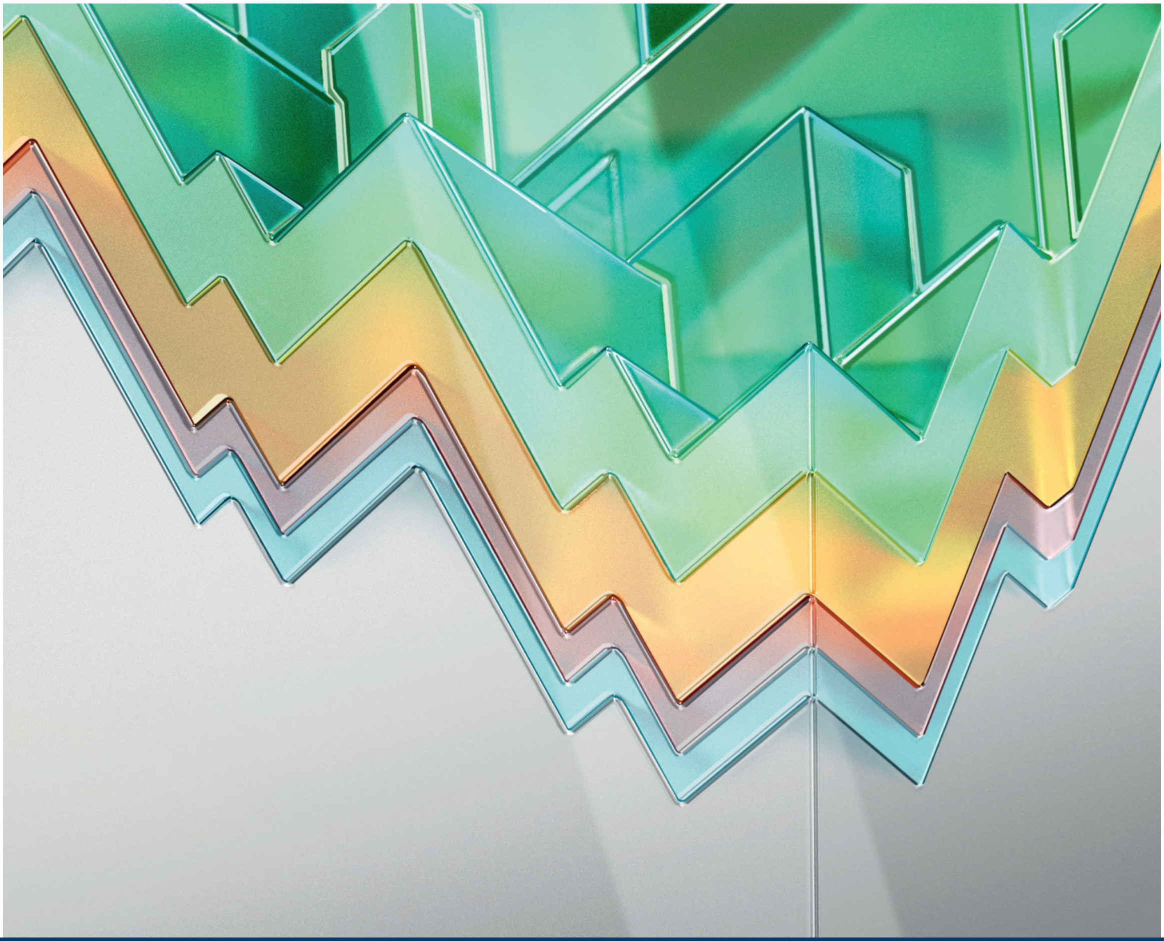

Transparent Passivating Contact for Crystalline Silicon Solar Cells

Malte Köhler

Energie & Umwelt / Energy & Environment
Band / Volume 538
ISBN 978-3-95806-550-5

Mitglied der Helmholtz-Gemeinschaft

JÜLICH
Forschungszentrum

Schriften des Forschungszentrums Jülich
Reihe Energie & Umwelt / Energy & Environment Band / Volume 538

Forschungszentrum Jülich GmbH
Institut für Energie- und Klimaforschung
IEK-5 Photovoltaik

Transparent Passivating Contact for Crystalline Silicon Solar Cells

Malte Köhler

Schriften des Forschungszentrums Jülich
Reihe Energie & Umwelt / Energy & Environment Band / Volume 538

ISSN 1866-1793 ISBN 978-3-95806-550-5

Bibliografische Information der Deutschen Nationalbibliothek.
Die Deutsche Nationalbibliothek verzeichnet diese Publikation in der
Deutschen Nationalbibliografie; detaillierte Bibliografische Daten
sind im Internet über http://dnb.d-nb.de abrufbar.

Herausgeber und Vertrieb: Forschungszentrum Jülich GmbH
Zentralbibliothek, Verlag
52425 Jülich
Tel.: +49 2461 61-5368
Fax: +49 2461 61-6103
zb-publikation@fz-juelich.de
www.fz-juelich.de/zb

Umschlaggestaltung: Grafische Medien, Forschungszentrum Jülich GmbH

Druck: Grafische Medien, Forschungszentrum Jülich GmbH

Schriften des Forschungszentrums Jülich
Reihe Energie & Umwelt / Energy & Environment, Band / Volume 538

D 82 (Diss. RWTH Aachen University, 2020)

ISSN 1866-1793
ISBN 978-3-95806-550-5

Für meine Großeltern Irmgard, Ruth, Hansheinrich und Georg

«The bare silicon surface is a very unhappy surface»

Prof. Dr. Thomas Kirchartz,
Kooperationsworkshop Hirschegg (2018)

Contents

Abstract

The goal of this work is to develop a transparent, passivating and conductive contact for the light facing side of crystalline silicon solar cells. State of the art passivating contacts show a very high passivation quality of the silicon surface as well as a high electrical conductivity. However, due to their restricted transparency and comparably high parasitic absorption for the incoming sunlight these contacts are not ideal for the use on the sun facing side of the solar cells. With the aim of increasing the efficiency of crystalline silicon solar cells, the need for a *transparent* passivating contact arises.

One material, which is suitable as a transparent passivating contact due to its high transparency and electrical conductivity, is n-type doped microcrystalline silicon carbide (µc-SiC:H(n)). It was shown in literature, that depositing µc-SiC:H(n) using hot-wire chemical vapor deposition (HWCVD) directly on the crystalline silicon surface leads to a deterioration of the passivation. Additionally it was shown, that using a thin silicon oxide (SiO_2) in between the crystalline silicon and the µc-SiC:H(n) can prevent this deterioration of the passivation while showing a high transparency and high electrical conductivity. However, transferring these properties of the contact layer stack into a first working solar cell proved to be difficult. Despite the high passivation quality and the high conductivity of the material, neither the desired voltage nor a high fill factor could be achieved on solar cell level. The focus of this thesis is therefore on the systematic implementation of this layer stack in a silicon heterojunction solar cell.

In the first part of this work, different wet-chemical oxidation processes for the formation of SiO_2 are evaluated in order to enable a high passivation quality. It is shown that different oxidation processes have an impact on the properties of the SiO_2 (thickness, stoichiometry, density). These properties then influence the passivation of the silicon surface after deposition of the µc-SiC:H(n). Furthermore, the results show that in addition to the oxidation process of the oxide, the wire temperature during the deposition of the µc-SiC:H(n) has a decisive influence on the passivation quality.

The second part of this work includes an analysis of the electrical and optical properties of µc-SiC:H(n) as a function of the wire temperature used during the HWCVD process. Additionally, the influence of the wire temperature on the passivation quality and on the contact resistivity of the SiO_2/µc-SiC:H(n) stack is investigated. It is shown that an increase in wire temperature increases the transparency and conductivity of the µc-SiC:H(n) and decreases the passivation quality of the contact. However, in order to achieve high power conversion efficiencies in the solar cell, the contact layers need to have high conductivity, which is reflected in low contact resistivity, and high passivation quality. To overcome this challenge, a double layer µc-SiC:H(n) was used. The layer in direct contact with the SiO_2 was deposited at low wire temperature to ensure high passivation quality. The second layer was deposited at high wire temperature to provide low contact resistivity and high transparency.

In the third part of this work, the insights from the first two parts are used for the preparation of solar cells. It is shown that using a µc-SiC:H(n) double layer stack instead of a single layer, mainly reduces the contact resistance and thus increases the fill factor of the solar cell (see Figure 0.1, green to yellow triangle). Furthermore, it is discussed that the deposition of the transparent conductive oxide (TCO), which is necessary for the lateral conductivity of the free charge carriers to the contact fingers of the solar cells, subsequently damages the passivation of the solar cell. Following an investigation of the mechanisms of sputter degradation, an optimization of the deposition conditions and the thermal post-treatment can significantly reduce the damage. This leads to an increase in the open circuit voltage of the solar cell (see figure 0.1, yellow to blue triangle). The additional use of a magnesium fluoride layer to reduce the reflection of the contact results in an increase of the short circuit current of the solar cell (see Figure 0.1, blue to red triangle). Due to this optimization of the contact, the highest efficiency (η) of this work is achieved with 24%. This means an increase in efficiency of $6.4\%_{\text{abs}}$ within this work.

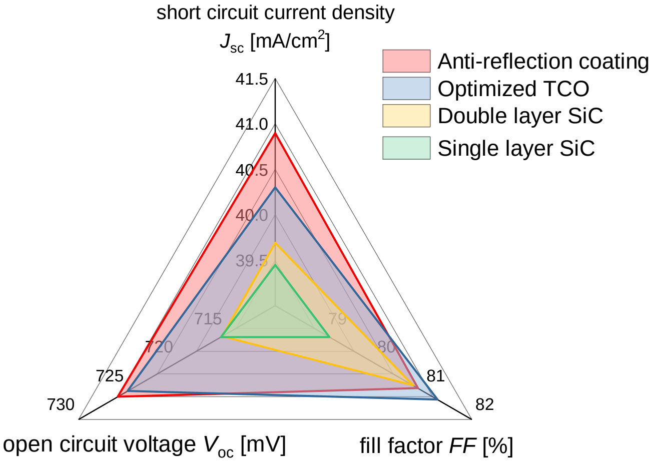

Figure 0.1.: *Evolution of the solar cell parameters J_{sc}, V_{oc} and FF using a single layer µc-SiC:H(n) (green, power conversion efficiency η = 22.3%), a double layer of µc-SiC:H(n) (yellow, η = 22.9%), an optimized TCO deposition (blue, η = 23.8%) and an anti-reflection coating (red, η = 24%).*

Zusammenfassung

Das Ziel dieser Arbeit ist es, einen transparenten, passivierenden und leitfähigen Kontakt für die dem Licht zugewandte Seite von kristallinen Siliziumsolarzellen zu entwickeln. Aktuelle passivierende Kontaktschichten zeigen eine sehr gute Passivierung der Siliziumoberfläche und eine hohe Leitfähigkeit. Aufgrund ihrer eingeschränkten Transparenz und relativ hohen parasitären Absorption des einfallenden Sonnenlichts sind diese Schichten jedoch nur bedingt für den Einsatz auf der Vorderseite von Solarzellen geeignet. Mit dem Ziel die Effizienz von kristallinen Siliziumsolarzellen zu steigern, entsteht die Notwendigkeit für einen *transparenten* passivierenden Kontakt.

Ein Material, das sich aufgrund seiner hohen Transparenz und Leitfähigkeit als ein transparenter passivierender Kontakt eignet, ist n-dotiertes mikrokristallines Siliziumkarbid (µc-SiC:H(n)). Wissenschaftliche Publikationen zeigen, dass eine direkte Beschichtung von kristallinem Silizium mit µc-SiC:H(n) mittels hot wire chemical vapor deposition (HWCVD) die Oberfläche des Siliziums schädigt und daher eine gute Passivierung verhindert. Des Weiteren konnte dargestellt werden, dass durch den Einsatz einer dünnen Siliziumoxidschicht (SiO_2) zwischen kristallinem Silizium und µc-SiC:H(n) eine gute Passivierung sowie eine hohe Leitfähigkeit und eine hohe Transparenz des Kontakts erzielt werden kann. Die Übertragung dieser Eigenschaften des Kontaktschichtstapels in eine erste funktionsfähige Solarzelle erwies sich jedoch als schwierig. Trotz hoher Passivierqualität und hoher Leitfähigkeit des Materials konnten mit der Solarzelle weder die gewünschte Spannung noch ein hoher Füllfaktor erzielt werden. Der Fokus dieser Arbeit liegt daher auf der systematischen Implementierung dieses Schichtstapels in eine Siliziumheterostruktursolarzelle.

Im ersten Teil dieser Arbeit werden verschiedene nass-chemische Ätzverfahren zur Bildung des SiO_2 evaluiert, um eine hohe Passivierqualität zu ermöglichen.

Es wird gezeigt, dass verschiedene Ätzverfahren aufgrund variierender Eigenschaften des SiO_2 (Dicke, Stöchiometrie, Dichte) die Passivierung der Siliziumoberfläche durch den Kontakt beeinflussen. Des Weiteren zeigen die Ergebnisse, dass zusätzlich zum Herstellungsverfahren des Oxids auch die Drahttemperatur während der Abscheidung des µc-SiC:H(n) einen entscheidenden Einfluss auf die Passivierqualität nimmt.

Der zweite Teil dieser Arbeit beinhaltet eine Analyse der elektrischen und optischen Eigenschaften des µc-SiC:H(n) in Abhängigkeit der verwendeten Drahttemperatur während des HWCVD Prozesses. Zusätzlich wird der Einfluss der Drahttemperatur auf die Passivierqualität und auf den Kontaktwiderstand des SiO_2/µc-SiC:H(n) Stapels untersucht. Hier zeigt sich, dass durch eine Erhöhung der Drahttemperatur die Transparenz und die Leitfähigkeit des µc-SiC:H(n) steigen und die Passivierqualität des Kontakts sinkt. Um eine hohe Effizienz der Solarzelle zu ermöglichen, benötigt es jedoch eine hohe Leitfähigkeit, die sich in einem geringen Kontaktwiderstand zeigt, sowie eine hohe Passivierqualität. Um diese Herausforderung zu überwinden, wurde eine Doppelschicht µc-SiC:H(n) verwendet. Die Schicht in direktem Kontakt mit dem SiO_2 wird bei geringer Drahttemperatur abgeschieden, um eine hohe Passivierung zu gewährleisten. Die zweite Schicht wird bei hoher Drahttemperatur abgeschieden, um einen geringen Kontaktwiderstand und eine hohe Transparenz zu ermöglichen.

Im dritten Teil dieser Arbeit werden die Erkenntnisse aus den ersten beiden Teilen für die Präparation von Solarzellen eingesetzt. Es wird gezeigt, dass durch den Einsatz der µc-SiC:H(n) Doppelschicht im Vergleich zur Einzelschicht hauptsächlich der Kontaktwiderstand des Schichtstapels verringert und somit der Füllfaktor der Solarzelle erhöht werden kann (siehe Abbildung 0.2, grünes und gelbes Dreieck). Außerdem wird diskutiert, dass die Deposition des transparenten, leitfähigen Oxids (TCO), das für die Querleitfähigkeit der freien Ladungsträger zu den Kontaktfingern notwendig ist, die Passivierung der Solarzelle nachträglich schädigt. Im Anschluss an eine Analyse des Schädigungsmechanismus kann eine Optimierung der Depositionsbedingungen sowie der thermischen Nachbehandlung den Schaden signifikant reduzieren. Dies führt zu einer Erhöhung der Leerlaufspannung der Solarzelle (siehe Abbildung 0.2, blaues Dreieck). Durch den zusätzlichen Einsatz einer Magnesium-

fluorid Schicht zur Reduktion der Reflexion des Kontakts wird eine Steigerung des Kurzschlussstroms der Solarzelle erreicht (siehe Abbildung 0.2, rotes Dreieck). Durch diese Optimierungen des Kontakts wird die höchste Effizienz (η) in dieser Arbeit mit 24% erzielt. Dies bedeutet eine Effizienzsteigerung um 6.4%$_{\text{abs}}$ im Vergleich zu vorherigen Resultaten.

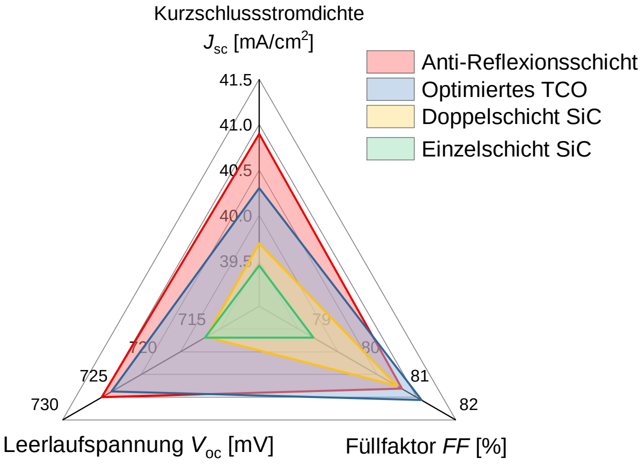

Abbildung 0.2.: *Entwicklung der Solarzellenparameter J_{sc}, V_{oc} und FF bei Einsatz einer Einzelschicht µc-SiC:H(n) (η = 22.3%), einer Doppelschicht µc-SiC:H(n) (η = 22.9%), einer optimierten TCO Deposition (η = 23.8%) und einer Anti-Reflexionsbeschichtung (η = 24%).*

1. Introduction

The world's population is expected to grow and so is the world's energy consumption [1,2]. Since the world's production of electricity today is still mainly based on fossil fuels (largest share in 2018 was coal with 38%) the carbon dioxide emissions are increasing with increasing electricity production [2]. However, to achieve the goals of the Paris climate agreement from 2016 [3] all industrial sectors need to be decarbonized to limit the climate change. One way to transform the energy sector is to increase the share of renewable energy. The share of renewable power generation increased from 2017 to 2018 from 8.4% to 9.3% [2]. In 2018 the global consumption of electrical energy increased by 3.7% [2]. This increase was mainly compensated by 33% of renewable energy sources, 31% by coal, and 25% by natural gas [2]. Due to a rise in the consumption of fossil fuels this led to an estimated increase of carbon emissions by 2.7%, which is the highest growth rate in the past seven years [2]. However, to achieve the goals of the Paris agreement the energy-related carbon emissions need to be reduced yearly by 3.5% until 2050 [4]. Despite the strong growth of renewable energies in recent years the energy mix between 36% non-fossil fuels and 38% coal has not changed much within the past 20 years. To achieve a reduction in carbon emissions within the energy sector the share of renewable energies has to be increased significantly stronger than the growth of the energy consumption. In 2018 the global share of renewable energy production in the electricity sector was 9.3% and increased by 10.5% compared to 2017 [2].

One driving force of the increase in renewable energy production was the photovoltaic electricity production, which showed a growth rate of 28.9% in 2018 [2]. One reason for this increase in photovoltaic electricity production is its competitive price compared to the average cost of electricity in several countries [5]. This development shows that photovoltaic energy production is transforming from a subsidized technology to a competitive pricing model, which is able to compete against conventional energy production [6]. To reach this so called «grid parity» in even more countries the cost for a kWh of photovoltaic energy has to be further reduced. Since the price of the solar module is only a small fraction of the overall costs for a photovoltaic installation, reducing the module costs does not influence the price significantly. One better way is to increase the energy output per solar module by increasing the efficiency of the solar cells. Therefore, the main focus in the crystalline silicon community is to increase the efficiency of the solar cells and solar modules. With a share of 95% in production capacity in 2017 crystalline silicon solar cells are dominating the photovoltaic market today [6].

The efficiency of crystalline silicon solar cells can be improved by reducing losses of the solar cell. Swanson and Sinton [7] as well as Glunz and Feldmann [8] describe the process of improving the solar cell efficiency as fixing holes in a leaky bucket, which should hold as much water as possible. In recent years several holes in this leaking bucket were already fixed e.g. by reducing the recombination of photo-generated charge carriers. Recombination describes the process of excited charge carriers which fall back into their ground state. When charge carriers recombine they cannot be used in the external circuit, thus, the efficiency of the solar cell decreases. The recombination of charge carriers mainly happens at the crystalline silicon (c-Si) interface. The reduction of recombination was predominantly achieved in recent years by adding layers on top of the crystalline silicon to reduce the number of open silicon bonds at the surface. These contact layers need to be conductive to enable a transport of the generated charge carriers to the external circuit of the solar cell. Otherwise resistive losses lead to a decreased efficiency. However, by fixing the leaking hole of surface recombination and resistive losses another hole in the bucket was increased. By adding these passivating layers on top of the crystalline silicon, less radiation of the sun reaches the crystalline silicon absorber, which increases the optical losses of the solar cell. Thus, the leaking bucket of the solar cell efficiency has three main holes, which need to be sealed as well as possible. The first hole represents the recombination losses, the second hole represents the resistive losses, and the third hole represents the optical losses of the solar cells. These three elements are the key to achieve a high efficiency of silicon solar cells and can be represented by the «magic triangle» depicted in Figure 1.1. By reducing the recombination of solar cells the

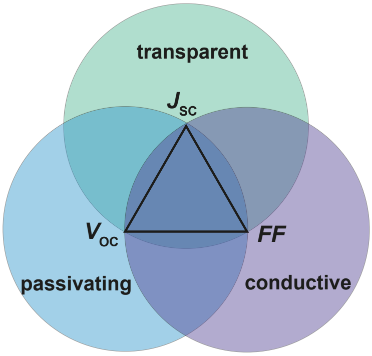

Figure 1.1.: *Optimizing a transparent passivating contact involves three parameters, which need to be tuned to maximize the power conversion efficiency of solar cells. These three parameters are the short circuit current density (J_{sc}), open circuit voltage (V_{oc}), and fill factor (FF). The contact structure must passivate the silicon surface very well, has a high electrical conductivity and a high optical transparency. This figure was originally published in [9] and was adapted (CC BY 4.0).*

maximum voltage (V_{oc}) of the solar cell is increased. By using high conductive layers the fill factor of the solar cells is increased (FF). By mitigating optical losses of the solar cell the maximum current (J_{sc}) is increased. Since conductive and passivating contacts are already available the main focus needs to be to reduce the optical losses.

The optical losses can be mitigated by using high transparent layers as passivating contact layers for the light facing side of solar cells. One material combination, which has a high optical transparency as well as a sufficient conductivity and a high passivation ability, is the combination of silicon dioxide (SiO_2) and n-type hydrogenated microcrystalline silicon carbide (µc-SiC:H(n)). In the following this contact scheme will be called «transparent passivating contact (TPC)». SiO_2 in combination with silicon is an intensively studied and well known material within the semiconductor and transistor community. It has a high passivation ability on the silicon surface and is very transparent for the incident light. However, SiO_2 is an insulator and cannot transport the electrical current. Therefore, it can only be used as a very thin layer so that the charge carriers have a high probability of quantum mechanically tunneling through the oxide. The µc-SiC:H(n) has a high optical transparency and a high conductivity but the passivation ability when applied directly on the crystalline silicon surface is very low. Thus, the stack of thin SiO_2 and µc-SiC:H(n) is a very promising candidate to fill all three holes in the leaky bucket whilst achieving a high efficiency of the solar cells. Intensive studies regarding the optical properties, electrical properties, and contact properties of µc-SiC:H(n) have been performed by Pomaska in his PhD thesis [10]. However, a systematic investigation of the integration of SiO_2/µc-SiC:H(n) as a transparent passivating contact for crystalline silicon solar cells is still lacking. This work aims to close this gap.

This thesis is divided into seven Chapters. While Chapter 1 is the introduction, in Chapter 2 the necessary fundamental information for this thesis are summarized. It is divided into four Sections. In Section 2.1 the physical basics of the solar cell operation are discussed. In Section 2.2 the qualitative and quantitative concepts of the selectivity of contacts are reviewed. In Section 2.3 state of the art passivating contact concepts are discussed with a focus on the concepts involving tunnel oxide layers. In Section 2.4 fundamental properties and preparation methods of SiO_2 are reviewed.

In Chapter 3 experimental details regarding the preparation and characterization of the layers and devices are given. In Section 3.1 the preparation of the SiO_2 and µc-SiC:H(n) as well as all additional processes to form the transparent passivating contact (TPC) are explained. In Section 3.2 the measurement methods to investigate the structural properties of µc-SiC:H(n) are listed. In Section 3.3 measurement methods to characterize the optical properties of µc-SiC:H(n) as well as the thickness of the thin SiO_2 layer are explained. In Section 3.4 the methods to characterize the contact properties of the SiO_2/µc-SiC:H(n) stack as well as to characterize the finished solar cell devices are described.

Chapter 4 discusses the results of experiments using different wet-chemical oxidation solutions to prepare thin SiO_2 tunnel layers, which have a high passivation quality and a high tunnel probability. In Section 4.1 the influence of the oxidation time and the SiO_2 thickness on the passivation quality and tunnel probability is investigated. A pre-selection of suitable oxidation solution is done. In Section 4.2 the pre-selected oxides are tested by changing the filament temperature during hot wire chemical vapor deposition (HWCVD) of µc-SiC:H(n), which significantly influences the passivation and conductivity properties of the TPC depending on the oxide preparation method. Finally, one oxidation procedure was selected, which was used to prepare the SiO_2 for the following experiments. In Section 4.3 the results of the Chapter are summarized.

In Chapter 5 material properties of µc-SiC:H(n) and contact properties of the SiO_2/µc-SiC:H(n) stack were investigated. In Section 5.1 the influence of the filament temperature during HWCVD on the electrical conductivity, the doping density, and the crystallite size of the µc-SiC:H(n) is studied. In Section 5.2 the influence of the filament temperature on the optical bandgap, the sub-bandgap absorption and the parasitic absorption of µc-SiC:H(n) is discussed. In Section 5.3 the passivation properties and electrical contact properties of the TPC are optimized. Possible passivation mechanisms of the TPC are discussed and a double layer stack of µc-SiC:H(n) is introduced to achieve a high passivation quality and a high electrical conductivity. The results of the Chapter are summarized in Section 5.4.

In Chapter 6 the TPC is used to fabricate the front side of silicon heterojunction solar cells. In Section 6.1 selected wet-chemical oxidation solutions are tested on device level to find the best performing oxide in solar cells. In Section 6.2 a single layer of µc-SiC:H(n) is used in the TPC to produce solar cells. A fill factor loss analysis is performed to find the limiting parameters . In Section 6.3 a double layer stack of µc-SiC:H(n) is used in the TPC to achieve a high passivation and a high electrical conductivity of the contact. The deposition parameters of both µc-SiC:H(n) layer are optimized using a design of experiment approach. In Section 6.4 the transparent conducting oxide (TCO) layer is optimized for the use with the TPC. The degradation mechanisms happening due to sputtering of the TCO are investigated and selected suitable materials for TCOs are screened. The deposition parameters are then optimized for the best performing TCO. Finally, the optical reflection of the front side is reduced by applying an anti reflection coating of magnesium fluoride in Section 6.5.

In Chapter 7 the main conclusions of this work are summarized and an outlook for the further optimization of the TPC is given.

2. Fundamentals

2.1. Basic semiconductor principles

From an electrical point of view materials can be divided into three groups: metals, semiconductors, and insulators [11]. The difference between these groups is the position of their so called energy bands. The energy bands consist of energy states. An energy state describes a energetic position which can be occupied by a charge carrier. Metals have one energy band which is partly filled with electrons and has partly unoccupied energy states (see Figure 2.1 i). Due to the unoccupied states electrons can move across the metal with a minimum surplus of energy, thus metals are good electrical conductors.

Semiconductors and insulators have two energy bands which are called the «valence band» and the «conduction band» (see Figure 2.1 ii and iii). While (at $T = 0$ K) in the valence band all energy states are filled with electrons the energy states in the conduction band are completely empty. The energetic distance between both bands is the so called bandgap energy (E_g). Within the bandgap there are ideally no energy states. Due to the completely filled valence band the electrons cannot move, thus, these materials cannot conduct an electrical current in this state. When the temperature of the semiconductor is above 0 K charge carriers can be exited thermally into the conduction band. Within the conduction band plenty of free energy states are available, thus, the electron can move and the material becomes conductive. Whenever an electron is excited from the valence into the conduction band a hole (positively charged) is created in the valence band which is the unoccupied state of the electron. The density of free charge carriers is denoted the intrinsic charge carrier concentration (n_i) and depends on the bandgap and the temperature of the semiconductor material. For silicon the intrinsic charge carrier

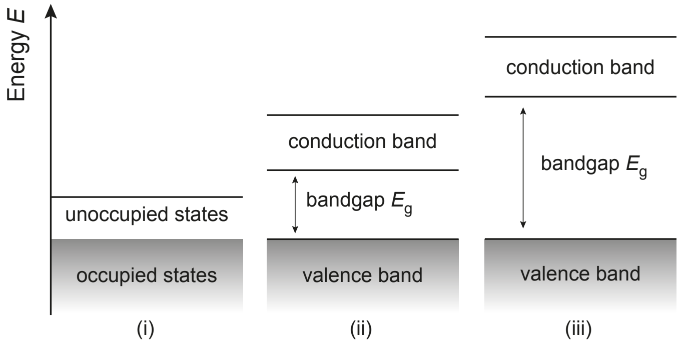

Figure 2.1.: *Energy band diagram of a conductor (i) with occupied and empty (unoccupied) energy states in the band, semiconductor (ii) and insulator (iii) with filled valence band and empty conduction band. The bandgap energy (E_g) is the distance between the highest occupied and the lowest unoccupied state.*

concentration at $T = 300$ K is $n_i = 9.65 \times 10^{-9}$ cm^{-3} [12]. The electrical conductivity (σ) for each type of charge carrier depends on the charge carrier density (n) and the charge carrier mobility (μ)

$$\sigma = \mathrm{q}\, n\, \mu \tag{2.1}$$

with the elementary charge (q). The difference between semiconductors and insulators is the width of the energy bandgap. While semiconductors have typically bandgaps between 0.18 eV (InSb) and 5.5 eV (diamond) [13] isolator have a bandgap of about 10 eV [11].

The occupation of the energy states in the valence band and conduction band by electrons is described by the Fermi distribution $f(E)$ as a function of the energy of the electrons

$$f(E) = \frac{1}{\exp\left(\frac{E - E_\mathrm{F}}{\mathrm{k_B} T}\right) + 1} \tag{2.2}$$

with Fermi level (E_F), the Boltzmann constant ($\mathrm{k_B}$), and the temperature (T). The Fermi level which is also also called the «Fermi energy» is the characteristic energy where half of the energy states are occupied and the other half is empty. Since for intrinsic semiconductors at $T = 0$ K the valence band is fully occupied and the conduction band is empty, E_F is by definition in the middle of the bandgap.

To obtain the electron concentration in the conduction band (n_e) the density of energy states and the Fermi distribution are integrated over the electron energy starting at the conduction band minimum (E_c). The electron density in the non-illuminated semiconductor only depends on the temperature, the effective density of states in the conduction band (N_c) and the distance of the Fermi-level to the valence band edge and can then be calculated using the Boltzmann approximation

$$n_\mathrm{e} = N_\mathrm{c} \exp\left(-\frac{E_\mathrm{c} - E_\mathrm{F}}{\mathrm{k_B}T}\right). \tag{2.3}$$

The density of the holes (n_h) in the valence band can be calculated accordingly

$$n_\mathrm{h} = N_\mathrm{v} \exp\left(-\frac{E_\mathrm{F} - E_\mathrm{v}}{\mathrm{k_B}T}\right) \tag{2.4}$$

with the valence band maximum (E_v) and the effective density of states in the valence band (N_v). The multiplication of n_e and n_h gives

$$n_\mathrm{e} n_\mathrm{h} = n_\mathrm{i}^2 = N_\mathrm{c} N_\mathrm{v} \exp\left(-\frac{E_\mathrm{g}}{\mathrm{k_B}T}\right). \tag{2.5}$$

Since every excited electron creates a hole in the valence band, $n_\mathrm{e} = n_\mathrm{h}$ in an intrinsic semiconductor, and $n_\mathrm{e} n_\mathrm{h}$ only depends on material properties (N_c, N_v and E_g) and on the temperature.

The electronic properties of a semiconductor can be manipulated by doping the material. To increase the electron density in the conduction band, donor atoms can be added which have energy states close to the conduction band edge (E_c). The electrons in the donor states can be easily activated thermally into the conduction band. The electrical conductivity for electrons is increased and the semiconductor has an n-type character. To increase the hole density in the valence band, acceptor atoms can be added which have energy states close to the valence band edge (E_v). Thereby, the electrical conductivity for holes is increased and the semiconductor has an p-type character. The donor doping concentration (N_D) and acceptor doping concentration (N_A) are usually in the range of 10^{15} cm^{-3} – 10^{19} cm^{-3} [14]. Thus, in an n-type semiconductor the electron concentration, under the assumption of low

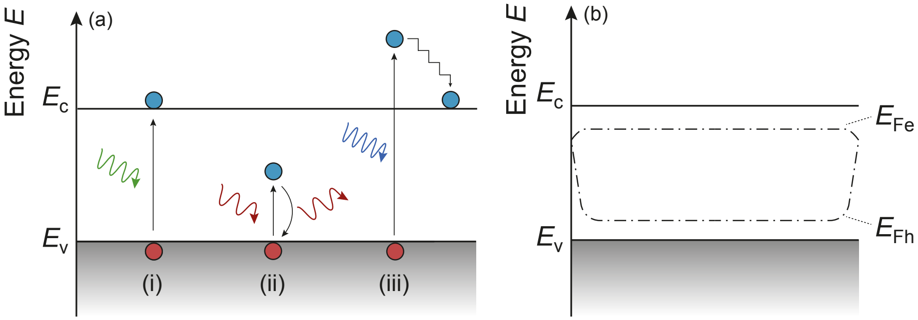

Figure 2.2.: *(a) Generation processes of charge carriers in semiconductors. (i) Absorption of a photon with a photon energy equal to the bandgap energy. (ii) Transmission of a photon since the exited electron does not reach the conduction band due to a photon energy lower than the bandgap. (iii) Absorption of a photon with a photon energy larger than the bandgap. The electron is excited deep into the conduction band and thermalizes back to the band edge. (b) Quasi-Fermi level splitting in an n-type semiconductor due generation of electron-hole pairs.* E_{Fe} *and* E_{Fh} *denote the quasi-Fermi levels of electrons and holes.*

injection, is dominated by the doping concentration with $n_\mathrm{e} \approx N_\mathrm{D}$, which leads to

$$n_\mathrm{h} = \frac{n_\mathrm{i}^2}{N_\mathrm{D}} \quad \text{and} \quad E_\mathrm{F} = E_\mathrm{c} - \mathrm{k_B} T \ln\left(\frac{N_\mathrm{c}}{N_\mathrm{D}}\right) \tag{2.6}$$

and for a p-type semiconductor with $n_\mathrm{h} \approx N_\mathrm{A}$ it leads to

$$n_\mathrm{e} = \frac{n_\mathrm{i}^2}{N_\mathrm{A}} \quad \text{and} \quad E_\mathrm{F} = E_\mathrm{v} + \mathrm{k_B} T \ln\left(\frac{N_\mathrm{v}}{N_\mathrm{A}}\right). \tag{2.7}$$

It can be seen that in a n-type semiconductor E_F is close to the conduction band and in a p-type semiconductor E_F is close to the valence band which is caused by the asymmetric charge distribution.

Solar cell operation A solar cell works by absorbing photons and creating electron-hole pairs. Whenever an electron is exited into the conduction band a positively charged hole is created in the valence band. The mechanism is visualized in Figure 2.2 a (i). This process is called the generation of electron-hole pairs. When the photon energy is smaller than the bandgap, the semiconductor is transparent (see Figure 2.2 a (ii)). Photons with higher energies than the bandgap excite electrons higher than the conduction band edge. These electrons then thermalize to the conduction band edge. The energy difference between photon energy (E_{Ph}) and the energy of the E_{c} is thereby transferred to the crystal lattice and creates phonon vibrations (see Figure 2.2 (iii)). These relaxation process happens on the time scale of 10^{-12} s.

By creating electron-hole pairs, the electron density in the conduction band increases simultaneously to the hole concentration in the valence band. The total charge carrier density is now the sum of the equilibrium electron concentration (n_{e}^{0}) in the dark and excess electron concentration (Δn_{e}) generated by the photons which is not equal to n_{i} anymore

$$n_{\mathrm{e}} = n_{\mathrm{e}}^{0} + \Delta n_{\mathrm{e}} \quad \text{and} \quad n_{\mathrm{h}} = n_{\mathrm{h}}^{0} + \Delta n_{\mathrm{h}}. \tag{2.8}$$

This leads to a problem in the mathematical description, since due to the increased electron concentration (n_{e}) in the conduction band the Fermi-level needs to be closer to the conduction band. Simultaneously, due to the higher hole concentration (n_{h}) in the valence band the Fermi-level also needs to be closer to the valence band. The problem is solved by splitting the Fermi-level into separate Fermi-levels for electrons and holes. These Fermi-levels are called quasi-Fermi level (QFL) and are denoted as energy of the quasi Fermi level of electrons (E_{Fe}) and energy of the quasi Fermi level of holes (E_{Fh}). The splitting of the QFLs in an n-type semiconductor can be seen in Figure 2.2 (b). The upper and lower dashed-dotted line represents the QFL of electrons and holes, respectively. To calculate the distance between the QFLs, the energies of the charge carriers are important.

The energy of the charge carriers can be divided into different forms. Due to their charge, the charge carriers have an electrical potential which is -qφ for electrons and qφ for holes. Due to their concentration the charge carriers also have a chemical potential which is written as ξ_{e} for electrons and ξ_{h} for holes. The combination of electrical and chemical potential is the electrochemical potential for electrons (η_{e}) and holes (η_{h}). The different potentials for electrons and holes are visualized in Figure 2.3. It can be seen that the difference of the quasi-Fermi levels

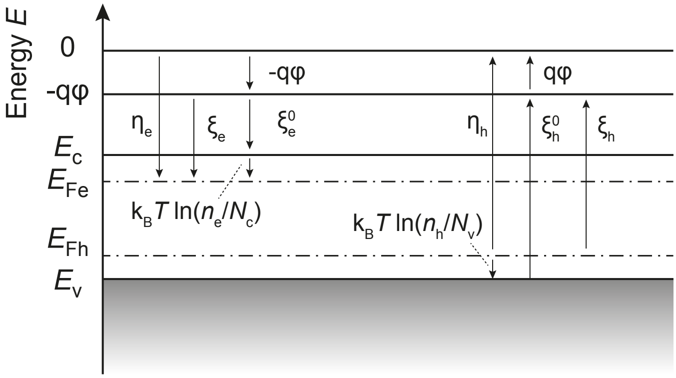

Figure 2.3.: *Energies of electrons and holes in a semiconductor. With the electrical potential ($-q\varphi$), the chemical potential of electrons and holes (ξ_e and ξ_h) and the electrochemical potential for electrons and holes (η_e and η_h). The position of the 0 energy is chosen arbitrarily. The diagram is adapted from [14].*

is the difference between the electrochemical potentials of electrons and holes. The splitting of the QFL can be calculated by

$$\eta_\mathrm{e} + \eta_\mathrm{h} = E_\mathrm{Fe} - E_\mathrm{Fh} = \mathrm{k_B}T \ \ln\left(\frac{n_\mathrm{e}\, n_\mathrm{h}}{n_\mathrm{i}^2}\right). \tag{2.9}$$

After generation of electron-hole pairs both charge carriers are at the same location and thus, in the same electrical potential. Therefore the electrical potential of the charge carriers cancels out and the electrochemical potential is equal to the chemical potential. This chemical potential now has to be converted in electrical energy which can be used in an external circuit. The conversion into electrical energy needs to take place before the electron-hole pairs recombine with each other. The lifetime of an electron-hole pair in silicon is typically in the 10^{-3} s range. The lifetime of the charge carriers is determined by the recombination processes happening in the semiconductor. Details about recombination processes may be found later in this Chapter. During this typical lifetime of the charge carriers at the conduction band edge, the electron-hole pairs need to be separated and then separately extracted at the distinct contacts. To extract electrons and holes separately, the symmetry of the semiconductor needs to be broken. The most basic idea is to imagine a membrane at each side of the semiconductor which only enables either electrons or holes to pass. Thus, these membranes are «selective» for one type of charge carrier. Details about selective contacts can be found in the following Section.

2.2. Selectivity

For the solar cell to deliver electrical energy, the generated electron-hole pairs need to be separately extracted at the distinct contacts. Therefore, each contact should only be conductive for one type of charge carrier. The most basic idea is to imagine a membrane at each side of the semiconductor which only allows either electrons or holes to pass (see Figure 2.4 a). Thus, these membranes are «selective» for one type of charge carrier. The idea of the contact as a membrane can be found in Würfel [14]. These membranes for solar cell contacts have three basic design criteria.

1. The membrane needs to maximize the flow of majority charge carriers out of the semiconductor. Thus, the series resistance needs to be as low as possible.
2. The membrane should minimize recombination at the interface.
3. The membranes at each side of the cells should be asymmetric so that both carrier types are extracted separately.

The flow of the charge carriers out of the solar cell (criterion 1) is the external current (J_{ex}). To drive the charge carriers to the distinct contact they can be either driven by an electric field (see Figure 2.5 a) or by a concentration gradient which is the chemical potential (see Figure 2.5 b). The current driven by the electric field is a drift current (J_{drift}) and can be expressed for electrons as

$$J_{\text{drift}} = \sigma_{\text{e}} \nabla(-\varphi) \tag{2.10}$$

with the electrical conductivity of electrons (σ_{e}), and the gradient of the electrostatic potential $\nabla(\text{-}\varphi)$. The current driven by the concentration gradient is as diffusion current (J_{diff}) and can be expressed for electrons as

$$J_{\text{diff}} = \text{q} D_{\text{e}} \nabla(n_{\text{e}}) \tag{2.11}$$

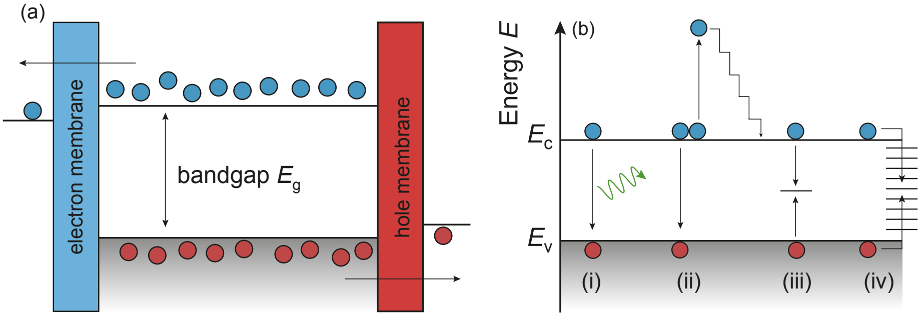

Figure 2.4.: *(a) Visualization of a selective contact realized by an electron membrane (blue) and a hole membrane (red) including the metal contacts at each side. The membranes should be semipermeable for one type of charge carriers. (b) Recombination processes of excited charge carriers: (i) radiative recombination, (ii) Auger recombination, (iii) SRH recombination, and (iv) surface recombination .*

with the electron diffusion coefficient (D_e). However, this equation does not show the driving force of the diffusion current. The driving force of the electron diffusion current is the gradient of the chemical potential of electrons $\nabla(\xi_e)$. With the relation $\frac{\nabla(n_e)}{n_e} = \frac{\nabla(\xi_e)}{k_B T}$ Equation 2.11 results in

$$J_{diff} = \frac{q D_e n_e}{k_B T} \nabla(\xi_e). \tag{2.12}$$

Using the Einstein relation $\frac{D_e}{\mu_e} = \frac{k_B T}{q}$ and Equation 2.1 this simplifies Equation 2.12 to

$$J_{diff} = \frac{\sigma_e}{q} \nabla(\xi_e). \tag{2.13}$$

The external electron current is a the sum of J_{drift} and J_{diff} and can be written as

$$J_{ex} = \frac{\sigma_e}{q} \nabla(-q\varphi + \xi_e). \tag{2.14}$$

Since $-q\varphi + \xi_e$ is equal to the the electrochemical potential electrochemical potential of electrons (η_e) and the quasi-Fermi level of electrons E_{Fe} (see Figure 2.3), Equation 2.14 can be simplified to

$$J_{ex} = \frac{\sigma_e}{q} \nabla \eta_e \quad = \frac{\sigma_e}{q} \nabla E_{Fe}. \tag{2.15}$$

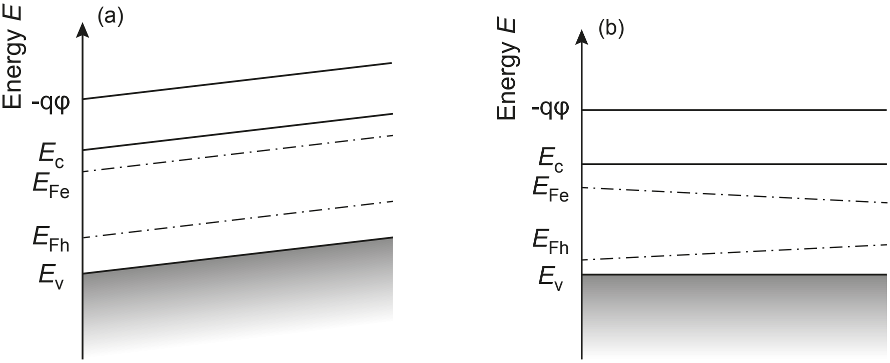

Figure 2.5.: *(a) Energy of the electrons due to an electric field without a gradient of the chemical energy. (b) Energy of the electrons without an electric field with a gradient of the chemical energy. Sketch is adapted from [14].*

Equation 2.15 is also valid for holes when using the electrical conductivity of holes (σ_h) and E_Fh. To maximize the external current (design criterion 1) the σ of the selective contact can be increased.

The electrical conductivity can be increased by choosing a contact material with a high mobility for one type of charge carrier. Additionally, the electrical conductivity depends on the carrier density which can be increased by doping of the contact as described before. However, if the contact is doped too high this can lead to the so called «Auger» recombination. Increased recombination contradicts the design criterion 2 that a selective contact should reduce recombination.

In a semiconductor different types of recombination occur with different probabilities depending e.g. on the used semiconductor material. One recombination path in semiconductors is **radiative recombination**. An electron and a hole recombine by emitting a photon (see Figure 2.4 b (i)). This process is the inverse process of photo-generation and can therefore not be omitted. The recombination rate of the radiative recombination (R_rad) is proportional to the electron (n_e) an hole (n_h) concentration $R_\mathrm{rad} \propto n_\mathrm{e} n_\mathrm{h}$. Due to the indirect bandgap of silicon radiative recombination has a low probability in this material.

The **Auger recombination** is a non-radiative recombination mechanism [15]. The energy of the recombining electron-hole pair is not emitted as a photon but transferred to another charge carrier which is exited within the conduction or valence band and thermalizes back to the band edge (see Figure 2.4 b (ii)). Thus, this process requires a third charge carrier. In an n-type semiconductor the Auger recombination rate is $R_{\mathrm{Aug,n}} \propto n_{\mathrm{e}}^2\, n_{\mathrm{h}}$. Auger recombination therefore, is increased with increased doping of the semiconductor or at high light injection intensities.

A third recombination mechanism is the recombination via defects states so called «traps» within the bandgap. This recombination mechanism has been described by Shockley, Read and Hall and is also referred to as **SRH recombination** [16, 17]. The recombination happens when an electron falls into a trap state in the bandgap which is occupied by a hole or vice versa (see Figure 2.4 b (iii)). The excess energy is transferred with a high probability to the phonon system of the crystal. However, SRH statistics does not distinguish between the ways the energy is dissipated. Further details can be found in [18]. The electron recombination rate of the SRH depends on the the velocity of the electrons (v_{e}), the capture cross section for electrons of a trap state ($\sigma_{\mathrm{trap,e}}$) as well as on the density of trap states filled with a hole ($n_{\mathrm{trap,h}}$) and the electron concentration with $R_{\mathrm{SRH,n}} = v_{\mathrm{e}}\, \sigma_{\mathrm{trap,e}}\, n_{\mathrm{trap,h}}\, n_{\mathrm{e}}$. Traps which are located in the middle of the bandgap are more recombination active than traps close to the band edges. The reason for that is, that the probability of trapping a charge carrier is a function of the distance between trap and band. Traps in the middle of the bandgap have a similar probability of trapping a hole or an electron. For traps e.g. close to the conduction band it is way more likely that a trapped electron is re-emitted thermally into the conduction band than the trapping of a hole from the valence band. To reduce the SRH recombination is is necessary to reduce the trap state in the bandgap e.g. by using silicon with very few impurities and crystal defects.

A special case of the SRH recombination is **surface recombination**. Since the atoms at the crystal surface do not have a binding partner, the number of surface states can be very high e.g. for silicon <111> 8×10^{14} cm^{-2}. These surface states create a continuous distribution of traps at the interface (see Figure 2.4 b (iv)). The surface recombination rate (R_{surf}) is similar the Shockley-Read-Hall recombination rate (R_{SRH}). However, since this recombination happens at the surface, $n_{\mathrm{trap,h}}$ has the unit of occupied states per area and not per volume like for the SRH recombination. Therefore, $v_{\mathrm{e}}\,\sigma_{\mathrm{trap,e}}\,n_{\mathrm{trap,h}}$ has the unit of a velocity and is also known as the surface recombination velocity of electrons (S_{e}). Thus, $R_{\mathrm{surf}} = S_{\mathrm{e}}\,n_{\mathrm{e}}$.

The second design criterion for designing a selective membrane is to minimize recombination. To investigate the influence of the recombination on the solar cell energy output a formulation of the singe diode equation is used [19]

$$\mathrm{q}V_{\mathrm{oc}} = \mathrm{k_B}T\ln\left(\frac{J_{\mathrm{sc}}}{J_0}+1\right) \tag{2.16}$$

with the voltage at open circuit (V_{oc}), and the current of the solar cell at short circuit (J_{sc}). The saturation current density (J_0) is a representation of the recombination current in a solar cell. Since the surface recombination is the most dominant recombination mechanism in modern crystalline silicon solar cells, all other recombination shall be neglected in this example. Thus, the recombination in a p-type semiconductor ($n_{\mathrm{e}} \ll n_{\mathrm{h}}$) can be expressed by assuming low injection as the saturation current density

$$J_0 = \mathrm{q}S_{\mathrm{e}}n_{\mathrm{e}}^0. \tag{2.17}$$

Since the electrons are the minority carriers in a p-type semiconductor, n_{e}^0 can be expressed as

$$n_{\mathrm{e}}^0 = \frac{n_{\mathrm{i}}^2}{N_{\mathrm{A}}} \qquad \text{for } n_{\mathrm{e}}^0 \ll n_{\mathrm{h}}^0. \tag{2.18}$$

The intrinsic carrier concentration can be written as described in Equation 2.5. When combining Equation 2.18 and 2.5 and inserting it into Equation 2.17 this results in

$$J_0 = \mathrm{q}S_{\mathrm{e}}\,\frac{N_{\mathrm{c}}N_{\mathrm{v}}\exp\left(-E_{\mathrm{g}}/\mathrm{k_B}T\right)}{N_{\mathrm{A}}}. \tag{2.19}$$

For a p-type wafer dominated by surface recombination the recombination current depends on the surface recombination velocity (S_{e}), the bandgap of the absorber material (E_{g}), the doping concentration (N_{A}), and the temperature of the device (T). When inserting Equation 2.19 into Equation 2.16 this results in

$$\mathrm{q}V_{\mathrm{oc}} = E_{\mathrm{g}} - \mathrm{k_B}T\ln\left(\frac{\mathrm{q}S_{\mathrm{e}}\,N_{\mathrm{c}}N_{\mathrm{v}}}{J_{\mathrm{sc}}\,N_{\mathrm{A}}}+1\right). \tag{2.20}$$

The energy which can be extracted from the solar cell is represented by $\mathrm{q}V_{\mathrm{oc}}$. In a thermodynamic notation $\mathrm{q}V_{\mathrm{oc}}$ is the free energy. The free energy is the part of the

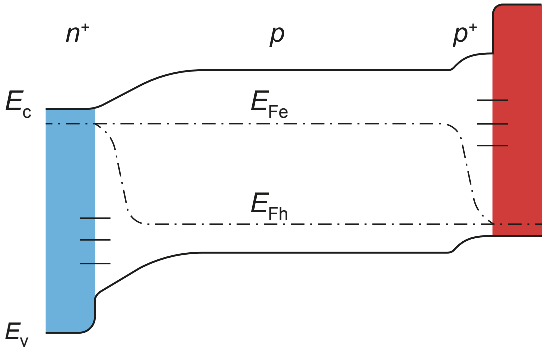

Figure 2.6.: *Band diagram with optimized n-type (blue) and p-type (red) selective contacts. The contacts are optimized by an increased bandgap of the contact, an increased doping in the* n^+ *and* p^+ *region and decreased surface states.*

enthalpy which can be drawn from the solar cell. The enthalpy is represented by E_g and is reduced by the entropy in the logarithmic term. Equation 2.20 shows how a selective membrane on a semiconductor which is dominated by surface recombination can be improved. The free energy can be increased by increasing the enthalpy and reducing the entropy of the system. To increase the enthalpy, the bandgap of the absorber material needs to be increased. To reduce the entropy of the system the surface recombination velocity of the electrons S_e should be decreased and the acceptor doping N_A should be increased. Additionally, the bandgap of the contact materials can be increased. In combination with a high electron affinity for n-type contacts and a low electron affinity for p-type contacts a high bandgap results in a barrier for minority carriers, which increases the selectivity. An optimized selective contact uses all these three methods to improve the free energy of the solar cell. Such a contact design is sketched in Figure 2.6. The p-type contact material (red) has a higher bandgap as the c-Si, it is highly doped so that the E_{Fh} is close the the valence band edge and the surface is passivated to reduce the number of trap states which reduces the surface recombination velocity. The same mechanisms works for the n-type doped contact (blue) just by increasing N_D which shifts E_{Fe} towards E_c.

The classical way to achieve selectivity in crystalline solar cells was to use buried junctions. Therefore, e.g. a moderately p-type doped silicon wafer was highly n-type doped at the front side to form the pn junction. Additionally, the wafer was highly p-type doped on the rear side to from a back surface field [20]. The doping of the front and rear side needs to be designed in a way that the series resistance of the device is as low as possible (high doping) and Auger recombination is avoided (moderate doping). By using homojunctions the bandgap of the contact cannot be increased which limits the selective contact. An additional problem of the homojunction design is the direct contact between the silicon and the metal electrode. This interface has a very high surface recombination velocity, since the metal introduces a continuum of trap states throughout the bandgap [14]. Thus, only one of the three design criteria can be fulfilled. To overcome the limitations of surface recombination, solar cells have been designed which use so called «passivating contacts». Selected designs of passivating contacts are discussed in Section 2.3.

The concept of selectivity was generally used as a qualitative description with no clear quantitative definition [21, 22]. However, in recent years various groups proposed quantitative definitions of the selectivity. Such quantitative definitions are helpful to compare different kinds of selective contacts with each other. Würfel et al. describe the selectivity as a difference in conductivity between electrons and holes [23]. Mora-Seró and Bisquert describe the reduction of selectivity by a leakage current at the contacts [24]. Tress et al. describes selectivity in organic solar cells by the surface recombination velocities [25]. Thus, no generally accepted concept of the quantitative definition of selectivity exists so far. However, the situation of ideal selectivity is widely accepted to be the state where the partial current of one charge carrier type becomes zero.

Roe et al. described the selectivity by the concentration difference of electrons and holes at the specific selective contact which are driving the respective minority ($J_{0,\mathrm{m}}$) and majority saturation carrier currents densities ($J_{0,\mathrm{M}}$) [26]. The selectivity (S) is then defined as $S = J_{0,\mathrm{M}}/J_{0,\mathrm{m}}$ at the specific contact. Another definition is proposed by Brendel and Peibst which uses the minority carrier resistivity (ρ_{m}) and the majority carrier resistivity (ρ_{M}) to define the selectivity $S = \rho_{\mathrm{m}}/\rho_{\mathrm{M}}$ [27]. The definition of Roe et al. and the definition of Brendel and Preibst are compared and generalized to an extended model by Rau and Kirchartz [28]. In the following the definition of selectivity by Brendel and Peibst is explained, since it is used in this work to compare the developed TPC to other selective contacts.

To calculate the selectivity, Brendel and Peibst propose to divide the minority carrier resistivity ρ_m by the majority carrier resistivity ρ_M

$$S = \frac{\rho_\mathrm{m}}{\rho_\mathrm{M}}. \tag{2.21}$$

Thus, a contact is very selective when the minority charge carrier resistivity is high which reduces the recombination at the interface and the majority carrier resistivity is low which enables majority charge carriers to pass the membrane. The minority carrier resistivity can be calculated by the minority carrier current density (J_m)

$$J_\mathrm{m} = J_\mathrm{c}\left(\exp\left(\frac{V}{V_\mathrm{th}}\right) - 1\right) \tag{2.22}$$

with the recombination parameter J_c, the voltage V and the thermal voltage $V_\mathrm{th} = \mathrm{k_B}T/\mathrm{q}$. Since the minority carrier resistivity is voltage dependent $\rho_\mathrm{m} = V/J_\mathrm{m}$ Brendel and Peibst used the inverse slope at $V = 0$ V

$$\rho_\mathrm{m} = \left(\frac{\mathrm{d}J_\mathrm{m}}{\mathrm{d}V}\bigg|_{V=0}\right)^{-1} = \frac{V_\mathrm{th}}{J_\mathrm{c}}. \tag{2.23}$$

Therefore, the minority carrier resistivity only depends on the thermal voltage which is constant for constant temperature and on the recombination parameter. To calculate the majority carrier resistivity a linear current-voltage characteristic is assumed which then leads to

$$\rho_\mathrm{M} = \left(\frac{\mathrm{d}J_\mathrm{M}}{\mathrm{d}V}\bigg|_{V=0}\right)^{-1} = \rho_\mathrm{c} \tag{2.24}$$

which is the contact resistivity. The majority carrier resistivity therefore is identical with the contact resistivity. To avoid large numbers Brendel and Peibst propose to use the logarithm of the selectivity S_{10} which can be calculated by

$$S_{10} = \log\left(\frac{V_\mathrm{th}}{J_\mathrm{c}\rho_\mathrm{c}}\right). \tag{2.25}$$

This logarithmic selectivity value can be used to compare different types of contacts. While the recombination parameter can be extracted from photo-conductance measurements as the J_0 value the contact resistivity can be measured by the transfer length method (TLM) as described in Chapter 3.

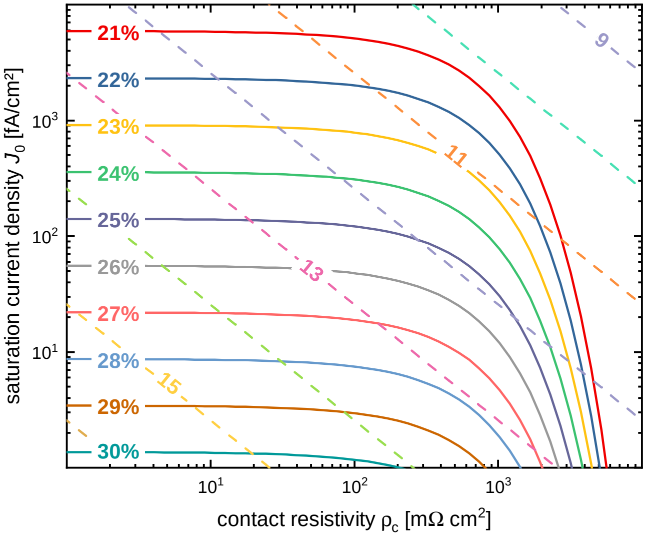

Figure 2.7.: *Visualization of iso-selectivities calculated from Equation 2.25 (dashed lines) and iso-efficiency lines calculated from Equation 2.26 with maximum power conversion efficiency $\eta_{max} = P_{max}/P_{sun}$ (solid lines) as a function of the parameters contact resistivity (ρ_c) and saturation current density (J_0). For the calculation of the efficiencies J_{sc} = 43.6 mA/cm^2 and V_{th} = 25.7 mV at a temperature of 25 °C were assumed.*

Nevertheless, a high selectivity of the contact does not necessarily lead to a high efficiency of the final solar cell. Therefore, the dependency of the power and thereby the efficiency of the solar cell on the saturation current density and the contact resistivity will be discussed in the following. As described by Rau and Kirchartz [28] the generated power P_{max} of the solar cell in the approach of Brendel and Peibst can be approximated by

$$\begin{aligned} P_{\mathrm{max}} &= J_{\mathrm{sc}} V_{\mathrm{oc}} FF_0 \left(1 - \frac{J_{\mathrm{sc}}\rho_{\mathrm{c}}}{V_{\mathrm{oc}}}\right) \\ &= J_{\mathrm{sc}} V_{\mathrm{th}} \ln\left(\frac{J_{\mathrm{sc}}}{J_0}\right) FF_0 - J_{\mathrm{sc}}^2\, FF_0\, \rho_{\mathrm{c}} \qquad (2.26) \end{aligned}$$

with the fill factor without the influence of the series resistance (FF_0). The FF_0 is defined by Green et al. [29] as

$$FF_0 = \frac{v_{\mathrm{oc}} - \ln(v_{\mathrm{oc}} + 0.72)}{v_{\mathrm{oc}} + 1} \tag{2.27}$$

with

$$v_{\mathrm{oc}} = \frac{V_{\mathrm{oc}}}{V_{\mathrm{th}}} = \ln\left(\frac{J_{\mathrm{sc}}}{J_0} + 1\right) \tag{2.28}$$

using Equation 2.16. For a comparison between selectivity and efficiency iso-selectivity (dashed lines) and iso-efficiency curves (solid lines) are plotted in Figure 2.7. For the calculation of the efficiency Lambertian light trapping was assumed leading to a $J_{\mathrm{sc}} = 43.6$ mA/cm^2 as well as a thermal voltage of $V_{\mathrm{th}} = 25.7$ mV at a temperature of 25 °C. The maximum efficiency was then calculated by dividing the maximum power of the solar cell by the power of the sun $\eta_{\mathrm{max}} = P_{\mathrm{max}}/P_{\mathrm{sun}}$.

In the Brendel and Peibst model the area of the selective contact can be divided into two parts. One part of the contact area is highly conductive but not passivating the other part of the contact is not conductive but highly passivating. Thus, changing the fraction of these two contact areas changes the contribution of resistive and recombination losses but does not change the selectivity. However, as it can be seen from the iso-efficiency lines in Figure 2.7, changing the fraction of the two contact areas may change the achievable efficiency. It can also be seen that resistive losses are strongly increasing for contact resistivities above a critical value. This critical value is characterized by the tangent points of the iso-selectivity lines with the iso-efficiency lines. When the contact resistivity is higher than this critical value the efficiency may be increased by increasing the conductive area fraction of the contact. If the contact resistivity lower than the critical value the losses due to imperfect passivation are dominating. Thus, increasing the passivated area fraction of the contact may increase the efficiency. It can be summarized that a quantitative selectivity is a powerful tool to compare different selective contact with each other. Nevertheless, a high selectivity of the contact does not necessarily lead to a high efficiency of the solar cell.

2.3. Passivating contacts

The passivating contacts were developed to suppress surface recombination of solar cells. Surface recombination is the dominant recombination mechanism in industrial standard silicon solar cells [30–33]. Since crystalline silicon has an indirect bandgap, radiative recombination is unlikely, because it is a three particle recombination. SRH recombination in the bulk can be omitted by using high quality silicon material with a low density of defects e.g. impurities and crystallographic defects. Auger recombination depends in non-concentrator solar cells mainly on the doping which can be designed in a way to reduce this recombination. Thus, the surface recombination is the most likely recombination mechanism in most modern solar cells. This recombination at the surface usually happens due to a high density of traps at the interface of the c-Si. These traps originate from unpaired electrons at the silicon surface. Improving the passivation quality of the silicon surface can be achieved in two ways: (i) by a reduction of the trap states or (ii) by a spatial separation of electrons and holes so that they cannot recombine with each other at the surfaces. This can be achieved by using selective contacts as discussed before. It should be noted that all passivating contacts are selective contacts but not all selective contacts are passivating contact.

To reduce the trap density at the interface the unpaired electrons of the silicon have to be paired by adding a layer on top of the c-Si. It was found that Si-based layers e.g. (SiO_2 [34,35], SiN_x [36], and hydrogenated amorphous silicon (a-Si:H) [37]) are well suited to passivate the c-Si surface. Remaining open silicon bonds can be additionally passivated by hydrogen atoms. Reducing the density of trap states at the interface is also called «chemical passivation»

A second method to reduce the surface recombination is to decrease the concentration of one recombination partner (either electrons or holes) at the surface. When only one type of charge carrier is present at the site of the trap recombination is suppressed due to the lack of a recombination partner. This can be achieved by implementing an electric field which repels one kind of charge carrier and attracts the other one. This type of passivation is also called «field-effect passivation». Further details about surface passivation can be found elsewhere [38, 39].

The industrial standard solar cell at the moment is build on the passivated emitter and rear cell (PERC) concept [40–42]. Even though most of the diffused emitter and the rear interface are passivated by dielectric films the metal electrodes are still in direct contact to the silicon to ensure a low contact resistivity. As discussed in the last section a metal/semiconductor interface has a high surface recombination which can reduce the efficiency of these solar cells due to a high surface recombination velocity which limits the V_{oc}.

The first solar cell concept which avoided a direct contact between metal electrode and c-Si was the silicon heterojunction (SHJ) solar cell [43]. In this concept the crystalline silicon is passivated with a thin intrinsic hydrogenated amorphous silicon (a-Si:H(i)) layer on both sides. This layer is providing a high chemical passivation due to the saturation of the open silicon bonds by the a-Si:H and the hydrogen which additionally passivates remaining open bonds. The a-Si:H(i) is followed by either a n-type doped hydrogenated amorphous silicon (a-Si:H(n)) or a p-type doped doped hydrogenated amorphous silicon (a-Si:H(p)) on each side of the wafer. In contrast to the PERC cell the pn-junction is not formed due to indiffusion of doping atoms into the wafer (homojunction) but by a doped external layer (heterojunction). Since the lateral conductivity of the a-Si:H layers is not sufficient an additional TCO is needed. Since the charge carriers now have to pass the a-Si:H layer stack when leaving the c-Si, the series resistance of the device can be critical which can influence the fill factor (FF) of the device. Thus, optimizing the efficiency is often a tread-off between FF and V_{oc} [44]. The current efficiency record for SHJ solar cells was reported online in 11/2019 by Hanergy as $\eta = 25.11\%$ with a $V_{\mathrm{oc}} = 747$ mV, $J_{\mathrm{sc}} = 39.6$ mA/cm^2 and a $FF = 85\%$ [45,46]. These results show very high V_{oc} and FF values. A detailed description of the obtained results in literature was not available at this time. A comparable efficiency was achieved by Kaneka Co. with $\eta = 25.1\%$ a significantly lower $V_{\mathrm{oc}} = 738$ mV, but a significantly higher $J_{\mathrm{sc}} = 40.8$ mA/cm^2 and a comparable $FF = 83.5\%$ [47].

Another material which is known to passivate the silicon surface very well is SiO_2. Due to its high bandgap SiO_2 is an isolator, thus to work as a contact materials the layer thickness needs to be extremely thin to enable quantum-mechanical tunneling of the charge carriers. An in-depth analysis of direct tunneling versus defect assisted tunneling at the c-Si/SiO_2 interface can be found in Li et al. [48]. Further details about silicon tunnel oxides can be found in the following Section 2.4. Excellent passivation was found by combining such a tunnel oxide which is providing the chemical passivation with a thin doped polycrystalline silicon (poly-Si) layer which provides the field effect passivation [49]. This contact has the advantage compared to a-Si:H passivated contacts that they are compatible with high temperature processing steps e.g. contact firing and can be implemented easier in existing solar cell production lines [50]. Nevertheless, in the classical approach only one passivating contact of SiO_2/poly-Si is implemented on the rear side while for the illuminated contact a diffused homojunction is used [51]. This leaves the front side with a direct metal contact to the c-Si which results in additional surface recombination resulting in a limited V_{oc}. The current record efficiency was achieved by Fraunhofer ISE and is up to now only reported in [52] without a detailed description of the device. The reported results are $\eta = 26\%$, $V_{\mathrm{oc}} = 732$ mV, $J_{\mathrm{sc}} = 42.1$ mA/cm^2 and a $FF = 82.3\%$. This cell compared to the SHJ record cells shows a significantly lower V_{oc} which is likely due to the passivated contact which is only on the rear side of the device. Nevertheless, the J_{sc} of the cell using the SiO_2/poly-Si contact is significantly higher than for the SHJ solar cell. The reason for this increase is the higher transparency of the front side of the SiO_2/poly-Si cells as compared to the a-Si:H on SHJ solar cell. The a-Si:H absorbs considerable parts of the incident sunlight which reduces the short circuit current density.

To further improve the efficiency of solar cells it is necessary to passivate also the front side of c-Si to achieve high V_{oc}. Contact materials need to be used which are highly transparent to enable a high J_{sc}. Additionally, the contact materials need to be conductive to transport the charge carriers to the electrode without imposing a high resistance to enable a high FF. Several materials have been investigated as passivating contacts for the front side of c-Si solar cells. Due to the high passivation quality of the SiO_2/poly-Si contact achieved on the back side of solar cells it was also used as a front contact of c-Si solar cells. Despite the high passivation quality the low bandgap of poly-Si $E_{\mathrm{g}} = 1.1$ eV [53] also shows a significant light absorption and need to be prepared very thin [54, 55]. Due to the thin layer thickness of poly-Si an additional TCO layer is necessary to support the lateral current transport. It was found that direct sputtering of TCOs results in a severe degradation of the passivation quality [56, 57]. Several methods have been shown to reduce the induced sputter damage. A degradation can be prevented by using an intermediate layer which is deposited by atomic layer deposition (ALD) [56] and by soft sputtering [58] or by annealing procedures [57, 58]. Double side passivated solar cells with SiO_2/poly-Si conacts have been shown by several groups [55, 59, 60]. The best solar cell efficiency so far has been reported by Larionova et al. with $\eta = 22.3\%$, $V_{\mathrm{oc}} = 721$ mV, $J_{\mathrm{sc}} = 38.6$ mA/cm^2, and a $FF = 80\%$ [59].

2.4. Silicon Tunnel Oxides

The tremendous success of silicon in the 20$^{\mathrm{th}}$ century of the last decade, which is also often called the silicon age, was not based on the superior material properties of the silicon itself. The decisive advantage compared to e.g. germanium was and still is the silicon oxide layer. The SiO_2 layer is chemically stable and allows the silicon wafer to be transported or shipped without degradation of the material properties. After arrival the oxide can be stripped off and a clean silicon surface is obtained. Furthermore, the c-Si/SiO_2 interface has a low density of interface states (D_{it}) and can therefore be used as e.g. a gate oxide or a buffer layer in chips or solar cells [61].

A thin native oxide layer already builds when pure silicon is left in air. The technological advantage of SiO_2 is that it can be produced artificially by thermal or wet-chemical oxidation or by deposition of SiO_2. Deposited SiO_2 is growing on top of the wafer and an additional source of silicon is needed. Oxidized SiO_2, however, uses the silicon atom of the wafer and includes oxide species by a chemical reaction. The oxide is therefore penetrating the first few nanometers of the wafer. By oxidation of silicon, very thin oxides of only a few atomic layer can be produced. Since the the oxide species have to penetrate into the silicon, the growing SiO_2 is posing a diffusion barrier which is practically limiting the oxide growth. Significantly thicker oxides cannot be obtained by longer oxidation times, since the thickness is growing logarithmically with oxidation time [62, 63]. The thickness of thermal oxidation can be calculated using the model developed by Massoud et al. [64].

For the fabrication of solar cells, SiO_2 is used in various ways. Before fabrication of any kind of crystalline silicon solar cells, the wafer is cleaned e.g. by a cleaning process developed at the Radio Corporation of America (RCA) [65] or ozone treatments [66, 67] which involves SiO_2. The standard process for diffused phosphorous emitters which is widely used for industrial solar cells is to grow a phosphorous-silicate glass on top of the wafer. From there the phosphorous indiffuses into the wafer and creates a shallow n-type doping in the silicon [68–70]. However, these oxides are removed typically in hydrofluoric acid (HF) after the process.

By using a rather thick SiO_2 passivation layer (6–10 nm) Blakers and Green were able to fabricate the first solar cell with an efficiency >20% in 1986 [71]. The use of SiO_2 lost some focus in the photovoltaic community due to the development of silicon nitride (SiN_x) deposited by plasma enhanced chemical vapor deposition (PECVD). Silicon nitride shows a excellent surface passivation quality for n-type silicon due to a high density of positive fixed charges and a high hydrogen content which passivates remaining silicon dangling bonds [36, 72, 73]. Furthermore, it is a very well suited anti-reflection coating enhancing the light incoupling into the solar cell. For p-type silicon surfaces aluminum oxide (Al_2O_3) deposited by ALD was found to have excellent surface passivation due to the high negative fixed charge density [74–76].

In recent years SiO_2 has regained interest in the solar cell community, due to the development of SiO_2/poly-Si contacts [8, 49, 77]. Since this SiO_2 layer is implemented in the solar cell stack the passivation and electronic properties are of increasing importance. The major requirements for the oxide in SiO_2/poly-Si contacts are a high chemical passivation of the silicon surface, a high conductivity through the SiO_2, and a high thermal stability. Therefore, the solar cell community is immensely profiting from the intensive studies of the metal-oxide semiconductor (MOS) community to improve the gate oxide for transistor applications. Buck and McKim found that the chemical preparation method of SiO_2 has a strong influence on passivation of the surface [78]. Angermann et al. then found that different wet-chemical and thermal oxidation methods result in different defect density at the c-Si interface (D_{it}) which might be the reason for a difference in passivation quality [79]. It was also found, that the c-Si/SiO_2 interface is not abrupt and perfectly stoichiometric [80]. Within the first few atomic layers all oxidation states of silicon (Si) can be found from stoichiometric (Si^{4+}) to sub-stoichiometric (Si^{3+} –

Si^{1+}) silicon oxide. Moldovan et al. found that the stoichiometry is dependent on the preparation method of the oxide and also linked to the passivation quality [81]. Oxides with higher stoichiometry show higher passivation qualities on samples passivated by SiO_2/poly-Si.

In this work the SiO_2 layer is used as a buffer layer between the c-Si and the µc-SiC:H(n). Therefore, the SiO_2 needs to passivate the c-Si surface to reduce surface recombination. Additionally, the oxide needs to conduct the charge carriers either by direct conduction (between c-Si and µc-SiC:H(n)) or quantum-mechanical tunneling and needs to be physically and chemically stable against the HWCVD of µc-SiC:H(n). In contrast to the SiO_2/poly-Si fabrication the SiO_2 in this work does not need to be stable against high temperatures, since only low temperature processes are involved. To produce a high quality requirements several wet-chemical oxidation solutions have been tested. The oxidation reaction of some of these solutions was investigated by Patzig-Klein [82] and shall be summarized in the following. This paragraph should only give a brief overview about possible oxidation reactions with different oxidation solutions. Details can be found Chapter 8 of the PhD thesis of Patzig-Klein [82].

A common solution to prepare SiO_2 on c-Si is concentrated HNO_3. Patzig-Klein investigated the oxidation reaction of a hydrogen terminated silicon wafer by oxidizing in 10% HNO_3 at 20 °C. It was shown that the oxide ions are inserted into the Si–Si back bonds and not directly into the Si–H bonds. In a first step the HNO_3 is reduced to NO_2 or N_2O_4 by generating a hole in the valence band (h_v^+). This

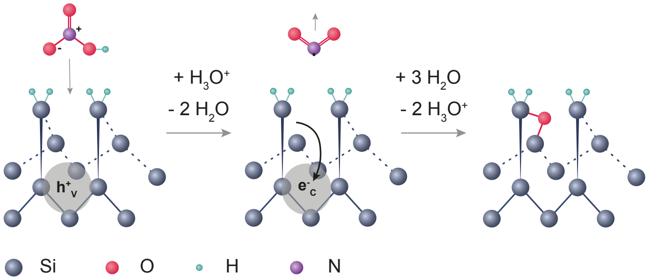

Figure 2.8.: *Oxidation reaction of hydrogen terminated c-Si by 10% HNO_3 at 20 °C. Figure adapted from [82].*

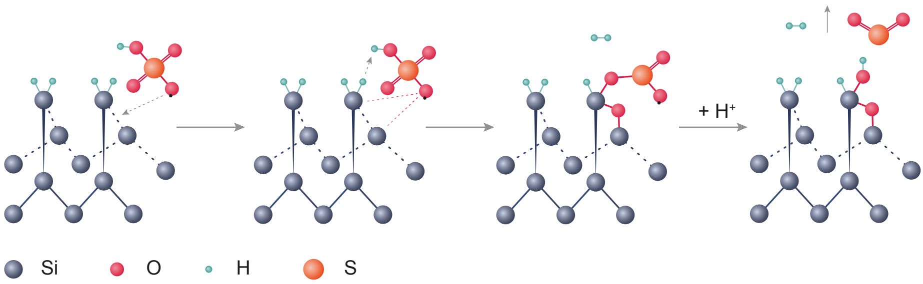

Figure 2.9.: *Oxidation reaction of hydrogen terminated c-Si by concentrated* H_2SO_4 *at 70 °C. Figure adapted from [82].*

process has already been proposed by Abel and Schmid in 1928 [83]

$$H_2Si \cdots SiH_2 + HNO_3 + H_3O^+ \rightarrow H_2Si \cdots SiH_2 + h_v^+ + NO_2 + 2H_2O. \tag{2.29}$$

The free hole in the valence band then enables the insertion of an oxide ion into the Si–Si back bond and creates an electron in the conduction band (e_c^-)

$$H_2Si \cdots SiH_2 + h_v^+ + 3H_2O \rightarrow H_2Si(O) \cdots SiH_2 + e_c^- + 2H_3O^+. \tag{2.30}$$

This process is visualized in Figure 2.8.

Patzig-Klein also investigated the SiO_2 formation by concentrated sulfuric acid (H_2SO_4). It was found, that for a reaction using H_2SO_4 additionally to the insertion of oxygen into the Si–Si back bonds a direct oxidation of the Si–H bond is possible. The reaction can be described as

$$H_2Si \cdots SiH_2 + H_2SO_4^- + H_3O^+ \rightarrow H_2Si \cdots (O)HSi\text{–}OH + SO_2 + H_2 + H_2O. \tag{2.31}$$

It was found, that the oxidation reaction of concentrated H_2SO_4 at 20 °C is rather slow and can be accelerated by heating it to 70 °C. The visualization of the oxidation process is illustrated in Figure 2.9. An additional oxidation solution is hydrogenperoxide (H_2O_2). One oxygen atom is inserted into the Si–Si back bond while water is produced.

$$\text{H–Si–Si–H} + H_2O_2 \rightarrow \text{H–Si–O–Si–H} + H_2O \tag{2.32}$$

$$\text{H–Si–O–Si–H} + 4H_2O_2 \rightarrow \text{H–Si(O)}_2\text{–O–Si(O)}_2\text{–H} + 4H_2O \tag{2.33}$$

$$H_2Si \cdots SiH_2 + H_2O_2 \rightarrow H_2Si(O) \cdots SiH_2 + H_2O \tag{2.34}$$

$$H_2Si(O) \cdots SiH_2 + 3H_2O_2 \rightarrow H_2Si(O)_2 \cdots Si(O)_2H_2 + 3H_2O \tag{2.35}$$

Due to the insertion of the oxygen the surface is getting less hydrophobic which then enables the water to adsorb and insert an oxygen into the Si–H bond.

$$H_2Si(O)_2 \cdots Si(O)_2H_2 + 2H_2O \rightarrow \text{HO–SiH(O)}_2 \cdots \text{(O)}_2\text{HSi–OH} + 2H_2 \tag{2.36}$$

This process is visualized in Figure 2.10.

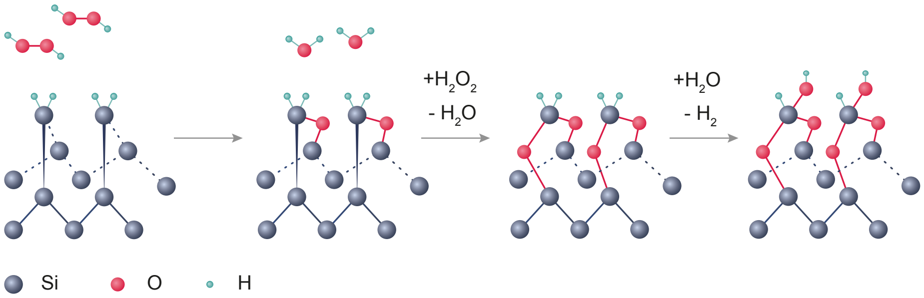

Figure 2.10.: *Oxidation reaction of hydrogen terminated c-Si by 10% H_2O_2 at 20 °C. Figure adapted from [82].*

In this work we use a mixture of concentrated sulfuric acid and hydrogen peroxide to oxidize the silicon surface which is known as «piranha solution», Caro's acid or Peroxymonosulfuric acid: $H_2SO_4 + H_2O_2 \rightarrow H_2SO_5 + H_2O$. Thus, the oxidation reaction might be different to that of H_2SO_4 and H_2O_2. Nevertheless, it is useful to understand the general differences in oxidation reactions.

3. Experimental Details

3.1. Preparation of the Transparent Passivating Contacts

Substrates and wafers In this work three different substrates are used. Samples designed for electrical conductivity, photothermal deflection spectroscopy (PDS) or transmission and reflection measurements are prepared on *corning EAGLE XG* glass. For film thickness, Fourier transform infrared spectroscopy (FTIR) and spectral ellipsometry (SE) measurements 15×15 mm^2 float zone (fz), double side polished (dsp) wafers pieces are used. For symmetric lifetime samples and solar cells 170 µm thick monocrystalline double side textured (dst) six inch Czochralski (Cz) wafers with a base resistivity of $1-5$ Ω cm are used. The wafers are quartered and labeled using a laser system resulting in 78×78 mm^2 wafers with one pseudo-square corner.

Silicon Tunnel Oxide In a first step the silicon wafers are cleaned using the standard procedure developed by the RCA [65]. The procedure consists of a 10 min dip in Standard Clean 1 (SC-1) at 60 °C, a first Quick Dump Rinse (QDR), a dip in Standard Clean 2 (SC-2) at 60 °C, a second QDR followed by a 5 min dip in 1% HF at room temperature (RT), and a last QDR. The receipts can be found in the following list. In a second step the tunnel oxide is prepared wet-chemically:

- **native** oxide in deionised water (DI-H_2O) at RT,
- 69.5% $\mathbf{HNO_3}$ at RT,
- **SC-1** DI-H_2O:H_2O_2(30%):NH_4OH(30%) 20:4:1 at 60 °C,
- **SC-2** DI-H_2O:H_2O_2(30%):HCl(37%) 20:1:1 at 60 °C,
- **piranha** H_2O_2(30%):H_2SO_4(96%) 2:1 at 60 °C,
- diluted $\mathbf{HCl:H_2O}$ in 1% or 8% at 80 °C.

After the oxidation both sides of the wafer have a symmetric SiO_2. Further details regarding the tunnel oxide formation can be found in Chapter 4.

Microcrystalline Silicon Carbide In a third step the µc-SiC:H(n) is prepared in an hot wire chemical vapor deposition (HWCVD) system also often referred to as a catalytic chemical vapor deposition (Cat-CVD). The system consists of a loadlock chamber and a deposition chamber. The transfer into the deposition chamber is done at a pressure below 2×10^{-6} mbar.

The samples are deposited in a top-down configuration. A heater is mounted above the substrate which has a temperature of 250 °C if not stated otherwise. Three rhenium wires with a diameter of 0.5 mm and a length of 15 cm are curled in seven curls to a length of approximately 10 cm. The wires are mounted on top of a frame consisting of gas inlet pipes to supply the precursors directly to the hot wire surface. The frame is mounted below the substrate where the distance between frame and substrate can be adjusted. The default distance is 97 mm. For the deposition of unintentionally doped µc-SiC:H(n) 5% monomethylsilane H_3Si-CH_3 (MMS) in H_2 and additionally H_2 are used as precursor gases. For intentionally doped µc-SiC:H(n) additional N_2 is used as a doping precursor. Each gas flow rate is controlled by mass flow controler (MFC) to manipulate the gas concentrations and the overall flow rate. The deposition pressure is kept at 0.75 mbar if not stated otherwise. The sample and the gases are pre-heated for 10 min before the start of the deposition.

The wires are heated by a current between 30 - 50 A resulting in filament temperature (T_f) of 1600 °C - 2100 °C. T_f is measured by a Raytek Marathon pyrometer. The precursors decompose catalytically at the surface of the hot wires and from radicals. After desorbing from the wires the radicals form the µc-SiC:H(n) on the substrate. The layer thickness is usually in the range of 20 – 50 nm.

Preparation of the rear side pn-junction As a fourth step the SiO_2 on the rear side is removed by a 5 min dip in 1% HF. The deposited µc-SiC:H(n) is stable against HF and protects the underlying SiO_2 on the front side. As a standard rear side for the SHJ solar cell a stack of a-Si:H(i) and a-Si:H(p) is deposited by PECVD. The PECVD machine is a commercial AK1000 system developed by Meyer Burger

Technology AG and is capable of depositing on 36 quartered six inch wafers or 9 six inch wafers per run. Therefore, it is possible to fabricate a complete batch of solar cells within one run which leads to less statistical scatter during solar cells development.

Transparent Conducting Oxide The TCO is deposited on top of the µc-SiC:H(n). In the standard configuration for solar cells indium tin oxide (ITO) is sputtered trough a mask to define four 2×2 cm^2 solar cells on each wafer. The standard ITO is deposited with a thickness of 70 nm to enhance the anti-reflexion effect of the TCO.

Metallization For the metallization of samples either a silver evaporation system or a screen printer is used. The silver evaporation system was in-house build while the screen printer is a MT-650TVC by Micro-tec Co. The evaporated silver results in 2 µm high silver fingers and busbars on the front side and a full area silver rear side with a thickness of 700 nm. The screen printed fingers have a height of 30 µm and a width of 55 µm. For a 2×2 cm^2 solar cells a busbar-less ten finger design with a squared silver frame around the active area is used. After the screen printing the cells are annealed for 40 min at 190 °C.

Anti-reflection coating The anti-reflection coating (ARC) is only used for TCO free solar cells and to reduce the reflection of the best solar cell with TCO. Therefore, magnesium fluoride (MgF_2) is thermally evaporated by an electron beam with a targeted layer thickness of 125 nm. The deposition is performed in a Leybold evaporation system.

3.2. Characterization of structural properties of µc-SiC:H(*n*)

Conductive atomic force microscopy To investigate the homogeneity of SiO_2 layers with respect to possible pinholes in the layer conductive atomic force microscopy (c-AFM) measurements are performed. After preparation the samples are immediately transferred into the vacuum to prevent further oxidation in air. Following, the measurements are performed inside the vacuum. The c-AFM system was build by omicron MATRIX and operated at the Peter Grünberg institute. For the measurements the c-AFM tip has a bias of several volts and the substrate is grounded. By scanning the surface the topography as well as the current signal at each point is obtained.

Profilometer The film thickness of the deposited µc-SiC:H(n) is measured using a Vecco DEKTAK 6M Stylus Profiler. Therefore, the layers are deposited in parallel on glass and on double side polished silicon pieces. Ink dots are placed in the middle of the samples using a permanent label writer. The ink is removed with isopropanol after the deposition leaving a hole in the layer where the height difference between substrate and layer is measured.

Fourier-transformed infrared spectroscopy (FTIR) The FTIR measurement is useful to determine the chemical composition of the µc-SiC:H(n) layers. Therefore, the sample is illuminated by infrared light. This light is exciting electric dipoles in the sample which absorbs the particular wavelength of the infrared light. The transmitted light through the sample is then detected by a spectrometer and then fourier-transformed. After correcting for the substrate signal which is measured separately on a bare silicon wafer only the absorption of the µc-SiC:H(n) remains. The result can then be plotted as FTIR-intensity as a function of the wavenumber (ν), which is the inverse of the wavelength (λ). From the FTIR-intensity the optical absorption coefficient (α) can be calculated by correcting the FTIR-intensity for the film thickness using the method of Langford et al. [84]. For FTIR measurements the Nicolet 5700 FTIR is used.

Time-of-flight secondary ion mass spectroscopy (ToF-SIMS) ToF-SIMS is a valuable technique to measure atom concentration in films. ToF-SIMS measurements are destructive, since a primary ion beam of Cs^+ is used to sputter secondary ions from the target material. The secondary ions are then accelerated in an electric field. Due to the sputtering it is possible to perform depth measurement or 3D mappings of atom concentrations in thin films. Quantification of the atom concentration is possible if a standard sample of the investigated material with a known atom concentration can be measured. For the measurement of nitrogen in µc-SiC:H(n) an unintentionally doped thick µc-SiC:H(n) layer with a known dose of ion implanted nitrogen is used for quantification. The time-of-flight secondary ion mass spectroscopy (ToF-SIMS) is used to measure nitrogen and hydrogen concentrations in µc-SiC:H(n) films. The measurements are performed at the central institute for engineering and analysis 3 of the research center Jülich with an ToF-SIMS IV by IONTOF.

X-ray defraction (XRD) The X-ray diffraction measurements are used to determine the crystallite sizes of the µc-SiC:H(n). Since the usually used µc-SiC:H(n) layers have been too thin and the X-ray diffraction (XRD) signal too weak, thicker µc-SiC:H(n) layers are prepared. The measurements are performed on a STOE Θ/Θ-Diffractometer in Bragg-Brentano mode at Röntgenlabor Dr. Ermrich. The average grain size is calculated from the SiC(006) peak.

3.3. Characterization of optical properties of µc-SiC:H(n)

Transmission and reflection measurements (T & R) To be able to obtain the refractive index and absorption coefficient the measurement data of T & R, PDS, and ellipsometry are combined. The transmission and reflection (T & R) measurements on µc-SiC:H(n) are performed on a Perkin Elmer Lambda 950 UV-VIS spectrometer.

Photothermal deflection spectroscopy (PDS) PDS measurements on an in-house built system are performed to investigate the absorption coefficient of µc-SiC:H(n). This method is particularly useful for thin samples, since it is very sensitive. The sample is mounted in a cuvette which is filled with carbon tetrachloride (CCl_4). Then the sample is illuminated by monochromatic light. Depending on the absorption the sample temperature changes. The generated heat in the sample is transferred to the CCl_4 which thereby changes its refractive index. This change in refractive index is measured by a laser which is orientated in parallel to the sample and slightly above the sample surface. The deflection of the laser beam due to the change in refractive index is measured by a four-quadrant diode. Details about the measurement technique are described in [85].

Ellipsometry Ellipsometry measurements are performed to determine the thickness of the SiO_2 after wet-chemical preparation on double side polished wafers. The measurements are performed in the clean room directly after preparation to prevent any further oxide growth in air. For these measurements a SENTECH 800 SE is used. For fitting the data an SiO_2 a model has been build within the software SpectraRay/3. An in-house build ellipsometer is used to determine the optical properties of µc-SiC:H(n) layers. To analyze the data a model was build using the Software SCOUT developed by W. Theiss Hard- and Software.

Electrochemical capacitance-voltage profiling (eCV) This technique is used to measure the active doping concentration (N^{act}) in semiconductors. Measuring the active doping concentration is interesting, since it can be related to the total doping atom concentration measured e.g. by ToF-SIMS to reveal the doping efficiency. To measure N^{act} a Schottky contact is necessary which is formed between the semiconductor material and an electrolyte (0.5M KOH). This Schottky contact forms a depletion region which acts a capacitor. By measuring the capacitance (C) as a function of the voltage (V) N^{act} can be calculated by

$$N^{\text{act}} = \frac{1}{\mathrm{q}\epsilon_0\epsilon_{\mathrm{r}}A^2} \times \frac{C^3}{dC/dV} \tag{3.1}$$

with the vacuum permittivity (ϵ_0) and the relative permittivity (ϵ_{r}) and the area of the contact A. To achieve a depth resolution of N^{act} the layer is etched in between the measurements. Further information about electrochemical capacitance-voltage profiling (eCV) measurements can be found in [86]. For the characterization of µc-SiC:H(n) voltage etching is used.

3.4. Characterization of the TPC contact and solar cells

Photo-conductance (PC) To analyze the passivation quality of the contact layers before finishing the TCO and metallization, photo-conductance (PC) measurements are a valuable option [87, 88]. The measurements are performed using a Sinton Consulting WCT-120 setup. Spacially uniform distributed excess charge carriers are generated by a short light pulse in the wafer which increases the electrical conductivity of the material. The excess carriers recombine with the recombination rate (U) which can be expressed as $U = \Delta n/\tau_{\mathrm{eff}}$ with the effective minority carrier lifetime (τ_{eff}). The recombination happens mostly due to impurities and crystal defects in the bulk of the silicon and surface recombination originating from open silicon bonds at the surface of the wafer. Due to the use of high quality crystalline silicon the bulk recombination rate is usually small as compared to the surface recombination rate. The change in Δn_{e} with time can be expressed as the difference between generation rate (G) and U [89]

$$\frac{\mathrm{d}}{\mathrm{d}t}\Delta n_{\mathrm{e}} = G - U = G - \frac{\Delta n_{\mathrm{e}}}{\tau_{\mathrm{eff}}}. \tag{3.2}$$

The effective minority carrier lifetime can then be written as

$$\tau_{\mathrm{eff}} = \frac{\Delta n_{\mathrm{e}}(t)}{G(t) - \frac{\mathrm{d}}{\mathrm{d}t}\Delta n_{\mathrm{e}}}. \tag{3.3}$$

The PC measurement can be performed in two different modes depending on τ_{eff}. For short $\tau_{\mathrm{eff}} < 300$ µs the measurement is performed in the quasi-steady state mode (QSS). In QSS the light pulse needs to be well longer than τ_{eff} and is usually set to 1 ms. Thereby the measurement is performed in the steady state and $\frac{\mathrm{d}}{\mathrm{d}t}\Delta n_{\mathrm{e}}$ is assumed to be 0. For QSS measurements the generation rate needs to be measured using a photodiode.

For longer lifetimes $\tau_{\mathrm{eff}} > 300$ µs the measurement is performed in the transient mode using a very short light pulse (1/64 ms). Therefore, the generation rate during the measurment is assumed to be $G = 0$. The measurement gives the τ_{eff} as a function of Δn_{e}. The documented τ_{eff} value is usually extracted at $\Delta n = 10^{15}$ cm^{-3}. Another representation of the passivation quality which will be frequently used is the implied open circuit voltage (iV_{oc}) [87, 90]. The iV_{oc} is the upper limit for the V_{oc} of the final device. The iV_{oc} can already be evaluated before the solar cell has metal contacts. It can therefore be monitored after each process step of the solar cell. The iV_{oc} can be calculated form Δn by

$$iV_{\text{oc}} = \frac{\text{k}_{\text{B}}T}{\text{q}} \ln\left(\frac{(\Delta n_{\text{e}} + N_{\text{A}})\Delta n_{\text{e}}}{n_{\text{i}}^2}\right). \tag{3.4}$$

A third representation of the passivation quality is the J_0, which is also extracted from the PC measurements. The J_0 can be extracted from the slope of the inverse lifetime [91]

$$J_0 = \frac{1}{2}\,\text{q}W n_{\text{i}}^2\,\frac{\text{d}}{\text{d}\Delta n_{\text{e}}}\left(\frac{1}{\tau_{\text{corr}}}\right) \tag{3.5}$$

with

$$\frac{1}{\tau_{\text{corr}}} = \frac{1}{\tau_{\text{eff}}} - \frac{1}{\tau_{\text{Auger}}} - \frac{1}{\tau_{\text{rad}}} \tag{3.6}$$

and with the thickness of the wafer (W), the lifetime due to Auger recombination (τ_{Auger}), and the lifetime due to radiative recombination (τ_{rad}). The fitting is performed around $\Delta n_{\text{e}} = 5 \times 10^{15}$ cm^{-3}.

Photoluminescence (PL) PL is a versatile imaging technique to obtain spatially resolved information about solar cells. Luminescence imaging was first used in 2005 by Fuyuki et al. to image silicon solar cells [92]. Charge carriers can be exited in the solar cell either by a light pulse (photo-luminescence) or by injecting a current (electro-luminescence). For photo-luminescence (PL) measurements in this work the solar cells are operated at open circuit, thus all exited charge carriers need to recombine. The luminescence thereby describes the radiative part of the recombination. As described in Section 2.2 non-radiative recombination is the dominating recombination mechanism in silicon solar cells. Therefore, a high luminescence signal of the solar cell corresponds to high radiative and a suppressed non-radiative recombination which is highly desired for silicon solar cells.

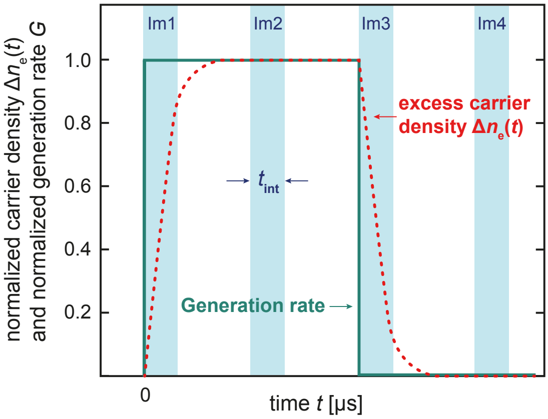

Figure 3.1.: *Schematic measurement procedure for dynamic PL measurements to determine the spatially resolved minority carrier lifetime. The generation profile is shown as the green solid line and the excess carrier density as the red dotted line. Four images are taken at a rising, a stable, a falling, and a dark excess carrier density to calculate the lifetime corrected PL image. Each image is integrated over the integration time* t_{int}.

In analogy to the PC measurements PL measurements can also be performed in a quasi-steady state mode [93] and dynamic mode [94,95]. Using the dynamic PL the effective minority carrier lifetime can be obtained without calibration of the light intensity [94]. For the dynamic measurement four images need to be taken during one illumination cycle (see Figure 3.1). The first image is taken when the light switches on (Im1), the second when the light has stable illumination (Im2), the third when the light is switched off (Im3) and the fourth image is taken in the dark (Im4). This cycle is repeated typically 100 – 250 times and each individual image is summed up to increase the signal-to-noise ratio. The final image (I_{PL}) can then be calculated by $I_{\mathrm{PL}} = \frac{Im2-Im4}{Im1-Im3} = \frac{I_{\mathrm{static}}}{I_{\mathrm{dynamic}}}$ and is proportional to $I_{\mathrm{PL}} \propto \Delta n_{\mathrm{e}}(\Delta n_{\mathrm{e}} + N_{\mathrm{D}})$ [96]. From Equation 3.2 assuming an time-independent τ_{eff} it follows [94]

$$\Delta n_{\mathrm{e}} = G\tau_{\mathrm{eff}}\left(1 - \exp\left(-\frac{t}{\tau_{\mathrm{eff}}}\right)\right). \tag{3.7}$$

Integrating Equation 3.7 over the integration time of the PL image (t_{int}) for the static and the dynamic image results in

$$I_{\mathrm{PL}} = \frac{t_{\mathrm{int}}}{t_{\mathrm{int}} + \tau_{\mathrm{eff}}\, \exp(-\frac{t_{\mathrm{int}}}{\tau_{\mathrm{eff}}}) - \tau_{\mathrm{eff}}}. \tag{3.8}$$

From Equation 3.8 it can be seen that the final PL image only depends on τ_{eff} and t_{int}, thus, does not need any calibration. Further details about dynamic PL can be found in literature [94, 95, 97, 98]. A more general description of electro- and photo-luminescence was developed by U. Rau [99] which also holds for cases where the solar cell is not operated in open circuit as performed in this work.

For the measurements in this work the images are taken by an Xenics Cheetah 640-CL InGaAs camera which is cooled to 0 °C. The samples is illuminated by an LED array for 200 ms followed by a 1 s delay.

Transfer Length Method (TLM) The transfer length method which can be also found as the «transmission line method» is used to determine the contact resistivity (ρ_{c}) of a layer stack. The layer stack is contacted by 8 silver contact pads which have a decreasing spacing between the contacts. The current has to flow through all contact layers and then laterally through the crystalline silicon which has the lowest sheet resistance of the layers. Between each adjacent contacts the resistance is measured and plotted as a function of the contact distance. This resistance R then comprises of the contact resistance R_{c} and the lateral resistance of the silicon $R_{\mathrm{Si}} = \rho_{\mathrm{Si}}\, d_{\mathrm{cont}}$ where ρ_{Si} is the specific resistivity of the doped silicon and d_{cont} is the distance between the contacts.

$$R = 2R_{\mathrm{c}} + \rho_{\mathrm{Si}}\, d_{\mathrm{cont}} \tag{3.9}$$

The measured data can then be linearly extrapolated to $d_{\mathrm{cont}} = 0$, which gives $R = 2R_{\mathrm{c}}$. The contact resistance then comprises of the specific resistivities of each layer times the layer thickness as well as the resistances at the interfaces between the layers. So $R_{\mathrm{c}} = 2 \times (R_{\mathrm{SiO2}} + R_{\mathrm{SiC}} + R_{\mathrm{SiC/TCO}} + R_{\mathrm{TCO}} + R_{\mathrm{TCO/Ag}} + R_{\mathrm{Ag}})$ as it can be seen in Figure 3.2. To mitigate a parasitic resistance between the probes and the contacts a four-point-probe measurement is performed. Details regarding TLM measurements can be found in [100, 101].

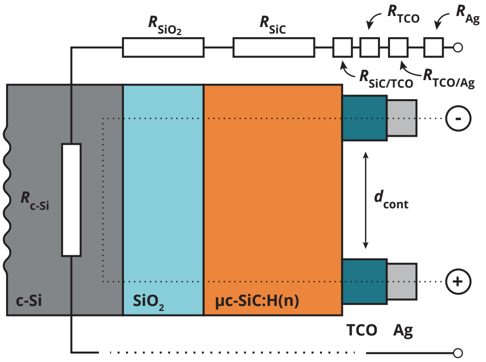

Figure 3.2.: *Measurement of the contact resistivity by TLM. Exemplary using structured TCO to define the contact distance d_{cont}. It should be noted that the R_{SiO2} is not an ohmic resistance but originates from the charge carrier tunnel probability through the SiO_2. Dashed line represents the current path trough the layer stack. White boxes represent the individual resistances of the layers and interfaces.*

Solar simulator The current density-voltage (JV) curve is measured in the commercial AAA class sun simulator LOANA provided by pv-tools. As a LED light source a wavelabs Sinus 120 is used. The measurements are performed under standard test conditions: power of the incoming sunlight $P_{\mathrm{sun}} = 1000\ \mathrm{W/m^2}$, a spectrum of AM1.5 and 25 °C cell temperature. A solar cell can be described using an equivalent circuit as presented in Figure 3.3 (a) which can be expressed using a diode equation

$$J(V) = J_0 \exp\left(\frac{\mathrm{q}(V - R_{\mathrm{s}}J)}{k_{\mathrm{B}}T} - 1\right) + \frac{V - R_{\mathrm{s}}J}{R_{\mathrm{sh}}} - J_{\mathrm{ph}} \tag{3.10}$$

with R_{s} which is the sum of the contact resistance and the bulk resistance of the material, shunt resistance (R_{sh}) and J_{ph} which is generated by the absorbed sunlight. Under illumination the measured curve is prepresented by the light-JV curve in Figure 3.3 (b). This curve has some characteristic values which are used to describe the solar cell performance. The short circuit current density (J_{sc}) is the maximum current density which can be drawn from a solar cell at 0 V. The open circuit voltage (V_{oc}) is voltage when no current is flowing. The power conversion efficiency (η) of a

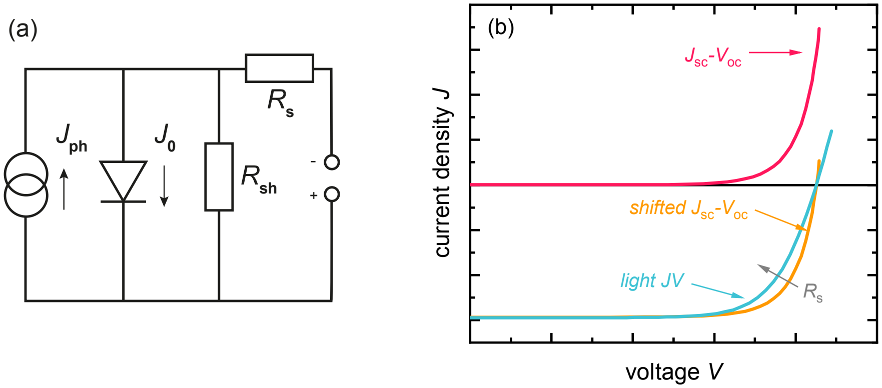

Figure 3.3.: *(a) One diode equivalent circuit of a solar cell with a generator, a diode, and two resistors. The generator generates the photo-current density (J_{ph}) while the diode is characterized by the saturation current density (J_0). One the shunt resistance (R_{sh}) is in parallel to the diode and the generator while the series resistance (R_s) is in series. (b) J_{sc}–V_{oc} curve (red), J_{sc}–V_{oc} shifted by J_{sc} (orange) and light-JV curve at one sun illumination (blue). The pFF is the FF of the shifted J_{sc}–V_{oc} curve (orange). The R_s is obtained by applying it to the shifted J_{sc}–V_{oc} until it matches the light-JV curve.*

solar cell is defined as

$$\eta = \frac{P_{\text{max}}}{P_{\text{sun}}}. \tag{3.11}$$

It is calculated from the maximum power generated by the solar cell (P_{max}) at the point where the product of J and V is at its maximum and power of the incoming sunlight (P_{sun}). From the quotient of maximum power of the solar cell (P_{max}) and $J_{\text{sc}}V_{\text{oc}}$ the fill factor (FF) is calculated $FF = P_{\text{max}}/(J_{\text{sc}}V_{\text{oc}})$. The efficiency can then be described as

$$\eta = \frac{J_{\text{sc}}V_{\text{oc}}FF}{P_{\text{sun}}}. \tag{3.12}$$

Further information may be found in [102]. Another important measure for solar cells is the pFF. The pFF is similar to the FF but without the influence of the series resistance of the solar cell. To obtain the pFF J_{sc}–V_{oc} measurements are used [103]. The J_{sc} and V_{oc} values are measured at varied light intensities. J_{sc}–V_{oc}

curves do not show an effect of the series resistance, since R_s is neither effecting the V_oc nor the J_sc when the $R_\mathrm{s} < 10\,\Omega\,\mathrm{cm}^2$. The J_sc–V_oc curve is similar to the JV curve without illumination of the solar cell (dark-JV curve). The difference between dark-JV and J_sc–V_oc curve is that the latter is not influenced by the R_s. When shifting the J_sc–V_oc curve by J_sc at one sun illumination a shifted J_sc–V_oc (pseudo light-JV) curve is obtained (see Figure 3.3 red to orange). The pFF is then the FF of this shifted J_sc–V_oc curve. By applying R_s to this shifted J_sc–V_oc the light-JV curve (see Figure 3.3 blue) can be matched.

Quantum-efficiency and reflection measurements For external quantum efficiency (EQE) and reflectance (R) measurements the LOANA system by pv-tools is used. EQE measurements provide valuable insight into the absorption and charge carrier extraction of solar cells as a function of the wavelength of the incident light. For the measurement calibrated monochromatic light is step-wise illuminated onto the solar cell. The thereby generated current is measured. Due to the very low currents the measurement is performed using lock-in amplifiers. The number of photons per wavelength interval is known due to the calibration. The EQE is a measure of the collected charge carriers divided by the number incident photons. The internal quantum efficiency (IQE) is the number of collected charge carriers divided by the number of absorbed photons. Therefore, the number of reflected photons is subtracted from the number of incident photons $IQE = EQE/(1 - R)$. The reflection measurements are done on the same spot as the EQE measurements using an Ulbricht sphere. The default sport size for both measurements is 12×12 mm^2.

For the development of a front side transparent passivating contact the information in the blue wavelength range a especially interesting. If the front side layer show a high parasitic absorption of the incident light the quantum efficiency is typically reduced in the short wavelength range. For the optimization of the front side anti-reflection coating reflection measurements in the short wavelength range reveal the effectiveness of the coating.

The JV parameters and the quantum efficiency of the best solar cell in this work was independently certified by CalTeC at the ISFH.

4. Wet-chemically grown SiO_2 Tunnel Oxides

In this Chapter the focus will be set on the investigation of selected wet-chemically grown SiO_2. Parts of this Chapter are already published elsewhere [104]. The SiO_2 is needed in the TPC as an intermediate buffer layer to protect the c-Si surface against damage during the HWCVD µc-SiC:H(n) deposition. SiO_2 is a well known and intensively studied material, which is widely used in the semiconductor industry. Silicon oxide can be fabricated in two ways: by deposition on a substrate (e.g. by PECVD [105, 106] or HWCVD [107]) or by oxidation of crystalline silicon (wet-chemical or thermal oxidation). In this work a focus was set to *wet-chemical* oxidation of c-Si because of the necessity for very thin tunnel SiO_2. Wet-chemical oxidation is a self-limiting process, which usually results in oxide thicknesses $d_{\mathrm{SiO2}} < 2$ nm. This is necessary for effective quantum-mechanical tunneling of charge carriers through the oxide [108]. Additional advantages of the wet-chemical oxidation are the high possible throughput and the low processing temperature compared to thermal oxidation [109]. The possibility to use wet-chemically grown SiO_2 as buffer layer in TPCs was already shown by Ding et al. [110] and Pomaska in his PhD thesis [10] using SiO_2 grown in concentrated HNO_3. Nevertheless, no intensive study about different wet-chemical oxidation methods to form the SiO_2 for TPCs has been shown.

For the TPC to function as a well passivating contact the recombination at the surface needs to be suppressed. To minimize the recombination rate at the c-Si/SiO_2 interface four aspects are of major importance.

(i) The surface of the c-Si has to be as clean as possible [65, 111]. Contamination by particles, metal, and organic residues can reduce the passivation quality.

(ii) The dangling bond density at the surface of the c-Si should be as low as possible [112–114]. The density of dangling bonds can be quantified by D_{it}.

(iii) The fixed charge density (Q_{fix}) has to have the correct polarity to enhance the field effect passivation of the contact [75, 113, 114]. Fixed charges in the oxide can occur due to interface-trapped charges or stoichiometric inhomogeneities in the SiO_2.

(iv) The stoichiometry density of SiO_2 should be as high as possible to achieve a high passivation quality [81, 115].

To clean the wafers from contamination (i) prior to formation of the wet-chemical tunnel oxide a special cleaning procedure was used. The procedure was developed by the Radio Cooperation of America RCA in 1965 and published in 1970 [65, 111]. The cleaning involves oxidation in a mixture of ammonia (NH_3) and H_2O_2, also frequently referred to as Standard Clean 1 (SC-1), which removes particles and organic residues. Following, the wafer is oxidized in a mixture of hydrochloric acid (HCl) and H_2O_2, which is also frequently referred to as Standard Clean 2 (SC-2) and removes metallic residues. The residual oxide from the RCA process is then stripped off in 1% hydrofluoric acid (HF) prior to formation of the oxide. This cleaning process was applied to all wafers prior to SiO_2 formation.

The influence of selected oxidation methods and solutions on the surface properties of silicon was intensively studied by Yamashita et al., Angermann et al., and Moldovan et al. [79, 81, 112, 115–119]. Yamashita et al. found that some oxidation solutions can result in an increased or decreased surface roughness compared to the initial roughness of the wafer (ii) [116]. Increasing the surface roughness of the c-Si also increases the D_{it}. It was also found that the wet-chemical oxidation solution has an influence on the polarity and the density of the fixed charges (iii) [118]. While oxidation in nitric acid (HNO_3), diluted hydrochloric acid (HCl), Standard Clean 2 (SC-2), and a mixture from sulfuric acid with hydrogenperoxide

H_2SO_4:H_2O_2 (piranha) result in a positive fixed charge density on n-type doped silicon, oxidation in Standard Clean 1 (SC-1) results in negative fixed charges [118]. The polarity of the fixed charges is of importance, since it either enhances or suppresses the electrical potential at the interface. In an n-type selective contact the majority carriers, which have to be extracted, are electrons. A negative fixed charge density at the n-type selective contact interface repels electrons and attracts holes, which increases the recombination. Therefore, n-type contacts using SiO_2 prepared in SC-1 solution should have a lower passivation quality than oxides with a negative Q_{fix} if all other influencing parameters are equal.

A factor which was found to influence the passivation quality of SiO_2/poly-Si passivated samples is the stoichiometry of the tunnel oxide (iv). Moldovan et al. found that a higher stoichiometry (less sub-stoichiometric oxide) of the oxide leads to a higher passivation quality [81, 115]. It was found that oxides with lower stoichiometry (more sub-stoichiometric oxide) show disruptions in the SiO_2 layer while oxides with higher stoichiometry do not show disruptions [81]. However, these disruptions where found after high temperature annealing (900 °C), which is necessary to fabricate poly-Si contacts. High temperature annealing is not necessary for SiO_2/µc-SiC:H(n) contacts. Nevertheless, the stoichiometry might also influence the quality of the TPC, since the SiO_2 needs to be stable against the HWCVD deposition.

In the case of the TPC, the silicon oxide has to fulfill the requirements for high passivation listed above ($i - iv$), to preserve a high passivation quality. Nevertheless, the contact also has to be conductive for the majority carriers, which have to flow through the layers into the metal electrodes. The resistance for the majority carriers of the contact can be measured as the contact resistivity (ρ_{c}). The contact resistance is composed of the resistances of each layer and the resistances at the interfaces as sketched in Figure 3.2. Since the SiO_2 is electrically isolating no charge carriers could get trough the SiO_2 in a classical description. However, if the potential barrier is thin enough the charge carrier transport can be described by quantum mechanics, which allows tunneling through the SiO_2. To calculate the tunnel probability for charge carriers through the SiO_2 the Schrödinger equation needs to be solved. Solving the Schrödinger equation for a rectangular potential barrier, which is the easiest description the quantum mechanical tunnel probability $T(E)$, can be described as [120]

$$T(E) \propto \exp(-d_{\mathrm{SiO2}}\, k) \tag{4.1}$$

where

$$k = \sqrt{\frac{2\, m_{\mathrm{t}}}{\hbar^2}\Phi} \tag{4.2}$$

with the tunneling mass (m_{t}), the height of the potential barrier of SiO_2 (Φ), and reduced Planck constant ($\hbar$). It should be noted that the trapezoidal shape of the SiO_2 barrier was disregarded in this example. Equation 4.1 shows that $T(E)$ exponentially depends on thickness of silicon oxide layer (d_{SiO2}). A small decrease of the oxide thickness exponentially improves the tunnel probability. To enable a sufficient $T(E)$, the oxide thickness should be below 2 nm [108]. However, it has also been shown e.g. by Peibst et al. that very low contact resistivities can be achieved using SiO_2 with a thickness larger than 2 nm [121] and a poly-Si layer. Peibst et al. used a high temperature annealing ~1000 °C to crystallize the poly-Si layer. This annealing most likely disrupts the SiO_2 locally and results in a direct contact between poly-Si and c-Si, which is often described as «pinholes». These pinholes provide a direct current path for the charge carriers through the oxide layer. Evidence for these pinholes in contacts annealed at high temperatures have been found by several research groups [122–124]. Nevertheless, it remains unclear if these pinholes also occur in contacts like the TPC, which are not annealed at high temperatures after deposition of the doped layer.

The purpose of this Chapter is to find the best oxidation solution and the best oxidation parameters to fabricate the SiO_2 for the TPC. Therefore, in the first Section the oxidation time and the oxide thickness is investigated regarding the passivation quality as well as the contact resistivity. In the second Section of this Chapter the influence of different filament temperatures during HWCVD on selected SiO_2 is investigated.

4.1. Influence of oxidation parameters

Growth Rates To find the ideal oxidation solution, which results in high passivation quality and low contact resistivity, five different chemical solutions are tested as described in detail in Section 3.1:

1. concentrated nitric acid (HNO_3),
2. a mixture from sulfuric acid with hydrogenperoxide H_2SO_4:H_2O_2 (piranha),
3. Standard Clean 1 (ammonium hydroxide (NH_4OH):H_2O_2),
4. Standard Clean 2 (HCl:H_2O_2),
5. diluted HCl in water (HCl:H_2O).

Some wafers are only rinsed in DI-H_2O after the removing of the RCA oxide in 1% HF, dried in atmosphere with nitrogen, and then transported to the measurement and deposition systems. During this time a native oxide already grows, which is marked as «native» oxide. In Figure 4.1 the thickness of the SiO_2 (d_{SiO2}) is plotted as a function of the oxidation time (t_{ox}) for the selected wet-chemical oxidation methods. The thickness of the SiO_2 is derived from spectral ellipsometry (SE) measurements. The oxide thickness measured for the unintentionally oxidized sample («native») is 0.5 nm. The oxide thickness of the native oxide depends on many factors e.g. the oxygen concentration in the DI-H_2O and the moisture of the ambient air [112, 125]. After 2 sec in HNO_3 the thickness of silicon oxide layer is already increased to 1 nm (see Figure 4.1). The thickest oxide is produced after 10 min in HNO_3 solution with $d_{\mathrm{SiO2}} = 1.4$ nm.

The oxidation in piranha solution does not show a significant dependency on the oxidation time. For $t_{\mathrm{ox}} = 15$ sec to 12.5 min the oxide thickness is in the range of 0.9 nm. To investigate the impact of a negative Q_{fix} on the passivation quality oxidation in SC-1 solution is also studied. The d_{SiO2} for 15 min SC-1 oxidation is 1 nm. For SC-2 d_{SiO2} can be increased from 0.6 nm to 0.9 nm by increasing t_{ox} from 15 min to 30 min. For HCl:H_2O the oxidation is the slowest of all oxidation solutions. Thicknesses above 0.5 nm can only be achieved for $t_{\mathrm{ox}} > 30$ min. The thickest oxide prepared with HCl:H_2O is found to be 0.7 nm for $t_{\mathrm{ox}} = 120$ min. The oxide thickness can not be increased further for $t_{\mathrm{ox}} = 300$ min. The reason

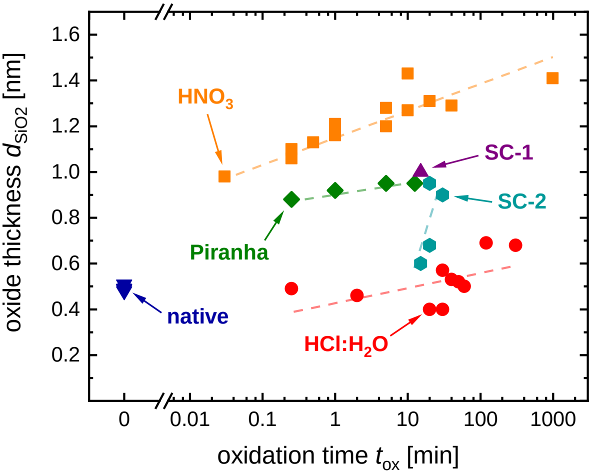

Figure 4.1.: *Oxide thickness (d_{SiO2}) for oxides grown in 69% HNO_3 at room temperature, in 1% HCl at 80 °C, SC-1, SC-2 & piranha at 60 °C. The native oxide was added as a reference. The thickness of the SiO_2 was measured using spectral ellipsometry (SE) on polished wafers. The data for HNO_3 oxidation was originally published in [10]. Dashed lines are guides to the eye.*

that the oxide thickness cannot be increased after a certain thickness is due to the self-limiting nature of the oxidation. In contrast to deposited SiO_2 the oxide is not growing on top of the wafer but rather into the wafer. During the wet-chemical oxidation an oxygen atom is inserted either into a Si–Si back bond or into a Si–H bond at the surface depending on the oxidation solution and the resulting chemical reaction. Intensive studies of possible oxidation reactions for e.g. HNO_3, H_2O_2, and H_2SO_4 are performed by Patzig-Klein [82]. Since the diffusion of the oxide species into the wafer and through the already grown SiO_2 is limited, the thickness of the wet-chemically grown SiO_2 is also limited. The thickness of the SiO_2 therefore depends on the oxidation reaction and on the temperature of the oxidation solution. Details can be fond in the Fundamentals Section 2.4

Passivation To investigate the passivation quality of the individual oxides, photoconductance measurements are performed directly after oxidation. Due to very low minority carrier lifetimes (<50 µs) of all oxidized samples no conclusive results can be obtained without any additional passivating layer. Therefore, a ∼40 nm thick µc-SiC:H(n) layer is deposited at $T_\mathrm{f} \sim 1800$ °C on both sides of the wafer. The results of the passivation quality in terms of iV_oc can be seen in Figure 4.2. It should be noted that the samples used for HNO_3 experiments have been prepared on textured silicon wafers while all other experiments were conducted on polished silicon wafers. Since the surface area fraction of textured surfaces is higher than for polished silicon chemical passivation is expected to be less effective. This effect can be seen for the native oxide after HF dip and DI-H_2O rinse. While for the polished wafers the iV_oc 676 mV and 683 mV, the iV_oc of the textured sample is 537 mV. Nevertheless, the difference between polished and textured wafers is only evident for the samples with native oxide. After 15 sec of HNO_3 treatment the iV_oc is on the same level as for the polished samples. For t_ox between 15 sec and several hours in HNO_3 no correlation between oxidation time and passivation quality can be seen. The mean iV_oc of the selected oxidation solutions can be found in Table 4.1. It can be seen that for a µc-SiC:H(n) layer deposited at $T_\mathrm{f} = 1800$ °C, the piranha oxide shows the highest mean iV_oc of 702 mV. While oxidation in HNO_3 results in iV_oc of 694 mV and HCl:H_2O of 692 mV, lower passivation qualities are found for SC-2 oxide with $iV_\mathrm{oc} = 689$ mV and SC-1 of 671 mV.

Table 4.1.: *Mean implied open circuit voltage (iV_{oc}) results for selected oxidation solutions to form the SiO_2 after deposition of the µc-SiC:H(n).*

Oxidation solution	mean iV_oc [mV]
piranha	702 ± 10
HNO_3	694 ± 9
HCl:H_2O	692 ± 9
SC-2	689 ± 18
SC-1	671

These results lead to the conclusion that the highest and lowest passivation quality can be achieved for oxidation in piranha and SC-1 solution, respectively.

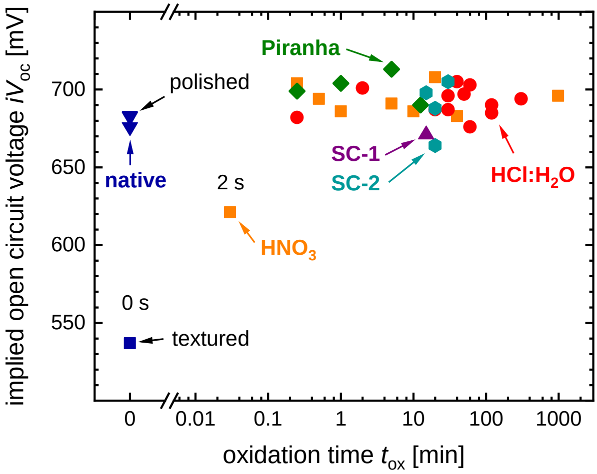

Figure 4.2.: *Implied open circuit voltage (iV_{oc}) as a measure of the passivation quality for oxides grown in 69% HNO_3 at room temperature, for 1% HCl at 80 °C, SC-1, SC-2 & piranha at 60 °C. The native oxide was added as a reference. The thickness of the SiO_2 was measured using spectral ellipsometry (SE) on polished wafers. The iV_{oc} was measured on samples with additional µc-SiC:H(n) layer. The data for HNO_3 oxidation was originally published in [10].*

Additionally, it is found that for textured wafers an intentionally grown SiO_2 is necessary to achieve a high passivation quality while the native oxide cannot provide a high iV_{oc}. Nevertheless, no decrease in passivation quality is observed for longer oxidation times. This indicates that longer oxidation does not increase the density of interface states (*ii*) significantly. Longer oxidation times might instead lead to a more stoichiometric silicon oxide (*iv*).

To investigate the influence of the different oxide thicknesses on the passivation quality and the contact resistivity the iV_{oc} and ρ_c are plotted as a function of d_{SiO2} in Figure 4.3 and Figure 4.4. All samples have been prepared on dsp c-Si(n) <111> wafers, since the faces of the random pyramids of textures wafers are also <111> planes. Two different MMS flow rates (4 sccm, 6 sccm) are used during HWCVD deposition, since for the higher flow rate a high series resistance of the solar cells was

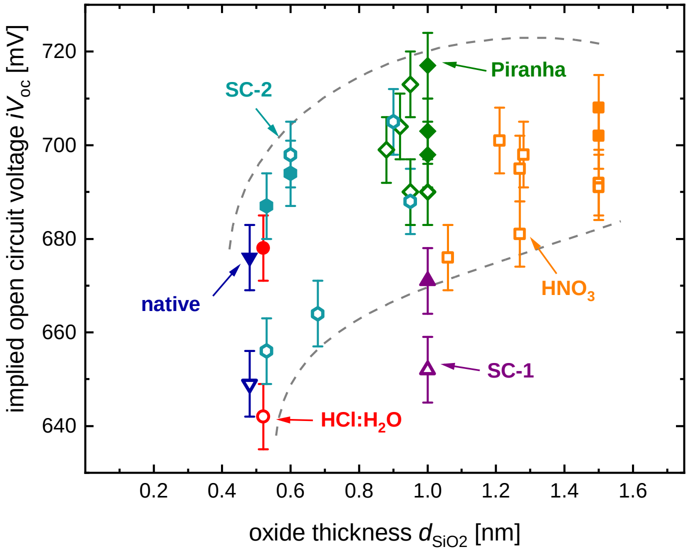

Figure 4.3.: *Implied open circuit voltage (iV_{oc}) for oxides grown using HNO_3 solution at room temperature (orange squares), for 8% HCl at 80 °C, SC-1 at 60 °C, SC-2 at 60 °C, piranha at 60 °C, and native oxide. The dashed lines are guides to the eye. For open symbols the µc-SiC:H(n) is deposited using an MMS flow of 4 sccm resulting in higher conductivity of the layer. For closed symbols the µc-SiC:H(n) is deposited using an MMS flow of 6 sccm resulting in lower conductivity of the layer. Adapted with permission from [104]. Copyright 2018 American Chemical Society.*

found in literature, which might be due to a low conductivity (σ) of the µc-SiC:H(n) [10]. A lower MMS flow rate results in a higher σ of the µc-SiC:H(n) [10].

It can be seen in Figure 4.3 that the iV_{oc} is influenced by the oxidation solution and the thickness of the oxide up to $d_{SiO2} < 0.9$ nm. In this range the lower MMS flow rate (open symbols) also result in lower iV_{oc} compared to the higher MMS flow rate (full symbols). For thicker oxides the different HWCVD deposition conditions seem to have less influence on the passivation quality. Oxidation in piranha solution results in the highest passivation quality of all oxides with a maximum iV_{oc} of 714 mV for d_{SiO2} of 1 nm. Higher oxide thicknesses can only be obtained by HNO_3 solution, which nevertheless does not exceed the passivation quality of the samples prepared with the piranha oxide. For samples prepared with HNO_3 the maximum iV_{oc} is

708 mV while the maximum iV_{oc} for SC-2 oxidized samples is 705 mV.

The oxide prepared with SC-1, which has a negative Q_{fix}, shows significantly lower passivation quality than the samples with an equal d_{SiO2} prepared by piranha solution. The reason for that might be the reduced field effect passivation due to the negative Q_{fix}, which repels the majority carriers and attracts the minority carriers instead. Additionally, lower MMS flow rates lead to a further reduction of the iV_{oc}. Therefore, low MMS flow rates seem to be more critical for the SC-1 oxide compared to the piranha oxide even though the oxide thicknesses are equal.

Yamashita et al. investigated the influence of different oxidation solutions on the oxide parameters: root mean squared roughness (R_{ms}), defect density at the c-Si interface (D_{it}), and atomic density of the SiO_2 (ρ_{SiO2}) for SiO_2 grown on c-Si <111> [116]. The results are shown in Table 4.2. They found that oxidation in boiling HNO_3 solution (115 °C) results in an increased root mean squared roughness (R_{ms}) while oxidation in piranha or SC-2 solution results in a decreased R_{ms} compared to the roughness before oxidation (see Table 4.2). They also found that the defect density at the c-Si interface (D_{it}) strongly depends on the R_{ms} and thereby on the oxidation method. The results show that the lowest D_{it} of $0.48{\times}10^{12}$ cm^{-2} was found for the oxide prepared by SC-2 solution. The D_{it} of SiO_2 prepared by piranha solution was found to be $1.3{\times}10^{12}$ cm^{-2} and for SiO_2 prepared by HNO_3 the D_{it} was $1.8{\times}10^{12}$ cm^{-2}. When only taking into account the R_{ms} this would lead to the conclusion that the oxide prepared using SC-2 should result in the highest passivation quality. However, this result is not observed.

Additionally, Yamashita et al. found that the oxide density of the SC-2 with $\rho_{\mathrm{SiO2}} = 2.01{\times}10^{22}$ cm^{-3} oxide is lower than for the oxides prepared with HNO_3 or piranha with $\rho_{\mathrm{SiO2}} = 2.21{\times}10^{22}$ cm^{-3}. Similar results were found by Sugita et al. on c-Si <100> where the ρ_{SiO2} of piranha oxide was even denser than ρ_{SiO2} of HNO_3 oxide [126]. These results suggest that the passivation quality of the SC-2 oxide might be lower due to a lower oxide density. One reason for that might be the conditions during HWCVD deposition of µc-SiC:H(n). Due to a high dilution of MMS with molecular hydrogen (H_2) a large amount of atomic hydrogen radicals are created at the hot-wire filaments. These radicals are known to etch e.g. crystalline silicon and deteriorate the passivation [127–129]. Therefore, it is possible that oxides with a lower density might be damaged or removed easier than oxides with a higher density. This finding would explain the lower passivation quality of the SC-2 oxide despite the lower D_{it}. Additionally, this assumption is supported by the finding that thinner oxide layers generally show lower passivation qualities than oxide layers with a thickness $d_{\mathrm{SiO2}} > 0.9$ nm. Thinner oxides are more likely do be removed by atomic hydrogen than thicker oxide, which then leads to a deterioration of the c-Si surface. SiO_2 prepared in HNO_3 solution shows an equal oxide density but a higher D_{it} than SiO_2 prepared by piranha in the data by Yamashita et al. which might explain the inferior passivation.

Additionally, it should be noted that the oxidation temperatures in the publication of Yamashita et al. were 90 °C higher for HNO_3 SiO_2 and only 30 °C higher for piranha oxide. The ρ_{SiO2} of HNO_3 might be lower when prepared at room temperature, since in literature it is shown that thermal treatments of the HNO_3 oxide lead to a densification of the SiO_2 [130, 131]. The higher D_{it} and the possibly lower ρ_{SiO2} for HNO_3 oxide compared to piranha oxide might be the reason for the lower passivation quality for HNO_3 prepared SiO_2.

It was additionally found that the fixed charge density of samples prepared in HNO_3 and piranha solution are comparable [132, 133]. These measurements have been performed using corona charging of c-Si/SiO_2 samples, which was capped by an Al_2O_3 layer. Therefore, an influence of the fixed charges on the passivation of these two oxides is unlikely.

Table 4.2.: *Root mean squared roughness (R_{ms}) of the wafer after removing the specific oxide. The initial R_{ms} before oxidation was 0.19 nm. The defect density at the c-Si interface (D_{it}) and atomic density of the SiO_2 (ρ_{SiO2}) for SiO_2 prepared by SC-2, piranha, and HNO_3 is given. The data is reported by Yamashita et al. [116].*

		SC-2	piranha	HNO_3
R_{ms}	[nm]	0.152	0.18	0.195
D_{it}	[$\times 10^{12}$ cm^{-2}]	0.48	1.3	1.8
ρ_{SiO2}	[$\times 10^{22}$ cm^{-3}]	2.01	2.21	2.21

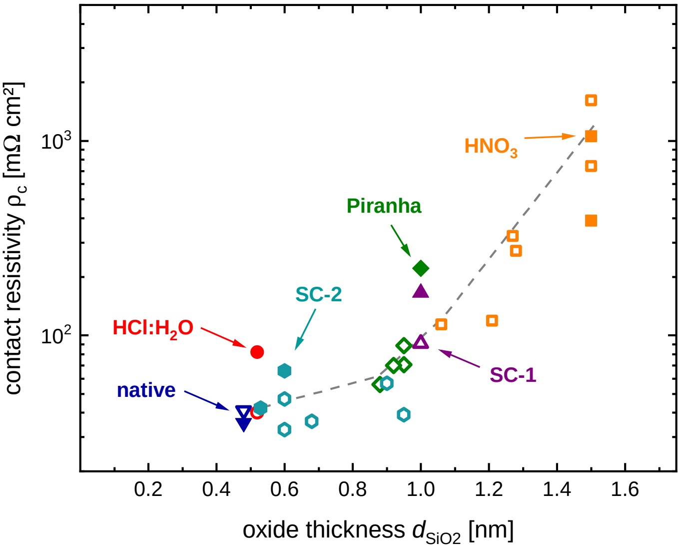

Figure 4.4.: *Contact resistivity (ρ_c) for oxides grown using HNO_3 solution at room temperature (orange squares), for 8% HCl at 80 °C, SC-1 at 60 °C, SC-2 at 60 °C, piranha at 60 °C, and native oxide. The dashed lines are guides to the eye. For open symbols the µc-SiC:H(n) is deposited using an MMS flow of 4 sccm resulting in higher conductivity of the layer. For closed symbols the µc-SiC:H(n) is deposited using an MMS flow of 6 sccm resulting in lower conductivity of the layer. Adapted with permission from [104]. Copyright 2018 American Chemical Society.*

Contact Resistivity Besides a high passivation quality it is important that the TPC also enables the electrons to flow into the metallic contacts. Therefore, the conductivity of the µc-SiC:H(n) has to be sufficient and the SiO_2 has to be thin enough to enable efficient quantum mechanical tunneling of the charge carriers. To investigate the influence of the conductivity of the µc-SiC:H(n) and the influence of the tunnel oxide thickness the contact resistivity (ρ_c) was calculated from measurements using the transfer length method (TLM). The results are plotted in Figure 4.4. It can be seen that the ρ_c is increasing between $d_{SiO2} = 0.5$ nm – 1 nm from 35 mΩ cm^2 to 100 mΩ cm^2 and increasing more strongly between $d_{SiO2} = 1$ nm – 1.5 nm up to 1000 mΩ cm^2. The increased electrical conductivity of the µc-SiC:H(n) due to the decreased flow rate of monomethylsilane gas (F_{MMS}) has no significant influence on the HNO_3 oxide at $d_{SiO2} = 1.5$ nm and only a slight influence on the oxides around $d_{SiO2} = 0.6$ nm. The dominating transport mechanism for TPC with d_{SiO2} between 1 nm − 1.5 nm is likely to be quantum mechanical tunneling through the oxide since the slope of ρ_c is increasing exponentially with d_{SiO2}. For thinner oxides the exact transport mechanism is not fully understood. One possibility is that small disruptions within the thin oxide layer might directly conduct the electrons. The dominating transport mechanism might be revealed using temperature dependent ρ_c measurements in future experiments as proposed by Folchert et al. [134].

It can be concluded that the best passivation quality with iV_{oc} of 717 mV can be achieved for a 1 nm thick SiO_2 prepared in piranha solution with subsequently deposited µc-SiC:H(n). This sample has a contact resistivity of 220 $\mathrm{m\Omega\,cm^2}$. Using the SC-2 oxide, which had an oxide thickness of 0.6 nm, results in the lowest contact resistivity of 33 $\mathrm{m\Omega\,cm^2}$ and an iV_{oc} of 689 mV.

Conductivity through disruptions in the oxide A possibility to describe the current transport through the oxide could be e.g. «pinhole conduction». Pinholes in the SiO_2 were already visualized for SiO_2/poly-Si contacts. [122–124]. Additionally, several publications show simulations and theoretical models to describe the current transport through the SiO_2 for poly-Si contacts [121, 134–137]. To form the poly-Si layer the contact needs to be annealed at high temperatures of 600 °C − 1050 °C [49, 55, 77]. The mechanism to form pinholes is described as a «balling-up» of the SiO_2 in order to reduce stress in the layer during the annealing process [124, 138]. The term «pinhole» is thereby used to describe the direct conduction through the SiO_2, which do not necessarily have to be geometric holes in the oxide. They can also be local inhomogeneities in thickness or stoichiometry, which may enable direct conduction. Up to now pinholes have only been shown for contacts using poly-Si and therefore high temperature annealing but not for unannealed contacts like the TPC. To investigate if pinholes already occur during formation of the SiO_2, thus might also appear for unannealed contacts, conductive atomic force microscopy (c-AFM) measurements are performed. With c-AFM it is possible to map the oxidized surface and measure local inhomogeneities in the conductivity. After oxidation the samples are directly transferred into the vacuum chamber of the c-AFM to prevent any additional oxidation in air.

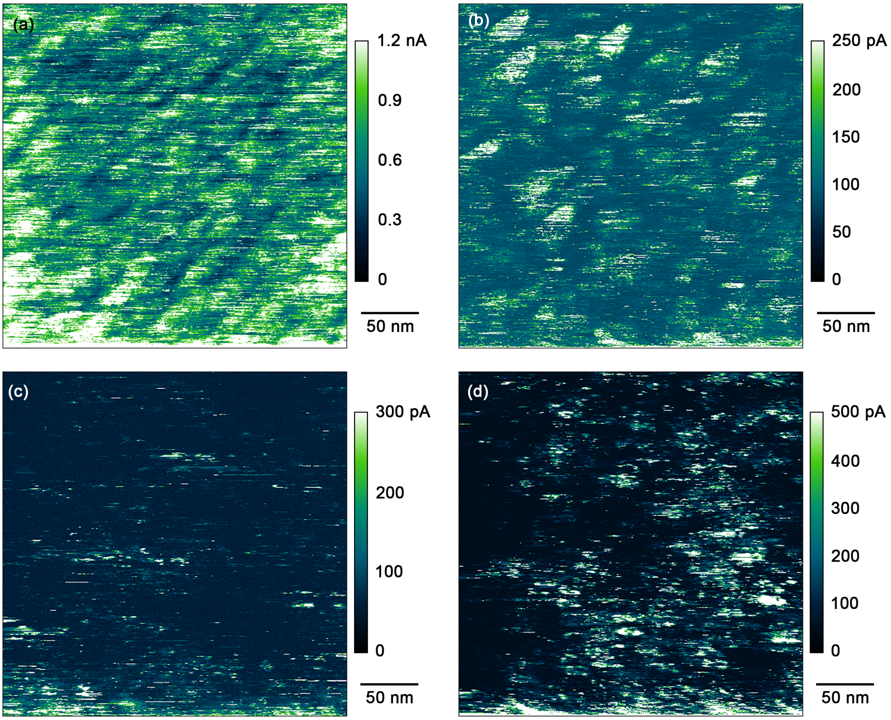

Figure 4.5.: *Conductive atomic force microscopy c-AFM measurements in vacuum of oxides prepared by piranha (a-b) and HNO_3 (c-d). Figures (a) and (c) are taken after desorption of water from the surface at 200 °C, Figure (b) and (d) are taken after annealing at 1000 °C. Figures (a) and (b) are measured using a tip potential of -2 V while Figure (c) is measured at -3 V and (d) at -4 V.*

The results of the c-AFM measurements on piranha and HNO_3 oxides are shown in Figure 4.5. The samples are first measured after a low temperature annealing in vacuum using a heater set to 200 °C to evaporate any residual humidity, which would disturb the measurements. To investigate the SiO_2 initial state the c-AFM measurements are preformed. Afterwards, the oxides are annealed at a heater set temperature of 1000 °C to simulate a standard annealing of poly-Si where pinholes were already found. The measurements on the piranha oxide are performed using -2 V c-AFM tip potential while for the HNO_3 -3 V and -4 V are necessary to measure any conductivity. The reason for that might be that the HNO_3 oxide is thicker than the piranha oxide. It can be seen that for the piranha oxide in the initial state (Figure 4.5 a) the conductivity is inhomogeneous but no pinhole like structures can be seen. Annealing at 1000 °C results in an overall decreased conductivity of the oxide with more pronounced conductive patches (Figure 4.5 b). For the HNO_3 oxide the conductivity in the initial state (Figure 4.5 c) is overall lower but more homogeneous compared to the piranha oxide. Only few conductive patches are measured. After annealing at 1000 °C the overall conductivity is decreased but more conductive patches can be found, which might be attributed to pinhole conduction.

To investigate the nature of these pinholes X-ray photoelectron spectroscopy (XPS) studies are performed to find stoichiometric inhomogeneities. Nevertheless due to very low signals for the sub-oxide peaks no conclusive results could be obtained. To further investigate the stoichiometry of the prepared oxides with photoemission spectroscopy (PES) and photoemission electron microscopy (PEEM) a high intensity synchrotron light source is necessary. During this thesis the application for beam time was granted but measurements could not be performed yet. Nevertheless, the c-AFM results lead to the conclusion that pinholes might only form after high temperature annealing and while in the initial state the conductivity through the oxide seems more homogeneous. This would lead to the conclusion that the transport process of the charge carriers is predominantly tunneling through the potential barrier of the SiO_2. However, pinhole formation in the oxide might also depend on the layer above the SiO_2 (e.g. poly-Si or µc-SiC:H(n)). This influence is not investigated in this work.

Selectivity To be able to put the obtained results from Figure 4.3 and Figure 4.4 into perspective to other tunnel oxide passivated contacts using poly-Si(n)/SiO_2 the passivation quality is plotted in terms of J_0 as a function of ρ_c in Figure 4.6. Since J_0 is a representation of the recombination current density, the value should be as low as possible. Iso-selectivity lines (gray dashed lines in Figure 4.6) are calculated using the method of Brendel and Peibst as described in Section 2.2 to compare the results of different contact materials. Contacts should be optimized by increasing the selectivity.

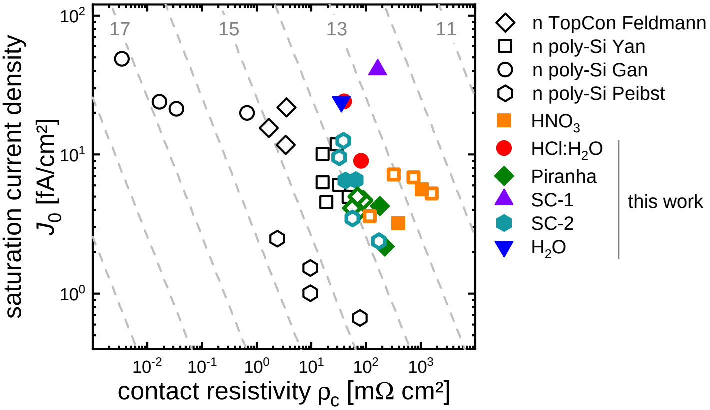

Figure 4.6.: *The saturation current density (J_0) as a function of the contact resistivity (ρ_c) for oxides grown using HNO_3 solution at room temperature, for 8% HCl at 80 °C, SC-1 at 60 °C, SC-2 at 60 °C, piranha at 60 °C, and native oxide. For open symbols the µc-SiC:H(n) is deposited using an MMS flow of 4 sccm resulting in higher conductivity of the layer. For closed symbols the µc-SiC:H(n) is deposited using an MMS flow of 6 sccm resulting in lower conductivity of the layer. The gray dashed lines are iso-selectivity lines calculated from Equation 2.25. The reported reference data (open black symbols) can be found in [53, 81, 121, 139–143]. The graph was originally published in [121]. Adapted with permission from [104]. Copyright 2018 American Chemical Society.*

It can be seen that the contact resistivity obtained for the TPC (colored symbols) is generally higher than for the poly-Si contacts (open symbols). Nevertheless, the saturation current density is lower compared to most poly-Si contacts. The lowest $\rho_c = 32\ \mathrm{m\Omega\,cm^2}$ is achieved for the SC-2 oxide while the lowest saturation current density is achieved for the piranha oxide with $J_0 = 2.2\ \mathrm{fA/cm^2}$. The results follow the trend of the results from Feldmann, Yan and Gan [139–141]. The saturation current density is decreasing with increasing contact resistivity. The reason for that might be the trade-off between passivation and conductivity of the contact materials as described by Brendel and Peibst [27]. The reason for the higher contact resistivity of the TPC contacts might be the absence of pinholes.

In comparison with contacts consisting of SiO_2/poly-Si contact, the TPC contact shows a higher contact resistivity and a higher passivation quality. Since the poly-Si layer has to be annealed at high temperature (850 – 1000 °C) pinholes have been found in the SiO_2. Therefore, it is possible that the contact resistivity is decreased due to a direct current path through the oxide where a lot of charge carriers avoid the tunneling process. These pinholes have not been demonstrated for unannealed contacts like the TPC yet. Nevertheless, these pinholes can also decrease the passivation quality of the contact since doping atoms, which are present in the a-Si:H precursor layers, can diffuse through the pinholes during the high temperature annealing. This local indiffusion can lead to locally enhanced recombination. That could be one explanation why the passivation quality of the TPC is higher.

The effect of the indiffusion of doping atoms during annealing can be prevented by ex-situ doping e.g. by ion implantation after annealing. Ion implanting is done for the contacts prepared by Peibst et al. and results in similar contact resistivities as for the in-situ doped poly-Si contacts but significantly decreases the saturation current density [121].

One reason why the contacts prepared by Peibst et al. show lower J_0 values compared to the TPC samples might be the HWCVD deposition, which could affect the passivation. The HWCVD deposition parameters are not optimized, which can influence the chemical passivation in addition to the oxide properties. The influence of the HWCVD deposition conditions on the passivation will be discussed in the following Section.

4.2. Influence of the filament temperature during HW-CVD for selected SiO_2

Passivation To further investigate the passivation quality of the SiO_2, selected oxides are tested using different filament temperatures during HWCVD deposition. The symmetric samples are prepared on double side textured Cz wafers. Pomaska showed that a changed filament temperature during HWCVD deposition of µc-SiC:H(n) influences the passivation quality of SiO_2 passivated samples prepared by HNO_3 [10]. This information is lacking for SiO_2 prepared by different oxidation solutions. Due to the obtained results in Section 4.1 the investigation is focused

Table 4.3.: *Best passivation results for the selected SiO_2 at the oxide specific filament temperature (T_f) with the implied open circuit voltage (iV_{oc}), effective minority carrier lifetime (τ_{eff}), and saturation current density (J_0) results obtained using photoconductance (PC) measurements.*

	spec. T_f [°C]	iV_oc [mV]	τ_eff [ms]	J_0 [fA/cm^2]
HNO_3	1740	715	2.2	12.8
piranha	1800	728	4.1	7.1
SC-2	1720	721	2.8	8.7

on the three best performing SiO_2 prepared by HNO_3, piranha, and SC-2 solution. The influence of the filament temperature (T_f) during HWCVD deposition on the iV_oc can be seen in Figure 4.7. The corresponding oxide thickness is marked in the brackets. It can be seen that the iV_oc is strongly dependent on the T_f. For all oxides the iV_oc is increasing with increasing T_f until a maximum in iV_oc is reached. The maximum achievable iV_oc depends on the oxidation method. The highest passivation qualities and the oxide specific filament temperatures can be found in Table 4.3. The highest passivation is achieved for oxidation in piranha solution with $iV_\mathrm{oc} = 728$ mV at $T_\mathrm{f} = 1800$ °C. The highest passivation for the SC-2 oxide is $iV_\mathrm{oc} = 721$ mV at $T_\mathrm{f} = 1720$ °C and for HNO_3 oxide $iV_\mathrm{oc} = 715$ mV at $T_\mathrm{f} = 1740$ °C. For HNO_3 an $iV_\mathrm{oc} = 704$ mV is additionally found for even higher $T_\mathrm{f} = 1895$ °C. It can be seen that the decrease of the iV_oc towards higher T_f depends on the oxidation method. The samples prepared by SC-2 oxide show the lowest resilience against high T_f and decrease to 600 mV at $T_\mathrm{f} = 1865$ °C.

The filament temperature during HWCVD deposition can effect the passivation quality by various reasons, which are discussed in more detail in Section 5.3. One mechanism, which might be important regarding the use of different SiO_2 oxidation solutions, can be the concentration of hydrogen radicals during HWCVD of the µc-SiC:H(n). As found by Umemoto et al. the radical density of hydrogen is increased exponentially by an increase of the filament temperature [145]. Therefore, a lot more radicals can damage the passivation of the c-Si/SiO_2 interface. Additionally, the deposition rate is found to be decreasing for increasing T_f, resulting in a longer time until the SiO_2 is covered by µc-SiC:H(n). Thus, the hydrogen radicals

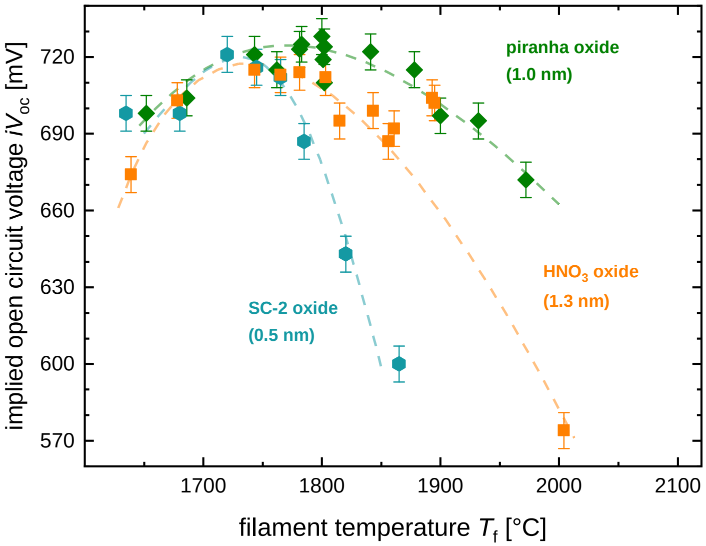

Figure 4.7.: *Implied open circuit voltage (iV_{oc}) as a function of the filament temperature (T_f) of the hot wires for SiO_2 prepared by selected oxidation solutions. HNO_3 at room temperature, SC-2 at 60 °C, and piranha at 60 °C. The oxide thicknesses are shown in brackets. Dashed lines are guides to the eye. Reprinted, with permission, from [144]. Copyright 2018 IEEE.*

have a longer time to impair the SiO_2 surface before it is protected by the growing µc-SiC:H(n). The oxide thickness of the SC-2 oxide might be too thin to protect the interface against deterioration. Nevertheless, a thickness of $d_{\mathrm{SiO2}} \leq 1$ nm seems to be sufficient to protect the c-Si surface. A thicker SiO_2 as for the HNO_3 oxide is not further improving the passivation quality. Therefore, the oxide thickness is not the only parameter influencing the passivation quality. Additionally, an influential parameter could be the atomic density of the SiO_2 (ρ_{SiO2}). An oxide with a higher density might be more stable against the hydrogen radicals as it is also stable against higher annealing temperatures. This would also explain why the SC-2 oxide is less stable against high T_f (see Table 4.2).

Contact Resistivity An increased T_f is not only decreasing the iV_oc. Previous work showed that the T_f also influences the electrical conductivity (σ) of the µc-SiC:H(n). Therefore, it was assumed that the T_f also influences the contact resistivity of the TPC [10]. TLM silver structures are evaporated and measured on the symmetric dst samples. In Figure 4.8 the contact resistivity (ρ_c) is plotted as a function of the filament temperature (T_f) calculated from TLM measurements. It can be seen that T_f as well as the oxidation method have an influence on the contact resistivity. For the thinnest SiO_2 (SC-2: $d_\mathrm{SiO2} = 0.5$ nm) the highest ρ_c is 375 mΩ cm^2 at $T_\mathrm{f} = 1785$ °C. For $T_\mathrm{f} < 1750$ °C ρ_c can not be evaluated due to non-linearities in the measured TLM data, which is likely due to the low conductivity of the µc-SiC:H(n) in this temperature regime. The lowest ρ_c is 62 mΩ cm^2 at $T_\mathrm{f} = 1865$ °C. For the thicker piranha oxidized samples ($d_\mathrm{SiO2} = 1$ nm) the lowest T_f which can be evaluated is 1840 °C with $\rho_\mathrm{c} = 62$ mΩ cm^2. Also the lowest ρ_c is calculated for samples oxidized using piranha solution at the highest $T_\mathrm{f} = 1970$ °C for these samples resulting in 18 mΩ cm^2. For the samples oxidized in HNO_3 ($d_\mathrm{SiO2} = 1.3$ nm) only the samples deposited at the highest $T_\mathrm{f} = 2005$ °C show a linear behavior in TLM measurements and result in $\rho_\mathrm{c} = 74$ mΩ cm^2.

In conclusion, both, the T_f during HWCVD deposition as well as the oxide thickness, have a significant influence on the contact resistivity. A trend can be seen that for thicker oxides higher conductive µc-SiC:H(n) is necessary to achieve reliable TLM results. For samples with the same oxide thickness the contact resistivity decreases exponentially with T_f probably due to a higher conductivity of the µc-SiC:H(n), which will be investigated in Section 5.1. T_f and thereby electrical conductivity of the µc-SiC:H(n) remains the main influence on ρ_c.

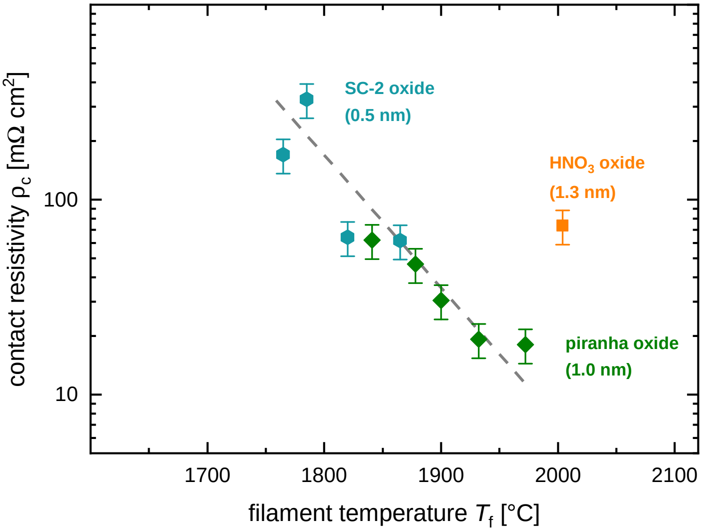

Figure 4.8.: *Contact resistivity (ρ_c) as a function of the filament temperature (T_f) of the hot wires for SiO_2 prepared by selected oxidation solutions. HNO_3 at room temperature, SC-2 at 60 °C, and piranha at 60 °C. The oxide thicknesses are shown in brackets. Dashed line is a guide to the eye. Reprinted, with permission, from [144]. Copyright 2018 IEEE.*

4.3. Summary

The focus of this Chapter was to find an optimized wet-chemically grown SiO_2, which provides a high passivation quality for the TPC and enables a low contact resistivity. Therefore, selected wet-chemical oxidation solutions as well as oxidation times were tested. It was found that a thin SiO_2 layer on c-Si alone is not sufficiently passivating to measure the passivation quality by photo-conductance (PC). Therefore, an additional µc-SiC:H(n) layer is needed. The data shows that longer oxidation time does not influence the passivation quality. Longer times in the oxidation solution seems to neither result in an increased roughness or D_{it}, which would decrease the iV_{oc}, nor in a higher quality SiO_2, which would improve the passivation quality.

In the second experiment the influence of the oxide thickness on the passivation quality as well as on the contact resistivity was investigated. It was shown that the highest passivation quality is achieved for an oxide thickness of 1 nm and oxidation in piranha solution with $iV_{\mathrm{oc}} = 714$ mV on dsp wafer. For thinner SiO_2 (SC-2) the passivation quality was lower leading to the conclusion that the oxide layer is not thick enough to protect the c-Si/SiO_2 interface against the harmful deposition conditions of the HWCVD. For higher oxide thicknesses (HNO_3) also lower passivation qualities were observed. The reason for that might be that the HNO_3 solution is increasing the surface roughness of the interface while oxidation in piranha solution is decreasing the surface roughness [116]. An increased surface roughness can then lead to an increased D_{it} and a higher recombination rate. Additionally, it was found that the SiO_2 prepared by SC-1 solution, even though it has an $d_{\mathrm{SiO2}} = 1$ nm, shows a significantly lower passivation quality compared to the piranha oxide. The reason for that might be the wrong polarity of the fixed charges, which is decreasing the field effect passivation.

It was also found that oxide thicknesses of $d_{\mathrm{SiO2}} \geq 1$ nm significantly increase the contact resistivity. The dominating transport mechanism seems to be quantum-mechanical tunneling. For thinner oxides the transport mechanism is not completely understood yet. One possible reason that the contact resistivity is not decreasing with the same slope as for the thicker oxides might be that the conductivity of the µc-SiC:H(n) is the limiting parameter rather than the tunneling process. The idea is supported by the indication of the correlation between low contact resistivities and high electrical conductivities of the µc-SiC:H(n).

The influence of the T_{f} on the passivation quality and the contact resistivity for selected oxidation solutions was discussed in the second Section of this Chapter. It was found that differently prepared oxides show a different resilience against higher T_{f}. The highest passivation quality was found for the combination of a piranha oxide and a µc-SiC:H(n) deposited at $T_{\mathrm{f}} = 1800$ °C with an $iV_{\mathrm{oc}} = 728$ mV on dst wafers. The other oxides show lower passivation qualities as well as faster decreases of passivation quality for increased T_{f}. The reason for this decrease in passivation quality might be the thickness of the oxide for oxides prepared by SC-2 as well as the lower ρ_{SiO2} and higher D_{it} for HNO_3 oxides. The lowest contact resistivity was found the be $\rho_{\mathrm{c}} = 18\ \mathrm{m\Omega\,cm^2}$.

5. Material and Contact Properties of μc-SiC:H(n)

In the following Chapter the material properties of μc-SiC:H(n) and the contact properties of the c-Si/SiO$_2$/μc-SiC:H(n) stack are investigated regarding the use as a transparent front side contact for c-Si solar cells. Contacts for the front side of c-Si solar cells have to fulfill three fundamental requirements:

(i) The contact needs to be conductive, since the photo-generated charge carriers have to flow through the contact into the metal electrodes.

(ii) The passivation quality of the interface between c-Si and contact needs to be excellent to reduce charge carrier recombination.

A high electrical conductivity of the μc-SiC:H(n) leads to a low contact resistivity (ρ_c) and a low series resistance (R_s) and thereby enables a high fill factor (FF) of the final solar cell. A high transparency of the contact enables a high short circuit current density (J_sc) while a high passivation quality enables a high open circuit voltage (V_oc). Details regarding the mechanisms of passivation can be found in the Fundamentals Chapter. This Chapter discusses the investigation of the electrical and the optical properties of the μc-SiC:H(n) as well as the contact properties of the TPC. At the end of this Chapter the obtained results are used to optimize the TPC by implementing a functional layer stack of μc-SiC:H(n).

5.1. Electrical properties

This Section focuses on the electrical properties of the μc-SiC:H(n) and its dependency on the filament temperature (T_f) during hot wire chemical vapor deposition (HWCVD). The aim of these experiments is to increase the electrical conductivity of the µc-SiC:H(n), since it has to conduct the charge carriers to the electrodes of the solar cell. It was shown in literature that the electrical conductivity (σ) of unintentionally doped µc-SiC:H(n) films [10,146,147] and intentionally doped films [129] is increased by increasing T_f. Intentionally n-type doping in SiC films can either be realized using molecular nitrogen (N_2), ammonia (NH_3), molecular oxygen (O_2) or by phosphine (PH_3) precursors as it was described in literature [10,148–151]. In this work nitrogen was used as a doping precursor gas. In Figure 5.1 (a) the electrical conductivity (σ) of the µc-SiC:H(n) films of this work is plotted as a function of T_f. It can be seen that the conductivity increases from 10^{-12} S/cm to 0.9 S/cm by increasing the T_f from 1630 °C to 2070 °C. The electrical conductivity increases mainly between $T_\mathrm{f} = 1750$ °C and 1900 °C by 10 orders of magnitude. This strong increase in conductivity can either originate from an increased charge carrier density (n) in the material, an increased μ, or both, since $\sigma = \mathrm{q}\, n\, \mu$. Nevertheless, due to the low conductivity for most of the films Hall measurements to extract n and μ did not give any conclusive results. According to Pomaska [10] the electrical conductivity of µc-SiC:H(n) can be increased by three parameters:

(i) by an increased oxygen concentration,

(ii) by an increased crystallite size (L_SiC),

(iii) by an increased nitrogen concentration (c_N).

The oxygen in the µc-SiC:H(n) is not intentionally added as a precursor during deposition. It can originate from the atmosphere in the deposition chamber and is likely to be adsorbed on the wafer surface, which is transferred into the chamber. The oxygen concentration in the µc-SiC:H(n) films are investigated by ToF-SIMS measurements and is found to be constant for all samples (see Figure 5.1 d). Hence, an increase in conductivity due to an increased oxygen content can be excluded.

To investigate the microstructure of the µc-SiC:H(n) XRD measurements have been performed. However, due to the low layer thickness (~30 nm) of the µc-SiC:H(n) the XRD signals have been too weak to obtain the reliable crystallite size L_SiC. In literature a correlation between intensity of the Si–C stretch mode in FTIR spectroscopy ($I_\text{Si-C}$) and crystallite size measured by XRD was found [10]. FTIR signals can be evaluated for thick and thin µc-SiC:H(n) layers. To con-

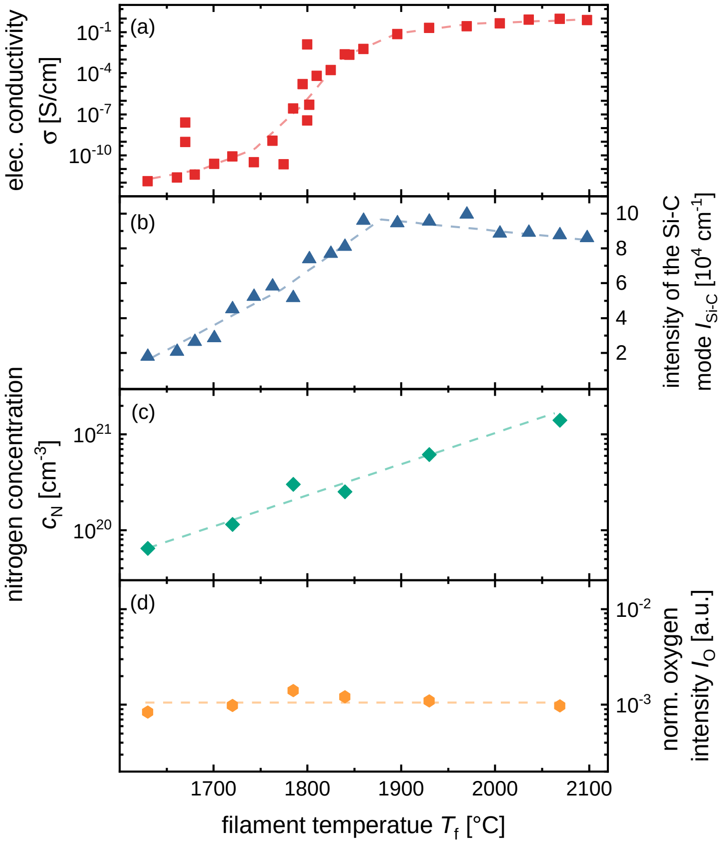

Figure 5.1.: *(a) The electrical conductivity (σ) measured on µc-SiC:H(n) on glass. (b) Intensity of the FTIR Si-C stretch mode at ν = 780 cm^{-1} as a measure of the relative crystallite site of µc-SiC:H(n). For FTIR measurements layers aere deposited on dsp c-Si. (c) The nitrogen concentration (c_N) and (d) normalized intensity of the oxygen signal (I_O) measured by ToF-SIMS in µc-SiC:H(n) on glass. Dashed lines are guides to the eye. Copyright 2019 IEEE. Adapted, with permission from [152].*

firm the correlation between $I_{\text{Si-C}}$ and average µc-SiC:H(n) grain size measured by XRD (L_{SiC}) both measurements have been applied to thicker (~100 nm) µc-SiC:H(n) layers. The results are plotted in Figure 5.2. It can be seen that the linear relation could be reproduced, which gives rise to the assumption that the microstructure of

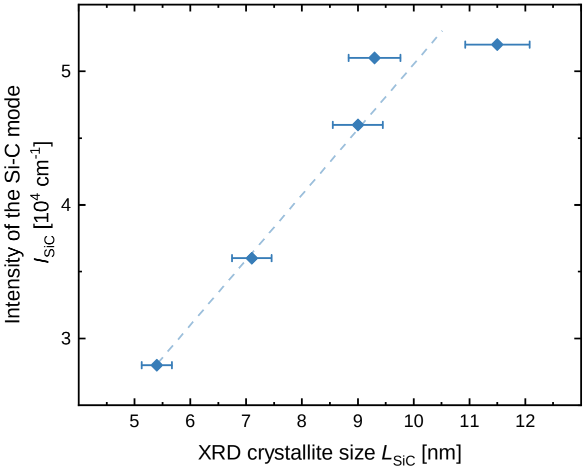

Figure 5.2.: *Absorption intensity of the Si–C stretch mode at ν = 780 cm^{-1} ($I_{\text{Si-C}}$) as a function of the XRD crystallite size (L_{SiC}). Measurements have been performed on ~100 nm thick µc-SiC:H(n) on dsp wafers. Dashed line is a guide to the eye. Copyright 2019 IEEE. Reprinted, with permission from [152].*

the µc-SiC:H(n) can be studied using FTIR spectroscopy. Nevertheless, for thinner layers the crystallite size is expected to be smaller compared to the thicker layers, since the material is still growing in the nucleation phase within the first nanometers.

The microstructure of the µc-SiC:H(n) was investigated by the absorption intensity of the stretch mode of the Si–C at a $\nu = 780$ cm^{-1} using FTIR spectroscopy. The results are plotted in Figure 5.1 (b). The $I_{\text{Si-C}}$ is increasing with increasing T_{f} up to $T_{\mathrm{f}} = 1860$ °C from 2×10^4 cm^{-1} to 1×10^5 cm^{-1}. For $T_{\mathrm{f}} > 1860$ °C $I_{\text{Si-C}}$ is slightly decreasing to 8×10^4 cm^{-1}. Under the assumption of a linear relationship between $I_{\text{Si-C}}$ and L_{SiC} these results shows that the crystallite size is increasing in the same filament temperature range (1620 °C – 1860 °C) as the electrical conductivity is increasing. For higher filament temperatures $T_{\mathrm{f}} > 1860$ °C both, $I_{\text{Si-C}}$ and σ reveal a plateau or a slight decrease. This indicates that the conductivity of the µc-SiC:H(n) is strongly correlated to the microstructure of the film. These results are in good agreement with the results obtained by Pomaska where also an increase in σ by several orders of magnitude could be observed for a higher microstructural order of µc-SiC:H(n) [10]. An increase in crystallite size was found to increase n

strongly and μ slightly for unintentionally doped µc-SiC:H(n) films [10]. The reason for that might be a lower density of depleted grain boundaries, which results in a decreased activation energy for the doping atoms. This decreased activation energy then results in an increase in free charge carriers. Nevertheless, it is unclear if the mechanism for intentionally doped µc-SiC:H(n) might be more complex.

A third possibility to increase the electrical conductivity of µc-SiC:H(n) is the doping by nitrogen. To investigate the nitrogen content of the µc-SiC:H(n) the concentration was measured by ToF-SIMS on the same samples as used for the σ measurements. The nitrogen concentration (c_N) as a function of the filament temperature is plotted in Figure 5.1 (c). The c_N is increasing by 1.5 orders of magnitude from $c_\mathrm{N} = 7 \times\ 10^{19}$ cm^{-3} to 1×10^{21} cm^{-3} for $T_\mathrm{f} = 1630$ °C to 2070 °C. This increase in nitrogen in the film can only account for a maximum increase of 1.5 orders of magnitude in σ. Thus, the increased nitrogen concentration alone cannot explain the increased electrical conductivity of µc-SiC:H(n). In literature it was found that an increased nitrogen concentration in the samples increases σ of the µc-SiC:H(n) due to an increase in both n and μ [10]. For very high nitrogen concentrations Pomaska proposed that the µc-SiC:H(n) might degenerates and the Fermi-level shifts into the conduction band [10]. This assumption is stressed by the calculations of Hong-Sheng et al. for nitrogen doping of crystalline 3C-SiC [153]. They also found that the Fermi-level is shifted into the conduction band for nitrogen doped SiC. However, it is unclear how much of the incorporated nitrogen is doping active.

The active donor doping concentration ($N_\mathrm{D}^\mathrm{act}$) can be measured using electrochemical capacitance-voltage profiling (eCV). Since a junction is necessary for eCV measurements, the results cannot be obtained on µc-SiC:H(n) layers on glass, which were used for conductivity measurements. To be able to measure $N_\mathrm{D}^\mathrm{act}$ the µc-SiC:H(n) layers are deposited on dst Cz-Si(n) wafers using the same deposition parameters as for layer used in Figure 5.1. To be able to compare the active doping concentration with the total concentration of nitrogen, c_N is measured again by ToF-SIMS measurements of the µc-SiC:H(n) deposited on wafer. The results for both series can be found in Figure 5.3.

The nitrogen concentration of the µc-SiC:H(n) on dst wafer and the active

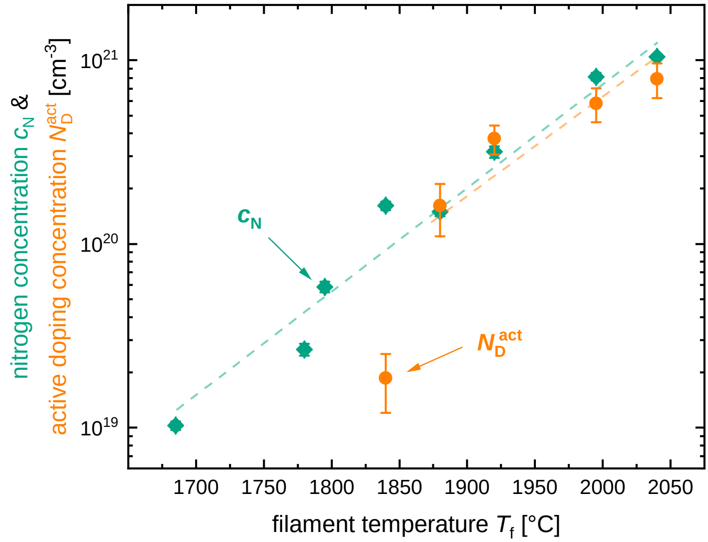

Figure 5.3.: *The nitrogen concentration (c_N) extracted from the ToF-SIMS measurement data shown in Figure 5.1 (green diamonds). The active donor doping concentration (N_D^{act}) measured using eCV is plotted as a function of T_f (yellow circles). From the nitrogen concentration and the active doping concentration the doping efficiency can be calculated. Dashed lines are guides to the eye.*

donor doping concentration are plotted as a function of the filament temperature. It can be seen that the total c_N is exponentially increasing by two orders of magnitude from 10^{19} cm^{-3} to 10^{21} cm^{-3} in the T_f interval from 1650 °C to 2050 °C. This increase is stronger as found for the c_N of µc-SiC:H(n) on glass. It is possible that the substrate material influence the incorporation of nitrogen into the µc-SiC:H(n). One reason for that might be that the microstructure of the µc-SiC:H(n) is different, since the growth conditions depend on the substrate material. Additionally, it can be seen that the active doping concentration for $T_f > 1840$ °C is almost equal to the total nitrogen concentration. This leads to the conclusion that the doping efficiency of the nitrogen is one for $T_f > 1840$ °C. For $T_f = 1840$ °C the active doping concentration is about one order of magnitude lower than the total nitrogen content. This result is an indication that the doping efficiency of nitrogen is decreased for lower filament temperatures. The reason for that might be the lower crystallite size as found in Figure 5.1 (b). For a lower crystallite size it is possible that less nitrogen is incorporated into the crystals and more nitrogen accumulates at the grain boundaries where it is not doping active. For $T_\mathrm{f} < 1840$ °C the electrical conductivity of the µc-SiC:H(n) is most likely too low to measure $N_\mathrm{D}^\mathrm{act}$ by eCV reliably.

It can be concluded that the filament temperature during HWCVD deposition of µc-SiC:H(n) has a strong influence on the electrical conductivity of the material. Since the oxygen content is constant for all samples, the main contribution to the n-type doping is most likely a result of nitrogen doping. Nevertheless, it is found that the increase in nitrogen in the film cannot account for the complete increase in conductivity. Therefore, another mechanism resulting in higher conductivity has to be present. One additional mechanism might be the increased crystallite size of the SiC. The crystallite size is found to increase with increased filament temperature, which might also lead to a higher doping efficiency and an increased free carrier density in the material. Nevertheless, the complete mechanism leading to an increase of 12 orders of magnitude in µc-SiC:H(n) conductivity over the complete T_f range is still not fully revealed. For the temperature range where eCV measurements were possible (1840 °C – 2040 °C) σ was increased by $\sim$3 orders of magnitude. This increase in conductivity might be explained by an increase of the nitrogen concentration (one order of magnitude) and the increase in crystallite size (one order of magnitude), which increases the free carrier concentration by 2 orders of magnitude. Due to the increase of crystallite size also the mobility of the material might be increased (one order of magnitude) as described by Pomaska [10]. To confirm these hypothesis further electrical characterization is needed e.g. by thermopower measurements.

5.2. Optical properties

For a high J_sc of the solar cell, the light facing contact has to be very transparent for the incident sunlight. Since the $\mathrm{SiO_2}$ is very thin and has a bandgap of 9.4 eV [154], the tunnel oxide is not limiting the transparency of the stack. Therefore, the transparency of the µc-SiC:H(n) is studied. From literature it is known that µc-SiC:H(n) can be applied as a window layer for thin film silicon solar cell [146, 147, 155–157]. Pomaska et al. investigated the optical properties of unintentionally and intentionally n-type doped thicker µc-SiC:H(n), which was several hundred nanometers thick [10, 158].

In this study several ten nanometer thick layer are characterized. To investigate the transparency of the µc-SiC:H(n) the optical absorption coefficient (α) is determined by PDS and T & R measurements for layers deposited at different T_{f}. Details regarding the measurement methods can be found in Section 3.3. The results of these measurements are shown in Figure 5.4 as a function of the photon energy (E_{Ph}). It can be seen that for lower filament temperatures and low photon energies $E_{\mathrm{Ph}} < 2$ eV the absorption coefficient is between 10^2 cm^{-1} and 10^3 cm^{-1}. For E_{Ph} between 2 – 3 eV α is increasing to $>10^4$ cm^{-1} depending on the filament temperature. It can be seen that the optical bandgap (E_{04}), which is equal to E_{Ph} when $\alpha = 10^4$ cm^{-1} (gray dashed line), is increasing with increased filament temperature. Nevertheless, it can also be seen that in the low E_{Ph} range between 0.5 eV and 2 eV the absorption coefficient is strongly increased for the highest T_{f} of 1860 °C and 1900 °C.

This absorption is called «sub-bandgap» absorption, since it occurs for light with an energy smaller then the optical bandgap. The sub-bandgap absorption can be evaluated by the sub-bandgap absorption coefficient (α_{1eV}), which is extracted at $\alpha(1\,\mathrm{eV})$. The influence of T_{f} on E_{04} and α_{1eV} can be seen in Figure 5.5 (a) and (b), respectively. The optical bandgap is increased from 2.3 eV to 2.9 eV in the filament temperature range of 1660 °C to 1900 °C. This result indicates that the µc-SiC:H(n) is getting more transparent with increased T_{f}. Nevertheless, the sub-bandgap absorption coefficient increases exponentially by 1.5 orders of magnitude from $\alpha_{\mathrm{1eV}} = 2\times10^1$ to 4×10^3 cm^{-1} in the same filament temperature range indicating that the material absorbs more light for photon energies below the optical bandgap. To be able to judge the influences of the E_{04} and the α_{1eV} on the final J_{sc} of the device the absorption loss in J_{sc} is calculated by multiplying the absorptance with the solar spectrum under 1.5 time the air mass of the atmosphere (AM1.5G(λ)) and integrating it over the wavelength up to the bandgap of c-Si at 1060 nm. The parasitic absorption current density loss ($J_{\mathrm{SiC}}^{\mathrm{abs}}$) is calculated for the first light path through the solar cell neglecting multiple reflections by

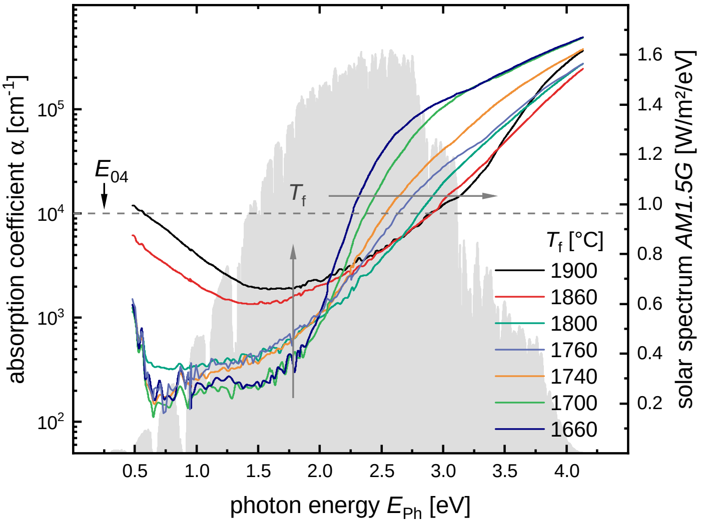

Figure 5.4.: *The optical absorption coefficient* (α) *(left y-axis) and solar spectrum for AM 1.5G (right y-axis) as a function of the photon energy* (E_{Ph})*. The optical absorption coefficient is calculated from PDS and transmission and reflection (T & R) measurements for µc-SiC:H(n) deposited on glass. The µc-SiC:H(n) is deposited using selected* T_f*. The dashed line marks the absorption coefficient of* $\alpha = 10^4$ cm^{-1} *where the optical bandgap* (E_{04}) *is extracted. The gray area shows the solar spectrum in terms of W/(m^2 eV) to illustrate how much energy is contained in the sunlight at distinct photon energies. The integrated energy results in 1003 W/m^2. Copyright 2018 IEEE. Adapted, with permission from [104].*

$$J_{\mathrm{SiC}}^{\mathrm{abs}} = \int_{300\ \mathrm{nm}}^{1060\ \mathrm{nm}} \left(1 - e^{-\alpha(\lambda) d_{\mathrm{SiC}}}\right) \mathrm{AM1.5G}(\lambda) \mathrm{d}\lambda \tag{5.1}$$

with the wavelength dependent absorption coefficient $\alpha(\lambda)$, the µc-SiC:H(n) layer thickness (d_{SiC}).

The results for µc-SiC:H(n) thicknesses of 20 nm, 40 nm, and 60 nm are plotted in Figure 5.5 (c). It can be seen that the $J_{\mathrm{SiC}}^{\mathrm{abs}}$ is decreasing with increasing T_f until reaching a minimum at 1800°C and then slightly increasing again. The reason for the decrease of parasitic absorption in the lower filament temperature range is the increase of the E_{04}. The slight increase of $J_{\mathrm{SiC}}^{\mathrm{abs}}$ for $T_f > 1800$ °C can be explained by the increased sub-bandgap absorption. Since the optical bandgap is only increasing

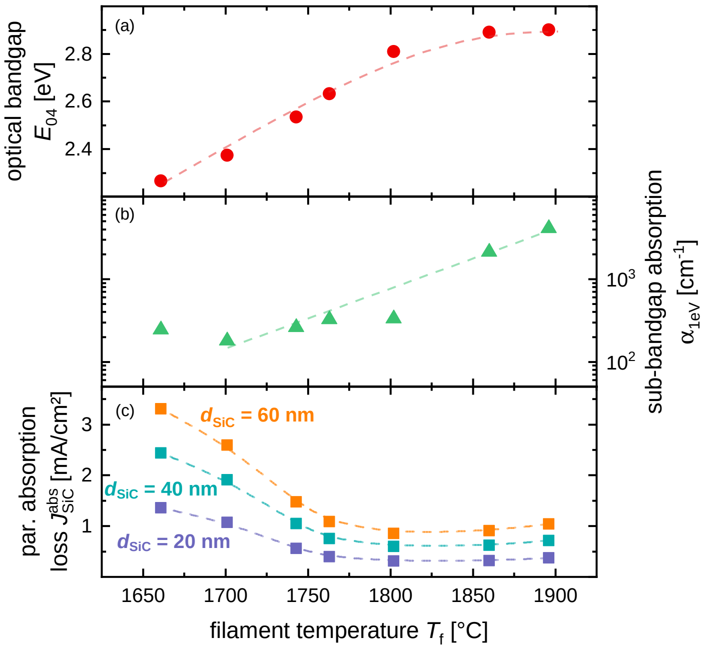

Figure 5.5.: *(a) The optical bandgap (E_{04}) as a function of T_f. E_{04} is extracted at the dashed line in Figure 5.4. (b) The sub-bandgap absorption at the photon energy of* 1.0 eV *(α_{1eV}), and (c) the parasitic absorption current density loss (J_{SiC}^{abs}) as a function of T_f. J_{SiC}^{abs} is calculated according to Equation 5.1 for three selected µc-SiC:H(n) thicknesses (60 nm, 40 nm, and 20 nm). Dashed lines are guides to the eye. Copyright 2018 IEEE. Adapted, with permission from [104].*

slightly in this T_f region, the optical loss due to sub-bandgap absorption cannot be compensated. Nevertheless, it can be concluded that the sub-bandgap absorption has a smaller impact on the parasitic absorption than the optical bandgap. The lowest parasitic absorption for film thickness of µc-SiC:H(n) (d_{SiC}) = 20 nm is found to be $J_{SiC}^{abs} = 0.31$ mA/cm^2 for $T_f = 1800$ °C.

To be able to explain the origin of the increased E_{04} and increased α_{1eV} with increased T_f these parameters are plotted as a function of the electrical conductivity and the Si–C stretch mode from FTIR in Figure 5.6, which is a measure for the crystallite size of the µc-SiC:H(n). It can be seen that the optical bandgap

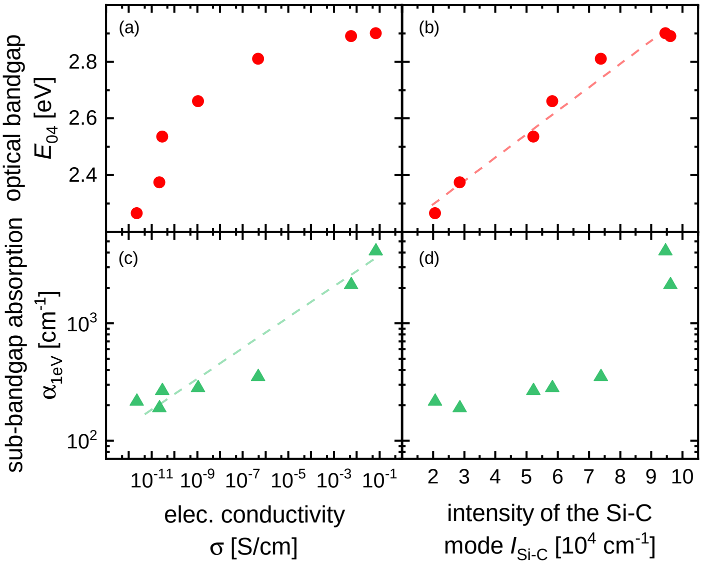

Figure 5.6.: *Correlations of optical bandgap (E_{04}) with the electrical conductivity (σ) in (a) and with the intensity of the Si–C stretch mode in FTIR spectroscopy ($I_{\text{Si-C}}$) in (b) as well as the correlation of the sub-bandgap absorption at the photon energy of* 1.0 eV *(α_{1eV}) with σ in (c) and with $I_{\text{Si-C}}$ in (d). Dashed lines are guides to the eye.*

shows a strong correlation with the intensity of the Si–C stretch mode. This leads to the conclusion that the optical bandgap is increased by an increased crystallite size of the µc-SiC:H(n). Fitting the data linearly results in the Equation $E_{04} = 0.084\, I_{\text{Si-C}} + 2.126$. The sub-bandgap absorption shows a correlation to the electrical conductivity but not to the Si–C stretch mode. This leads to the conclusion that the sub-bandgap absorption mainly results from the free carrier absorption of the µc-SiC:H(n). This result is consistent with the finding of an increased active doping concentration for increased T_f, which results in an increase of the free charge carrier density.

It can be concluded that the transparency of the µc-SiC:H(n) mainly depends on the optical bandgap and the sub-bandgap absorption coefficient. The optical bandgap increases with increased T_f, which might be due to an increased crystallite size of the µc-SiC:H(n). Nevertheless, also the sub-bandgap absorption is increasing, which most likely is due to the increased free carrier by an increased active doping concentration for increased T_f. To keep the parasitic absorption in the µc-SiC:H(n) as low as possible the lowest possible layer thickness which is still passivating the contact should be used. The lowest parasitic absorption is found for $T_\mathrm{f} = 1800$ °C.

5.3. Passivation and electrical contact properties of TPC

5.3.1. Single layer µc-SiC:H(*n*)

After discussing the electrical conductivity and the optical transparency of the µc-SiC:H(n), the passivation of the c-Si surface is the third key requirement for an advanced contact. However, the passivation is not only influenced by the µc-SiC:H(n) but is a property of the whole stack, which consists of the SiO_2 and the µc-SiC:H(n). As already discussed in the Fundamentals Chapter the dominating recombination mechanism in silicon solar cells, which uses high quality wafers, is usually the recombination at the surfaces of the c-Si. To reduce the recombination at the surface additional layers on top of the c-Si are necessary. These layers reduce the number of open silicon bonds (dangling bonds) at the interface, which acts as trap states for electrons and holes. In this work the silicon surface is passivated with a thin silicon oxide and a µc-SiC:H(n) layer. Details regarding the passivation mechanism can be found in the Fundamentals Section 2.3.

In this Section the influence of the filament temperature during HWCVD on the passivation quality is investigated. As already found in Chapter 4 high filament temperatures strongly decrease the passivation quality of the TPC. compared to the experiments in Figure 4.7 the cleaning and oxidation procedure is kept the same and all wafers are oxidized in piranha solution for 10 min. A new generation of dst Cz wafers is used, which provides higher quality c-Si due to a narrower specified doping density and less impurities. This allows for higher passivation qualities compared to the wafer used before in the experiments in Figure 4.7.

To investigate the mechanisms of c-Si surface passivation, µc-SiC:H(n) has been deposited on textured and polished c-Si. Symmetrically passivated samples have been prepared on dst wafer to measure the passivation quality by photo-

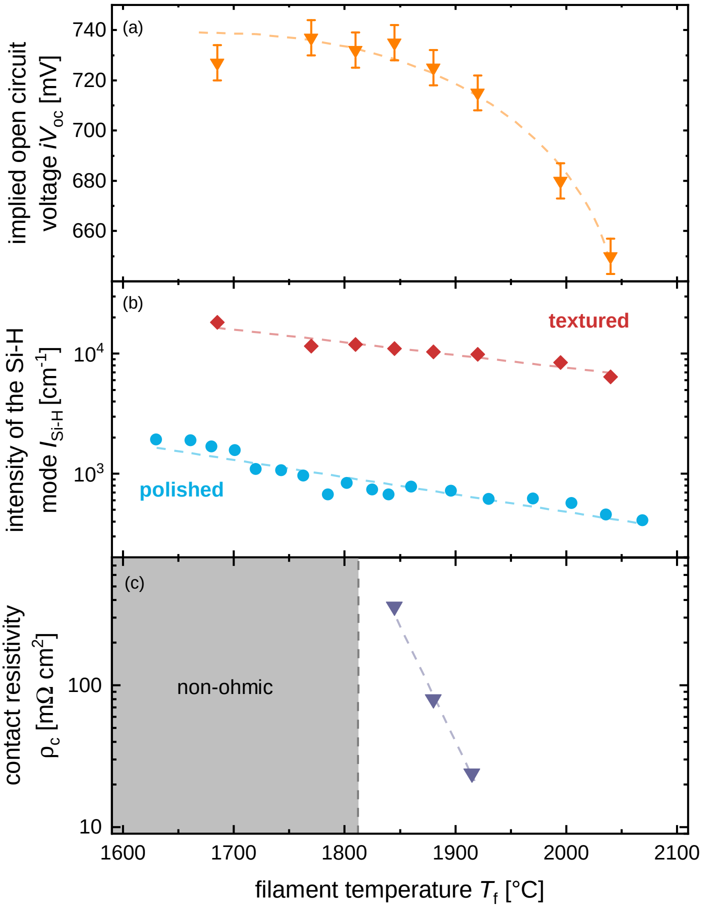

Figure 5.7.: *(a) The implied open circuit voltage (iV_{oc}) as a function of T_f. The iV_{oc} shows the same trend as in Figure 4.7. Nevertheless due to higher quality wafers the lifetime and iV_{oc} of the samples is improved. The SiO_2 is produced in piranha solution. (b) The intensity of the Si–H mode in FTIR spectroscopy ($I_{Si\text{-}H}$) of µc-SiC:H(n) on polished wafers (light blue circles) and $I_{Si\text{-}H}$ of µc-SiC:H(n) on textured wafers (red diamonds). (c) The contact resistivity (ρ_c) of the layer stack c-Si/SiO_2/µc-SiC:H(n)/ITO/Ag measured using the transfer length method (TLM). Dashed lines are guides to the eye.*

conductance measurements. For FTIR measurements of the hydrogen content, µc-SiC:H(n) is deposited only on one side of the dsp wafers. The passivation quality is measured in terms of iV_{oc} and J_0. The results of the iV_{oc} as a function of the T_{f} for symmetrically passivated samples are shown in Figure 5.7 (a). It can be seen that the same trend is evident as observed before in Figure 4.7 for samples oxidized in selected oxidation solutions. The passivation quality is reduced for higher filament temperatures. The highest passivation is found for the sample fabricated at $T_{\mathrm{f}} = 1775$ °C, where $iV_{\mathrm{oc}} = 737$ mV and $J_0 = 5$ fA/cm^2 have been measured. For $T_{\mathrm{f}} > 1950$ °C the iV_{oc} decreases below 700 mV. This decrease in passivation quality can either be happening due to a lower chemical passivation, a less selective contact, or both. Nevertheless, it was found before in Section 5.1 that the electrical conductivity and thereby the n-type character of the µc-SiC:H(n) is increasing with increased T_{f}. This increase in σ gives rise to a higher selectivity due to a higher field effect rather than a lower, which therefore, cannot explain a decrease in the passivation quality. Thus, a lower chemical passivation is more likely the reason for the reduced passivation quality for increased T_{f}.

A decrease in chemical passivation can have several reasons. One reason might be that the substrate temperature increases due to a stronger radiation of the hot wires. A higher substrate temperatures could lead to a diffusion or a desorption of the hydrogen at the SiO_2/c-Si interface [159–161]. This hydrogen loss then increases the number of silicon dangling bonds since Si–H bonds are broken. Diffusion of hydrogen from the interface requires a sub-stoichiometric SiO_2, since the hydrogen needs an additional open silicon bond in the SiO_2 where it can diffuse to. Because the SiO_2 is grown wet-chemically, a perfect stoichiometry is unlikely as found by Moldovan et al. [67, 81]. In contrast to diffusion, hydrogen atoms could also desorb from the interface in pairs and form molecular hydrogen. This hydrogen can then effuse through the SiO_2 and possibly leave the sample. The probability of the effusion of hydrogen strongly depends on the structure and thickness of the layers following the SiO_2 and might therefore change during deposition. Nevertheless, from amorphous silicon it is know that the diffusion of hydrogen happens at a diffusion energy of 1.53 eV while the desorption energy is 1.95 eV [162–164], which shows that diffusion is energetically more favorable. Both processes might happen simultaneously.

A decreased passivation due to an increased substrate temperature is likely not the only mechanism, since a lower passivation was also found for experiments where the substrate temperature was constant (e.g. changed F_{MMS}). Since Pomaska et al. found that a decreased F_{MMS} leads to an increased crystallite size, the microstructure of the µc-SiC:H(n) could also have influenced the passivation quality [158]. An additional mechanism, which might lead to a decrease in chemical passivation, is that the c-Si/SiO_2 interface is damaged due to the hydrogen radicals, which are present during HWCVD process. Etching of hydrogen was already reported for c-Si surfaces [165–167] as well as for a-Si:H layers [127,168,169]. The molecular hydrogen is used as a precursor to dilute the MMS precursor. H_2 decomposes at the hot wire filaments into atomic hydrogen i.e. hydrogen radicals. Umemoto et al. found that the hydrogen radical density is increased by several orders of magnitude in the given T_{f} range [145]. In the beginning of HWCVD deposition the atomic hydrogen can directly impair the thin SiO_2. The hydrogen radicals can either break a Si–O or a Si–H bond at the interface to the c-Si, which both would result in an additional recombination site at the interface due to an open silicon bond. Since the bond dissociation energy of Si–O (799.6 kJ/mol or 8.3 eV [170]) is about 2.7 times the bond dissociation energy of Si–H (293.3 kJ/mol or 3.1 eV [170]), it is more likely that hydrogen radicals break a Si–H bond. A third effect influencing the passivation quality might be the hydrogen reservoir of µc-SiC:H(n). This hydrogen might diffuse to the c-Si/SiO_2 interface an re-passivate the dangling bonds.

To investigate the influence of the filament temperature on the Si–H bonds FTIR measurements have been performed on textured and polished samples. From the FTIR intensity spectrum the absorption coefficient is calculated and evaluated for the peak intensity at $\nu = 2100\ \mathrm{cm}^{-1}$, which can be attributed to a stretching mode of the Si–H. The results are plotted in Figure 5.7 (b) for «polished» samples with single side µc-SiC:H(n), which originate from the same series as for Figure 5.1 and for «textured», symmetric µc-SiC:H(n) samples, which is the same series as in Figure 5.7 (a). It can be seen that the intensity of the Si–H mode $I_{\mathrm{Si\text{-}H}}$ is decreasing with increasing T_{f} for polished and textured samples. This leads to the conclusion that the amount of Si–H bonds is reduced. The most likely reason for this reduction of Si–H bonds is that the crystallite size of the µc-SiC:H(n) is increasing and therefore, the density of grain boundaries is decreased for increased T_{f}. Since

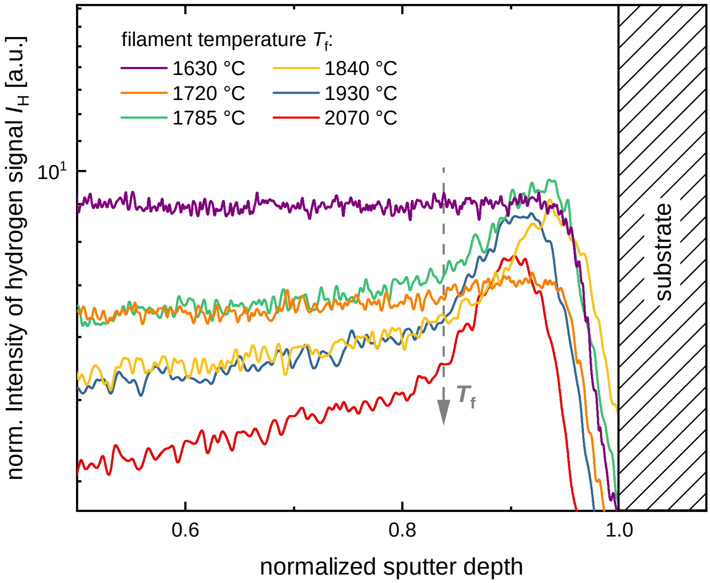

Figure 5.8.: *The intensity of the hydrogen signal in ToF-SIMS measurements (I_H) normalized by the signal of the ^{30}Si as a function of the sputter depth normalized to the film thickness on glass. The thickness is normalized to the sharp increase in oxygen signal as a measure for the glass substrate. The results show that with increasing T_f the hydrogen signal decreases as it is also found for FTIR measurements (see Figure 5.7 b). The layer thickness is in the range of 30 nm – 100 nm. The dashed arrow is a guide to the eye.*

the hydrogen is likely to be bonded to the silicon at the grain boundaries of the µc-SiC:H(n), less hydrogen is incorporated in the film when the density of grain boundaries decreases due to an increase in grain size.

To investigate the hydrogen content in the µc-SiC:H(n) layer also ToF-SIMS measurements have been performed. The results of these measurements can be found in Figure 5.8 as a function of the normalized sputter depth. The intensity of the hydrogen signal is normalized by the signal for ^{30}Si. It can be seen that the highest hydrogen signal is measured for the sample deposited at the lowest $T_f = 1630$ °C and the lowest hydrogen signal for the highest $T_f = 2070$ °C. These results are in good agreement with the results found in Figure 5.7 (b). These findings are stressing the assumption that less hydrogen is incorporated when the material is getting more crystalline with increasing T_f. This leads to the conclusion that more hydrogen is incorporated in the µc-SiC:H(n) when the microstructure is more amorphous. Additionally, it can be seen that the hydrogen signal increased towards the glass substrate for the four samples with the highest T_f. The reason for that is probably also the microstructure of the µc-SiC:H(n). It is known from literature that the growth of µc-SiC:H(n) on a foreign substrate id more amorphous in the first few nanometers (nucleation phase) before larger crystals are growing [171, 172]. Therefore, the first nanometers of more amorphous SiC can contain a higher concentration of hydrogen. Another possibility for the hydrogen peak towards the glass interface would be a ToF-SIMS measurement artifact called the «knock-on» effect during the depth profiling of the measurement. To measure a depth profile in ToF-SIMS a crater is sputtered by a primary ion beam. While sputtering it can happen that the primary ion beam drives-in elements deeper into the remaining material rather then releasing the ions. The knock-on effect results then in an artificially increased concentration close to the interface of the layer. This knock-on effect would be evident for all measured samples. Nevertheless, the peak is not observed for the samples deposited at lower T_f leading to the conclusion that the hydrogen peak is no measurement artifact. This lack of increased I_H signal towards the substrate for the samples deposited at $T_\mathrm{f} = 1630$ °C and 1720 °C might be an indication that the microstructure of the SiC is completely amorphous throughout the layer. Therefore, no difference in the I_H signal can be seen. Only for $T_\mathrm{f} > 1720$ °C a distinct difference in microstructure between nucleation and bulk phase occurs.

These results lead to the conclusion that hydrogen content in the µc-SiC:H(n) strongly depends on the T_f during HWCVD deposition. Therefore, the results of the hydrogen content measured by FTIR (Figure 5.7 (b)) cannot be directly related to the breaking of Si–H bonds at the SiO_2/c-Si interface but rather to the hydrogen content in the µc-SiC:H(n) layer. Nevertheless, a high hydrogen concentration especially close to the SiO_2/c-Si might lead to an improved passivation at the interface. If the increased hydrogen radical density due to an increased T_f leads to a deterioration of the interface cannot be finally concluded. Evidence of a damaged SiO_2 interface could not be found in transmission electron microscopy (TEM) micrographs. Nevertheless, it cannot be excluded that the decreased passivation quality for increased T_f

is a combination of impaired SiO_2/c-Si interface and less hydrogen at the interface to re-passivate the open dangling bonds. The entire mechanism, which gives rise to such high passivation qualities, is still not fully understood. Nevertheless, it should be noted that no post deposition treatments e.g. annealing or hydrogenation, which are necessary for e.g. SiO_2/poly-Si contacts, have be applied to the TPC contacts.

After studying the electrical conductivity of the µc-SiC:H(n) in Section 5.1 the contact resistivity (ρ_c) of the entire front layer stack (c-Si/SiO_2/µc-SiC:H(n)/ITO/Ag) is of major importance, since it contributes to the series resistance of the final device. The contact resistivity is comprised of the vertical resistivities of SiO_2, µc-SiC:H(n), and ITO as well as the resistivities at the interface between the layers (see Figure 3.2). The conductivity of the µc-SiC:H(n) is orders of magnitude lower than the conductivity of the wafer, which suppresses lateral current flow in the µc-SiC:H(n). This contact resistivity can be measured by the transfer length method (TLM). Since it was found earlier that the electrical conductivity can be tuned within 12 order of magnitude by changing T_f, it is assumed that the conductivity of the µc-SiC:H(n) also influences the contact resistivity. To investigate the influence of the electrical conductivity of µc-SiC:H(n) on the contact resistivity for a complete solar cell stack, structured ITO and silver (Ag) pads are deposited on the µc-SiC:H(n) samples. The results of the contact resistivity as a function of the filament temperature for the µc-SiC:H(n) deposition can be seen in Figure 5.7 (c). The contact resistivity could only be evaluated for samples deposited at $T_f > 1820$ °C, since for lower filament temperatures the results showed a non-ohmic behavior. With increasing the filament temperature during µc-SiC:H(n) deposition from $T_f > 1848$ °C to 1915 °C the contact resistivity is dropping exponentially from 360 $m\Omega\,cm^2$ to 24 $m\Omega\,cm^2$. The reason for that is most likely the electrical conductivity of the µc-SiC:H(n), which is improving from $\sigma = 10^{-3}$ S/cm to 10^{-1} S/cm. For $T_f = 1810$ °C the conductivity of the µc-SiC:H(n) is 10^{-6} S/cm, which is most likely the reason why the contact resistivity, could not be evaluated. This result leads to the conclusion that the electrical conductivity of µc-SiC:H(n) is a main contribution to the contact resistivity. The influence of the contact resistivity on the series resistance and the fill factor of the final solar cell will be discussed in Section 6.2. It can be concluded that for very high iV_{oc} no sufficiently low ρ_c is achieved. For lower contact resistivities at higher T_f the passivation quality of the TPC starts to deteriorate. Therefore, an optimal trade-off between high passivation quality and low contact resistivity has to be found for a solar cell with single layer µc-SiC:H(n) as incestigated in Section 6.2.

5.3.2. Double layer µc-SiC:H(*n*)

In this Chapter it was shown that the filament temperature of the hot-wire filaments during HWCVD deposition has a strong influence on the electrical, optical, and passivation properties of the µc-SiC:H(n). While the electrical conductivity and the optical transparency of µc-SiC:H(n) are increased, the passivation quality of the TPC is decreased for an increasing filament temperature. Therefore, the optimization of the contact for solar cells is a trade-off between high passivation quality and high conductivity. To overcome this trade-off a double layer stack consisting of a «passivation SiC layer» on top of the SiO_2 followed by a «conductive SiC layer» is developed. The idea of this double layer stack is to first deposit a thin passivation layer at a lower filament temperature $T_\mathrm{f}^\mathrm{pass}$. This layer provides a more amorphous material, which has a high hydrogen content and is deposited with less hydrogen radicals in the gas phase, which might deteriorate the SiO_2/c-Si interface less. Since the µc-SiC:H(n) grown under these conditions has a low electrical conductivity, the layer should be as thin as possible while maintaining a high passivation quality. The conductive layer is afterwards deposited on top of the passivation layer at elevated filament temperature $T_\mathrm{f}^\mathrm{cond}$. The conductive layer is necessary, since it was found before that the thin passivation layer alone does not provide a sufficient surface passivation. The conductive layer then provides additional passivation and a higher electrical conductivity, which might improve the contact resistivity to the TCO.

To investigate the influence of the double layer stack, the passivation layer is deposited at filament temperature which gave the highest iV_oc for single layers $T_\mathrm{f} = 1775$ °C with a thickness of $d_\mathrm{SiC}^\mathrm{pass} = 9$ nm. After depositing the passivation layer, the filament current is ramped up, which increased the T_f for the desired filament temperature to deposit the conductive layer. Increasing the filament temperature can be done without interrupting the depositing process, thus, it does not add an additional process step to the fabrication. The thickness of the passivation layer is varied between $d_\mathrm{SiC}^\mathrm{cond} = 25$ nm – 30 nm. The layer thicknesses are calculated from

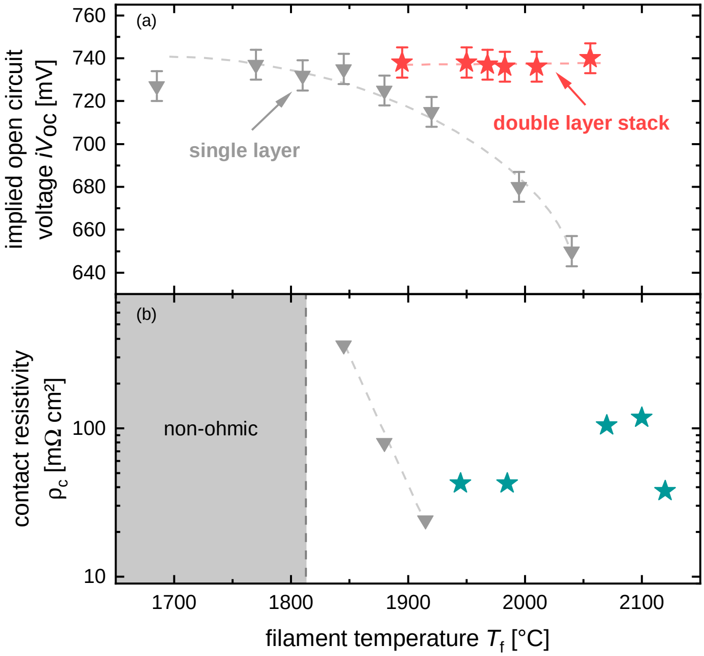

Figure 5.9.: *(a) Implied open circuit voltage (iV_{oc}) and (b) contact resistivity (ρ_c) as a function of T_f for symmetric TPC samples using a single layer (triangles) and a double layer stack (stars). For double layer stacks the filament temperature of the «passivation» layer is fixed to $T_f^{pass} = 1775\ ^\circ C$ and the filament temperature of the conductive layer (T_f^{cond}) is changed according to the horizontal axis. Dashed lines are guides to the eye. This figure was originally published in [9] and colors were adapted (CC BY 4.0).*

deposition rates measured on polished c-Si samples. The influence of T_f^{cond} on the passivation and the contact resistivity is depicted in Figure 5.9. It should be noted that the filament temperature of the conductive layer is varied and displayed on the horizontal axis.

It can be seen that the double layer stack (red stars) effectively prevents the sample from deterioration during the deposition process, which leads to a constant and high mean iV_{oc} of 738 mV even for $T_f^{cond} > 2000$ °C. The passivation of the single layer passivation (gray triangles) drops below 680 mV for $T_f > 2000$ °C. This reduction of iV_{oc} for increased T_{f} is not observed for the samples passivated using the double layer stack. This result leads to the conclusion that the passivation layer mainly determines the passivation quality of the entire stack. The best passivation quality is achieved for the conductive layer deposited at the highest filament temperature $T_{\mathrm{f}} = 2060$ °C. The respective iV_{oc} is 740 mV while the J_0 is 2 fA/cm^2.

In Figure 5.9 (b) the contact resistivity (ρ_{c}) is plotted as a function of the filament temperature of the conductive layer of the double layer stack. To measure the contact resistivity of the complete stack by TLM, structured ITO and Ag are deposited on the µc-SiC:H(n). It can be seen that a low contact resistivity of $\rho_{\mathrm{c}} = 38\ \mathrm{m\Omega\,cm^2}$ can be achieved while maintaining a high passivation quality. The contact resistivity of the double layer stack is slightly higher than the lowest contact resistivity, which was measured for single layer stacks (24 mΩ cm^2). The reason for that might be the influence of the 9 nm thin passivation layer, which increases the contact resistivity due to its low electrical conductivity of $\sigma \approx 10^{-8}$ S/cm.

The improved passivation quality of the double layer stack can have again various reasons. As explained before, one reason for the degradation of the passivation quality might be the loss of hydrogen at the interface due to an increased substrate temperature by stronger radiation of the hot-wire filaments. By adding a passivation layer, which contains more hydrogen than the layer deposited at higher T_{f}, the diffusion and desorption processes might be compensated when the substrate temperature increases during the conductive layer deposition. Since desorption and diffusion of hydrogen is a balance reaction with re-passivation of silicon dangling bonds, decreasing the hydrogen effusion and increasing the hydrogen reservoir at the interface would shift the balance reaction towards the re-passivation, which gives rise to higher passivation qualities.

Another reason for the improved chemical passivation might be that the thin passivation layer on top of the SiO_2 protects the c-Si/SiO_2 interface against the high hydrogen radical density during high $T_{\mathrm{f}}^{\mathrm{cond}}$ depositions for the conductive layer. Therefore, less silicon bonds are broken at the interface, which results in a lower concentration of silicon dangling bonds and thereby to less recombination sites.

Additionally, the increased conductivity of the second µc-SiC:H(n) layer results in a stronger field effect passivation. Therefore, the opposing field for the minority carriers is increased, which makes recombination less probable. The complete passivation mechanism for both single layers and double layer stack is still not fully understood. Nevertheless, it is likely that both the chemical passivation of the open silicon bonds as well as the field effect mechanism are influencing the overall passivation quality of silicon surface. At this stage device simulation with e.g. Sentaurus TCAD which are beyond the scope of this work could provide deeper insight into the relevant processes.

From the results of the passivation quality and the contact resistivity the selectivity of a contact can be calculated by the method proposed by Brendel and Peibst [27]. The selectivity is a measure of the ability of a contact to conduct majority carriers and block minority carriers. Therefore, an n-type contact works like a membrane, which allows electrons to pass and blocks holes. Using the concept of selectivity, different types of contacts can be compared with each other and possible limiting effects regarding the efficiency of a cell can be revealed. Further details regarding the calculation of the logarithm of selectivity (S_{10}) can be found in the Fundamentals Section 2.2.

For the single layer stack contacts at T_f = 1848 °C and 1915 °C a selectivity of S_{10} of 13.2 and 14.2 are calculated by Equation 2.25, respectively. For the double layer stack assuming the lowest J_0 and ρ_c a selectivity of $S_{10} = 14.5$ is achieved. To be able to compare the results to other contact concepts reference values are given in Table 5.1.

It can be seen that the lowest selectivity is found for the phosphorus diffused contact, which shows a high contact resistivity of ρ_c = 260 m$\Omega\,$cm^2 and a high J_0 of 109 fA/cm^2 [27]. The low passivation quality is likely a consequence of the direct contact between the metal fingers and the c-Si, which is increasing the surface recombination as discussed in the Fundamentals Section 2.2. The developed TPC contacts show a slightly higher selectivity compared to the a-Si:H(i)/a-Si:H(n) contact reported in [37], which is due to a lower contact resistivity. The two highest selectivities are achieved with high temperature annealed SiO_2/poly-Si contacts, which show higher J_0 but a significantly lower contact resistivities [141, 173]. The highest

Table 5.1.: *Selected n-type contacts with the respective saturation current density (J_0), contact resistivity (ρ_c), and the logarithm of selectivity (S_{10}). A detailed overview of selectivities for specific contacts can be found in Schmidt et al. [38]. Values for η_{max} are calculated by Equation 2.26 with $\eta_{max} = P_{max}/P_{sun}$.*

contact	J_0 [fA/cm^2]	ρ_c [mΩ cm^2]	S_{10}	η_{max} [%]	Ref.
single layer SiC	6.7	24	14.2	28.24	
double layer SiC	2	38	14.5	29.53	
P-diffused n^+	109	260	12	24.95	[27]
a-Si:H(i)/a-Si:H(n)	2	100	14.1	29.42	[37]
SiO$_2$/poly-Si(n) [*chemical oxide*]	10	0.1	16.4	27.85	[173]
SiO$_2$/poly-Si(n) [*thermal oxide*]	49	0.003	17.2	26.14	[141]

selectivity with $S_{10} = 17.2$ is found for a contact produced by Gan and Swanson [141] and showed a J_0 of 49 fA/cm^2 and a ρ_c = 0.003 mΩ cm^2. It shows a comparably low passivation quality but an almost 2 order of magnitude lower contact resistivity as found for the next best samples, which showed an selectivity of 16.2. This low ρ_c result was achieved in 1990 and such a low contact resistivity has, to the best of my knowledge, never been achieved again in recent years within the PV community. How to measure a correct ρ_c especially for high conductive layer, as most poly-Si layers are, is an ongoing discussion in the photovoltaic community [53,100,173–175].

These results are also visualized in Figure 5.10 where the gray dashed lines represent the iso-selectivity lines, which are calculated using Equation 2.25. It can be seen that the double layer stack TPC significantly improves the J_0 compared to the single layer TPC. Nevertheless, it can be seen that this improves the selectivity only slightly. In comparison to the best SiO$_2$/poly-Si contacts the contact resistivity of the TPC is higher, which results in a lower selectivity. However, as discussed in the Fundamental Section 2.2 a higher selectivity does not necessarily results in a lower maximum efficiency. Achieving very low contact resistivities in combination with increased losses due to lower passivation as described by the model of Brendel and Peibst [27] might reduce the maximum efficiency. The maximum efficiency is

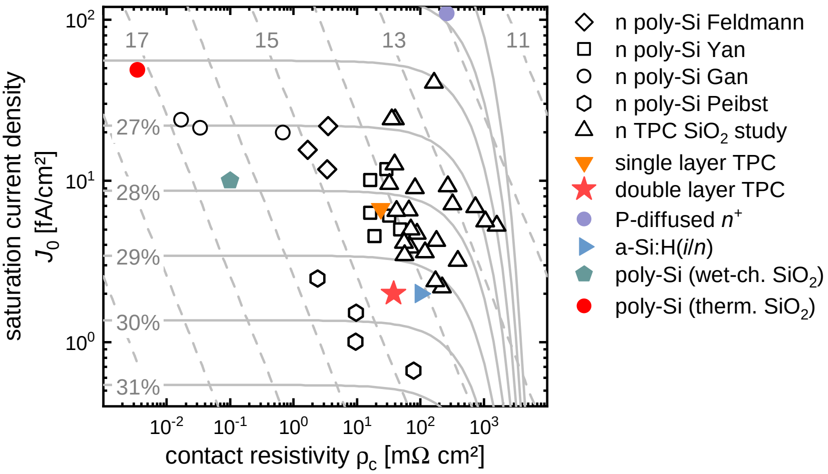

Figure 5.10.: *The saturation current density* (J_0) *as a function of the contact resistivity* (ρ_c) *for selected passivated contacts reported by several groups. Colored data points correspond to the results in Table 5.1. Open symbols have been previously shown in Figure 4.6. The gray dashed lines show the iso-selectivity* S_{10} *lines calculated by Equation 2.25. The gray solid lines show the iso-efficiency lines calculated by Equation 2.26. Data originally published in [27, 37, 53, 81, 121, 139–143, 173]*

.

calculated from Equation 2.26 with $\eta_{\max} = P_{\max}/P_{\text{sun}}$

The results of the calculation of $\eta_{\max}$ for single layer and double layer TPC ($S_{10} = 14.2$ and 14.5) give $\eta_{\max} = 28.20\%$ and 29.53%, respectively. For the SiO_2/poly-Si with the higher selectivity ($S_{10} = 17.2$) the $\eta_{\max}$ is 26.14% while for the SiO_2/poly-Si with the lower selectivity ($S_{10} = 16.4$) the $\eta_{\max}$ is 27.85%. These results show that a lower selectivity of a contact does not necessarily result in a lower maximum efficiency. The reason for that is the that the maximum efficiency depends on the balance between resistive losses and passivation losses. By optimizing this balance along an iso-selectivity line the maximum efficiency can be increased. This effect can be seen when comparing the SiO_2/poly-Si with the TPC contacts. Even though the SiO_2/poly-Si shows higher selectivities the achievable efficiency is higher for the TPC contacts due to the balance of resistive and passivation losses for these particular contacts.

To illustrate the difference between S_{10} and η_{max} in the model of Brendel and Peibst the efficiency of the SiO_2/poly-Si with thermally grown oxide shall be optimized while keeping the selectivity the same ($S_{10} = 17.2$). This sample has a very low contact resistivity, which is several orders of magnitude lower than the critical contact resistivity. When the area fraction of the conductive part is reduced while the area fraction of the passivation part is increased the maximum efficiency could be increased. By increasing the contact resistivity by one order of magnitude while keeping the selectivity the same (decreasing J_0) η_{max} could be increased to 28.5%, which is an increase of $2.4\%_{\mathrm{abs}}$. For contacts with ρ_{c} lower than the critical contact resistivity achieving a high passivation quality is very important to achieve higher η_{max}. This is the reason why the maximum efficiency is higher for TPC contacts as for SiO_2/poly-Si contacts with high S_{10}. These results show that the selectivity is a very valuable measure to optimize contacts regarding their passivation and resistive losses if they occur in separate areas on the wafer. However, this method of optimization cannot be applied to full area passivated contacts since resistive and passivation losses do not occur in spatially different locations.

To investigate the influence of the double layer stack on the solar cell performance series of changing $T_{\mathrm{f}}^{\mathrm{cond}}$ is repeated using solar cells with an a-Si:H(i)/ a-Si:H(p) rear side. Afterwards, the optimization of both layers regarding the passivation and contact properties has been performed. The results can be found in the following Chapter in Section 6.3.

5.4. Summary

In this Chapter the opto-electrical properties of µc-SiC:H(n) and the selectivity of the TPC contact were investigated. It was found that the lateral electrical conductivity of the µc-SiC:H(n) can be manipulated over 12 orders of magnitude by changing the hot-wire filament temperature. It could be shown that the content of nitrogen, which is a known donor in SiC, is only increased by 1.5 order of magnitude and therefore, cannot be the only reason for the strong increase in conductivity. It was found that by increasing the filament temperature the crystallite size of the µc-SiC:H(n) was increased, which increased the density of free charge carriers strongly.

It was also revealed that the optical bandgap as well as the sub-bandgap absorption of the µc-SiC:H(n) were increased with increased filament temperature. To investigate the influences of both parameters on the short circuit density the parasitic absorption loss was calculated in units of the current density. The lowest parasitic absorption of the 20 nm thick µc-SiC:H(n) was found for T_f = 1800 °C with 0.31 mA/cm^2.

Increasing the filament temperature resulted in decreased passivation quality. FTIR measurements of the Si–H bond revealed that the hydrogen content in the TPC is decreasing with increasing filament temperature. This finding was confirmed by the results of ToF-SIMS measurements. The decrease of passivation quality might originate from less hydrogen at the SiO_2/c-Si interface, which leads to a lower saturation of silicon dangling bonds. Additionally, increasing the filament temperature leads to more hydrogen radicals in the HWCVD chamber, which might lead to etching of the c-Si interface and thereby to an increase of dangling bonds. On the one hand, the highest passivation quality for a single layer µc-SiC:H(n) TPC using T_f = 1775 °C was measured to be iV_oc = 737 mV or J_0 = 5 fA/cm^2. However, due to a the low conductivity of the µc-SiC:H(n), which is a consequence of the low T_f, the contact resistivity could not be evaluated for this sample. On the other hand, the sample prepared at T_f = 1915 °C gave rise to the lowest contact resistivity of ρ_c = 24 mΩ cm^2 had an iV_oc of 715 mV.

The decrease of passivation quality for high filament temperatures could be prevented by using a double layer stack consisting of a passivating and a conductive µc-SiC:H(n), which are deposited at low and high filament temperatures, respectively. Therefore, a low contact resistivity of 38 mΩ cm^2 could be achieved while improving the passivation quality to iV_oc = 740 mV or J_0 = 2 fA/cm^2. These layers have not been optimized with respect to passivation or contact resistivity yet. To be able to compare the TPC contact with other n-type contact systems the selectivity S_{10} was calculated using the method of Brendel and Peibst [27]. The results reveal that the TPC shows a higher selectivity than a phosphorous diffused contact and an equal S_{10} compared the a-Si:H(i)/a-Si:H(n) contacts. However, contacts using SiO_2/poly-Si show higher selectivities, which can be explained by a lower contact resistivity. With respect to the maximum achievable efficiency the samples with TPC contacts showed an advantage compared to samples with SiO_2/poly-Si contacts. The reason is that the TPC samples show higher passivation quality while the contact resistivity is still below the critical limit. To investigate the influence of the double layer TPC on solar cells the contact was further optimized on cell level as presented in the following Chapter in Section 6.3.

6. Solar Cell Development with TPC Front Side

After developing an optimized buffer SiO_2 in Chapter 4 and investigating the electrical, optical, and passivation qualities of the µc-SiC:H(n) in Chapter 5, these findings are used to establish an efficient transparent passivating contact (TPC) for solar cells. For the solar cells in this Chapter random pyramid textured 170 µm thick Cz c-Si(n) <100> wafers are used. After fabrication of the TPC, the pn-junction are placed on the rear side of the solar cell using a stack of a-Si:H(i)/a-Si:H(p) deposited by PECVD. Then, the TCO layers are deposited on both sides of the solar cell by sputtering through a shadow mask to create four 2×2 cm^2 solar cells on each 78×78 mm^2 wafer. The metal contacts are realized either by evaporation of silver or screen printing of a low temperature silver paste followed by an oven annealing. For all experiments in this Chapter the rear contact is fully covered with 2×2 cm^2 silver.

In the first part of this Chapter selected wet-chemical oxidation methods (piranha, HNO_3, and SC-2) are used to investigate the influence of the different preparation methods for SiO_2 on solar cell level. In the second part the influence of the temperature of the hot-wire filaments is investigated with respect to the solar cell parameters. In the third part of this Chapter a functional layer stack of µc-SiC:H(n) is developed. In the fourth part several TCO deposition techniques and deposition conditions are investigated to reduce the passivation degradation after TCO deposition.

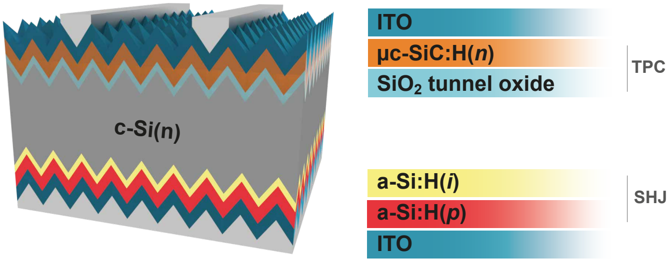

Figure 6.1.: *Solar cell concept with TPC on the light facing front side and a-Si:H(i)/a-Si:H(p) on the rear side followed by ITO and Ag electrodes.*

6.1. Solar Cells using selected SiO_2

In Chapter 4 it was found that different wet chemical oxidation methods result in different passivation qualities and contact resistivities. These values are strongly depending on the filament temperature during the HWCVD deposition of the µc-SiC:H(n). To be able to judge the influence of the contact resistivity on the series resistance as well as of the passivation quality on the V_{oc} solar cells were fabricated on 170 µm thick Cz dst c-Si(n) <100> wafers with a base resistivity of $1 - 5\ \Omega\,\mathrm{cm}^2$. The filament temperature was adjusted specifically for each oxidation method to achieve the best passivation quality. The T_f was chosen according to the results of the filament temperature series in Section 4.2 depicted in Figure 4.7 (a). For solar cells prepared with HNO_3 oxide the highest filament temperature of T_f = 1900 °C was used whilst for cells prepared in piranha solution T_f = 1820 °C was used. These T_f should enable high iV_{oc} and low ρ_c (see Figure 4.7). For cells prepared by SC-2 solution T_f = 1770 °C was used even though the maximum iV_{oc} is not expected at this T_f (see Figure 4.7 and Table 4.3). It is chosen to enable a lower series resistance. The silver contacts were thermally evaporated through a shadow mask. Deposition details of this experiment can be found in the Appendix A.1.

The JV results of the solar cells prepared with selected SiO_2 can be seen in Figure 6.2. For solar cells using piranha or HNO_3 oxidation two wafers are processed (marked in the Figure as I and II). The power conversion efficiency (η) shows that TPC solar cells using a HNO_3 or piranha oxide have equal efficiencies of $\eta = \sim 16\%$ while solar cells with SC-2 oxide show a lower efficiency of $\eta = 5\%$.

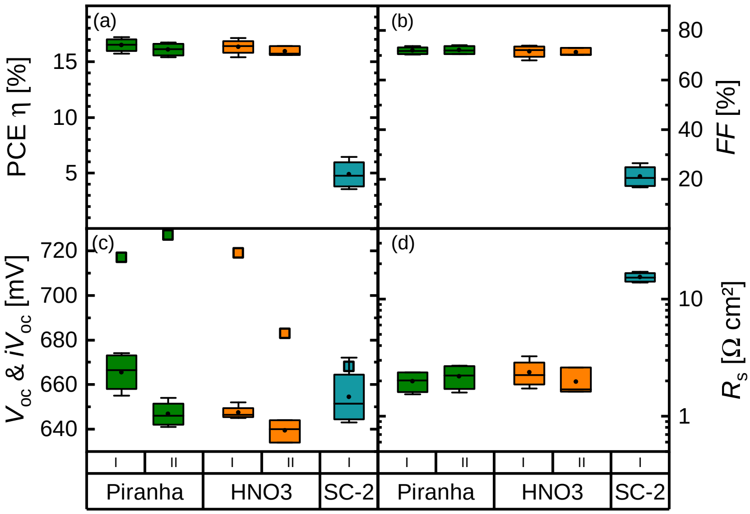

Figure 6.2.: *Solar cell series with tunnel oxide prepared with selected wet-chemical oxidation solutions (piranha, HNO_3, SC-2). The filament temperature of the µc-SiC:H(n) deposition was adjusted according to experiments on symmetric samples. T_f was 1820 °C, 1900 °C, and 1770 °C for piranha, HNO_3, and SC-2, respectively. (a) power conversion efficiency (η), (b) fill factor (FF), (c) open circuit voltage (V_{oc}), & implied open circuit voltage (iV_{oc}), and (d) series resistance (R_s) as a function of the selected oxidation solution. The colored box in the box plots depicts the values in the 25% – 75% range. The horizontal line within the box shows the median value and the circle shows the mean value.*

This difference is also reflected in the fill factor, which is significantly lower for the solar cells prepared by SC-2 oxide $FF \approx 21\%$ due to an s-shape of the JV curve compared to the solar cells prepared using HNO_3 or piranha with $FF = 72\%$. The reason for the difference in FF can be found in the R_s, which is approximately one order of magnitude higher for the solar cells prepared using SC-2 oxide and leads to an s-shape of the JV-curve. The reason for the high series resistance is likely the low electrical conductivity ($\sigma \approx 10^{-8}$ S/cm) of the µc-SiC:H(n) deposited at $T_f = 1770$ °C (see Figure 5.1 a). Higher filament temperatures for cells prepared with SC-2 oxide would lead to $iV_{oc} < 700$ mV (see Figure 4.7 a). Thus oxidation in SC-2 solution does not lead to high efficiency. The solar cells prepared with

HNO_3 or piranha oxide show a $R_s < 3\ \Omega\,\mathrm{cm}^2$, which is most likely a consequence of the low contact resistivities $\rho_c < 100\ \mathrm{m}\Omega\,\mathrm{cm}^2$ of the TPC (see Figure 4.7 b). Nevertheless, for the solar cells with SiO_2 prepared by piranha or HNO_3 the series resistances and the fill factors are comparable even though the µc-SiC:H(n) was deposited at different filament temperatures. Furthermore, the thickness of the HNO_3 oxide layer is larger than for the piranha oxide, which could additionally lead to an increased series resistance, since the tunnel probability is lower. Both effects might also equalize each other, since for the thicker oxide (HNO_3) also the higher conductive µc-SiC:H(n) was used while the piranha oxide layer is thinner but the µc-SiC:H(n) had a lower conductivity.

In Figure 6.2 (c) the iV_{oc} (squares) and the V_{oc} (boxes) are plotted. It can be seen that the iV_{oc} is strongly fluctuating within two samples, which are nominally prepared using the same deposition conditions. The reason for that might be a low reproducibility of the µc-SiC:H(n) layer quality. Since the hot-wire deposition system is a single sample system, no batch depositions can be performed. Therefore, fluctuations can occur between depositions especially when the filament temperature is changing even though the deposition parameters are nominally the same.

The iV_{oc} is measured after the fabrication of the passivation layers on front and back side (TPC and back side a-Si:H before TCO). The sample is called in the following the «solar cell precursor». The V_{oc} is measured after the deposition of TCO and metallization. The lowest passivation of the solar cell precursor is found for the solar cells prepared using SC-2 oxidation. The iV_{oc} is 668 mV while for the symmetric samples the iV_{oc} is 712 mV at $T_f = 1765$ °C (see Figure 4.7 a). The reason for this discrepancy between symmetric and solar cell precursor in iV_{oc} might be due to the narrow process window of the T_f. As it can be seen in Figure 4.7 (a) the iV_{oc} is dropping strongly for $T_f > 1765$ °C. However, lower T_f cannot be used due to the high R_s and low FF of these cells. It can be concluded that neither a sufficient passivation nor a suitable series resistance could be achieved for cells prepared by SC-2 SiO_2. Therefore, SC-2 oxidation is not a viable option for TPC solar cells in this configuration.

Additionally, it was found that a strong drop in passivation quality occurs from precursors to finished solar cells. This can also be seen in the difference between iV_{oc} (before ITO) and V_{oc} (after ITO and Ag deposition). The reason for this drop is a damage of the passivation during the sputtering of the ITO. With symmetric passivation samples (TCO/µc-SiC:H(n)/SiO_2/c-Si/SiO_2/µc-SiC:H(n)/TCO) it is confirmed that the deterioration of the passivation is happening on the TPC front side rather than on the a-Si:H(i)/a-Si:H(p) rear side. A reduced passivation quality after sputtering is known for contact systems using a-Si:H or SiO_2/poly-Si layers [57, 58, 176, 177]. A more detailed investigation of the sputter damage on the TPC and an optimization of the sputtering conditions can be found in Section 6.4.

To increase the efficiency of the solar cells, the filament temperature of the µc-SiC:H(n) deposition has to be optimized to find the best trade-off between high iV_{oc} and high FF for a specific oxide. As found in Chapter 4, oxidation in piranha solution results in the highest passivation quality for symmetric samples. This can also be seen for the solar cell precursors and result highest V_{oc} of the finished solar cell in this experiment. Therefore, oxidation in piranha solution for 10 min was chosen as the standard oxidation method for the following experiments to optimize the solar cell performance.

6.2. Single layer TPC solar cells

To further optimize the trade-off between the passivation quality and the fill factor, solar cells are prepared using selected filament temperatures during HWCVD deposition. The filament temperature was varied between $T_{\mathrm{f}} = 1810$ °C – 1915 °C. Since in Chapter 4 and in Section 6.1 it was found that SiO_2 prepared in piranha solution shows the best passivation quality as well as the highest solar cell efficiency, all solar cells have been prepared by 10 min oxidation in piranha solution. To be able to compare the results for TPC solar cells, reference solar cells with an a-Si:H(i)/a-Si:H(n) front contact have been produced in the same batch. For these experiments higher quality dst Cz wafers with a base resistivity of 1 $\Omega\,\mathrm{cm}^2$ are used. Additionally, the a-Si:H(i)/a-Si:H(p) deposition conditions on the rear side are improved, which enable higher passivation qualities on the rear side. Furthermore,

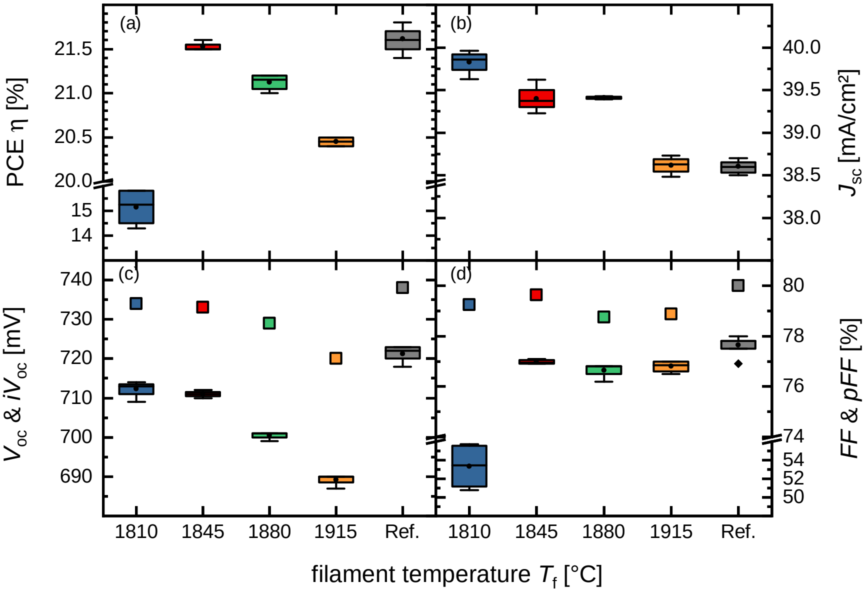

Figure 6.3.: *Solar cell series with µc-SiC:H(n) deposited at selected filament temperature* T_f*. Reference cells (Ref.) were produced, which have the same rear contact but an a-Si:H(i)/a-Si:H(n) front contact compared to the TPC cells. (a) Power conversion efficiency (*η*), (b) short circuit current density (*J_{sc}*), (c) open circuit voltage (*V_{oc}*) & implied open circuit voltage (*iV_{oc}*) (squares), and (d) fill factor (*FF*) & pseudo fill factor (*pFF*) (squares) as a function of* T_f*. The colored box in the box plots depicts the values in the 25% – 75% range. The horizontal line within the box shows the median value and the circle shows the mean value.*

the contacts are realized by screen printing of a low temperature paste. Details regarding the deposition conditions can be found in the Appendix A.2.

Photovoltaic Parameters The results of the efficiency, the J_{sc}, iV_{oc}, and V_{oc} as well as pFF and FF as a function of selected filament temperatures are plotted in Figure 6.3. It can be seen that the solar cells with the best efficiency are produced at $T_f = 1845$ °C. The best solar cells in this experiment have an $\eta = 21.6\%$, $J_{sc} = 39.5$ mA/cm^2, $V_{oc} = 709$ mV, and a $FF = 77.1\%$. For lower $T_f = 1810$ °C a higher V_{oc} is achieved. The decreased T_f, however, resulted in a decreased $FF < 56\%$.

Table 6.1.: *Difference in the passivation quality before sputtering of ITO (iV_{oc}) and after sputtering (V_{oc}). The passivation is deteriorated after sputtering. The drop is correlated to T_f.*

T_f [°C]	iV_{oc} [mV]	V_{oc} [mV]	$iV_{oc}-V_{oc}$ [mV]
1810	734	712	22
1845	733	711	22
1880	729	701	28
1915	720	689	31
Ref.	738	721	17

The low FF is a direct consequence of the high series resistance of $R_s = 6.5\ \Omega\,\mathrm{cm}^2$. For the best solar cell the series resistance is one order of magnitude lower. The reason for this high series resistance is most likely the electrical conductivity of the µc-SiC:H(n) as shown in Figure 5.1 (a).

Regarding the iV_{oc} it can be seen that the passivation quality is dropping when T_f is increased. This decrease was already found for symmetrically passivated samples (see Figure 5.7 a). As a direct consequence the V_{oc} is dropping. However, it can be seen that the difference between iV_{oc} and V_{oc} becomes larger for higher T_f (see Table 6.1). For $T_f = 1810$ °C and 1845 °C the difference is 22 mV. For $T_f = 1915$ the difference is 31 mV while for the SHJ reference the difference is 17 mV. This leads to the conclusion that the damage due to the sputtering of ITO is more severe for µc-SiC:H(n) layers deposited at higher T_f. Additionally, for the cells with TPC the sputter damage is more severe than for the reference cell, since for the reference the drop from iV_{oc} to V_{oc} is lower. This suggests that the ITO deposition is causing less damage on the a-Si:H layer passivated contact than on the TPC passivated contact. One reason for that might be that the applied standard sputter deposition is optimized for the use with a-Si:H layers. Optimization of TCO layers for TPC solar cells and curing procedures are investigated in Section 6.4.

Besides the solar cells deposited at the lowest T_f all solar cells show an equal fill factor. This result is unexpected, since for higher filament temperatures the contact resistivity of the TPC is decreased (see Figure 5.7 c). The reason for the constant fill factor and also a constant series resistance might be that the rear side contact is the limiting contact for the series resistance rather than the front side contact. This finding is stressed by the results of the reference solar cell, which uses the same rear side as the TPC solar cells and also shows a similar fill factor.

Fill Factor Analysis To further investigate the origin of fill factor losses, a fill factor loss analysis [178] based on a two-diode model [103] is performed. Since the FF is very sensitive to resistive and recombination losses, the losses are parameterized by the series resistance (R_s), shunt resistance (R_sh), and the recombination current densities of both diodes (J_{01} and J_{02}). Losses in J_{01} are usually attributed to recombination of charge carriers in regions with $n \neq p$, e.g. in the bulk, while losses in J_{02} are usually attributed to recombination regions with $n = p$, e.g. the space charge region or edge recombination [16, 17, 179]. Edge recombination of these solar cells can be excluded, since the solar cells are placed in the middle of the wafer sufficiently far away from the edges to suppress recombination. However, recombination in the dark areas of the solar cell, which are not illuminated due to the mask during measurements, contribute to J_{02} as well. This specific loss is not investigated in this case since the shaded areas are equal for all cells.

Using the fill factor loss analysis the upper fill factor limit is calculated when only the recombination current density of the first diode J_{01} is contributing to the FF loss (FF_J01). These losses can only be mitigated by improving the bulk silicon material of the wafer. The upper limits for the FF for the best TPC solar cell and the best reference solar cell are calculated to be 84.7% and 84.9%, respectively. Since both samples are prepared using the same wafer batch, the FF_J01 is expected to be equal. The results of the analysis are shown in Table 6.2 and reveal that the major loss in fill factor is occurring in the space charge region due to J_{02}. The value for both solar cells is similar. This was expected because both solar cells are utilizing the same rear side junction. Nevertheless, the TPC solar cell is loosing additional $0.8\%_\mathrm{abs}$ in FF due to a higher series resistance compared to the reference solar cell. This loss can be attributed to the higher contact resistivity of the TPC compared to the a-Si:H(i)/a-Si:H(n) front contact.

When comparing the best TPC solar cells (T_f = 1845 °C) with the best SHJ reference solar cells both show a comparable efficiency. Nevertheless, the V_oc of the the TPC cell is 9 mV lower then the V_oc of the reference cell. This disadvantage of the TPC cell is compensated by the J_sc, which is 0.8 mA/cm^2 higher for the TPC cells than for the reference cells. This superior J_sc is a consequence of the wider optical bandgap of TPC compared to the a-Si:H(i)/a-Si:H(n) front side.

Quantum Efficiency The advantage due to the optical properties of the TPC compared to the complete a-Si:H SHJ solar cell can be seen in Figure 6.4. The IQE, EQE and R are plotted as a function of the wavelength (λ) for three selected T_f and the SHJ reference. The measurements are performed with a 12×12 mm^2 light spot on the aperture area of the solar cells. Therefore, reflection is not only due to the active surface of the solar cell but also due to metal fingers.

It can be seen that the EQE is significantly higher in the wavelength range between 300 nm and 600 nm for the TPC solar cells than for the reference solar cells (see Figure 6.4 b). Partially the lower reflection losses for the TPC cells are a reason for the higher EQE, which can be seen in the reflectance data in Figure 6.4 (c). The reason for the lower reflectance of the TPC is a better refractive index matching for the layer stack as shown in Pomaska et al. [180]. Nevertheless, reflection can only account for a part of the optical losses. This can be seen in the IQE results, which are the EQE results corrected for the different reflectances (see Figure 6.4 a). The majority of the optical loss for the a-Si:H front side is due to parasitic absorption resulting from a higher absorption coefficient compared to the µc-SiC:H(n) [10]. It can also be seen that the IQE and EQE results for T_f = 1810 °C and 1845 °C

Table 6.2.: *Results of the fill factor loss analysis for the best TPC and SHJ reference solar cell.*

		TPC	SHJ ref.
FF_J01	[%]	84.7	84.9
ΔFF_J02	[%]	4.6	4.55
ΔFF_Rs	[%]	2.9	2.1
ΔFF_Rsh	[%]	0.2	0.2

are very similar while for the sample deposited at T_f = 1915 °C both EQE and IQE are reduced for the entire wavelength range between 400 nm and 1100 nm by 2.5%$_\mathrm{abs}$. This reduction might be due to the reduced passivation quality for the sample deposited at elevated temperatures, since it is decreased over the entire wavelength range.

Additionally, it can be seen that the reflectance of the TPC cells is correlated with the filament temperature. This might have two reasons. For higher T_f the layer thickness of the µc-SiC:H(n) is slightly smaller thus the reflection maximum shows a blue shift [180]. Furthermore, the refractive index of µc-SiC:H(n) decreases with increased filament temperature, thus also changes the reflectance of the stack.

It can be summarized that by increasing the filament temperature from T_f = 1800 °C as it was used in the first experiment, to 1845 °C the efficiency of the solar cells can be increased. The main improvements are achieved for the V_oc and the FF. Due to higher quality wafers and an improved a-Si:H(i)/a-Si:H(p) rear contact higher efficiencies were enabled. It should be noted that throughout the experiments of this work the reference cells and therefore also the back contact of the TPC cells is constantly improved as well.

In comparison to the SHJ reference cells the best TPC cells show an equal efficiency. It was found that due to the lower parasitic absorption of the µc-SiC:H(n) the J_sc is 0.8 mA/cm^2 higher than for the reference cells. The FF of the TPC cells was lower due to a higher series resistance, which can be attributed to the TPC front contact. Also the V_oc of the TPC cell is lower due to a lower initial passivation quality and stronger deterioration during ITO sputtering. To overcome these drawbacks, the FF and the initial passivation (iV_oc) need to be increased in a first step. In a second step the sputter degradation needs to be minimized or cured, which then should increase the V_oc. Both optimizations will be discussed in the following sections.

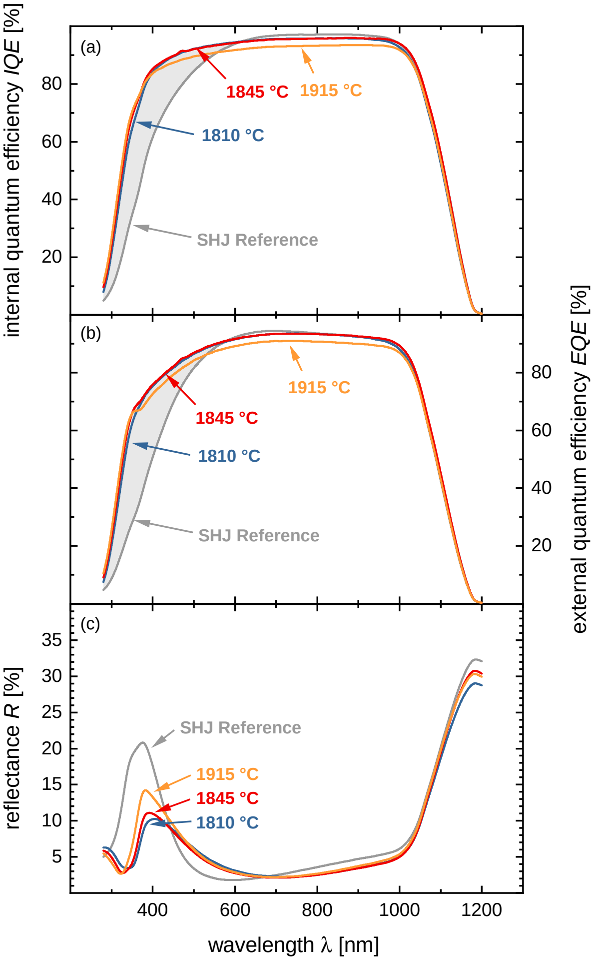

Figure 6.4.: *Electro-optical results for solar cells with µc-SiC:H(n) deposited at selected filament temperatures. (a) The internal quantum efficiency (IQE), (b) external quantum efficiency (EQE) and (c) reflectance (R) as a function of the wavelength (λ) for solar cells with TPC fabricated at three selected T_f and for the a-Si:H-SHJ reference cell. The gray area marks the wavelength range where the IQE and EQE results of the TPC are superior to the ones of the reference cell. Due to the higher optical bandgap of µc-SiC:H(n) compared to a-Si:H the IQE and EQE are higher in the short wavelength range.*

6.3. Double layer TPC solar cells

In Section 5.3 it was found that a double layer stack, consisting of a passivating µc-SiC:H(n) layer deposited at lower T_f and a conductive µc-SiC:H(n) deposited at elevated T_f, can maintain the passivation quality (mean iV_oc = 738 mV) for increased T_f of the TPC. Additionally, it was found that a low contact resistivity of $\rho_\mathrm{c} = 38\ \mathrm{m\Omega\,cm^2}$ can be achieved even though the thin passivation layer has a low electrical conductivity. These results were obtained on symmetrically passivated samples. Therefore, the double layer stack will be investigated and improved in solar cells in the following Section. A sketch of the solar cell device can be found in Figure 6.5.

6.3.1. Conductive µc-SiC:H(n) layer variation

In the first study according to the experiment with symmetrically passivated samples the filament temperature of the conductive layer ($T_\mathrm{f}^\mathrm{cond}$) is varied. The goal is to investigate the influence of the increased $T_\mathrm{f}^\mathrm{cond}$ on the V_oc, and FF. For this experiment wafers of the same batch as for the solar cells in Section 6.2 are oxidized in piranha solution. Afterwards, the µc-SiC:H(n) double layer is deposited with a 9 nm thick passivation layer at filament temperature of the passivation layer ($T_\mathrm{f}^\mathrm{pass}$) = 1775 °C and a 25 – 30 nm thick conductive layer at $T_\mathrm{f}^\mathrm{cond}$ = 1895 °C – 2045 °C. The deposition parameters for the rear side a-Si:H(i)/a-Si:H(p) and TCO layers were the same as for the single layer cells and can be found in the Appendix A.2. The results for η, J_sc, iV_oc & V_oc, as well as pFF & FF of this conductive layer series can be found in Figure 6.6.

It can be seen that iV_oc is fluctuating between 733 mV – 738 mV, which is slightly lower than for symmetrically passivated samples. Is was frequently observed that the solar cell precursors (asymmetric, after µc-SiC:H(n) and a-Si:H, but before ITO deposition) showed a slightly lower passivation quality than the symmetric samples. After finishing the solar cell by ITO deposition and metallization the resulting V_oc is measured to be 706 mV – 715 mV with a mean V_oc of 712 mV. This obtained V_oc values are equal to the V_oc results of the best single layer solar cell (see Figure 6.3 c).

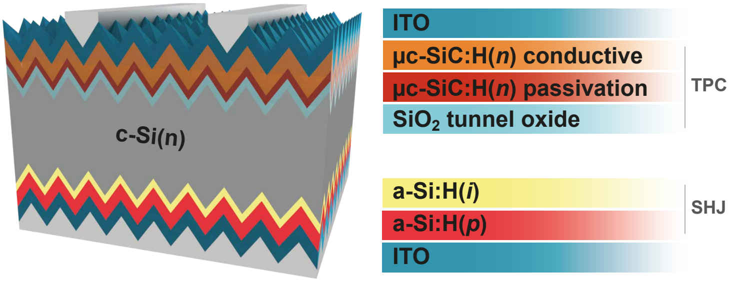

Figure 6.5.: *Solar cell concept with a double layer stack µc-SiC:H(n) on the light facing front side and a-Si:H(i)/a-Si:H(p) on the rear side. The double layer consists of a thin passivation layer on top of the SiO_2 and a conductive layer on top of the passivation layer. This sketch was originally published in [9] (CC BY 4.0).*

As expected from the results in Section 5.3 and Figure 5.9, the iV_{oc} is not influenced by T_{f} of the conductive layer, since the first µc-SiC:H(n) layer provides the surface passivation. Additionally, the FF is not increasing with increasing T_{f}, which is due to a series resistance in the range of $R_{\mathrm{s}} = 1.1 - 1.6\ \Omega\,\mathrm{cm}^2$ without a clear trend regarding $T_{\mathrm{f}}^{\mathrm{cond}}$. A constant series resistance can also be expected since the contact resistivity also did not show a dependency on $T_{\mathrm{f}}^{\mathrm{cond}}$. Although the mean contact resistivity of the double layer TPC stack was comparably low with $\rho_{\mathrm{c}} = 69\ \mathrm{m}\Omega\,\mathrm{cm}^2$ (see Figure 5.9 b), the series resistance of the solar cells is high with $R_{\mathrm{s}} > 1\ \Omega\,\mathrm{cm}^2$. Thus, the FF is limited to a maximum of 75.2%. Therefore, the deposition conditions of the double layer stack need to be improved.

To optimize the series resistance and the efficiency of the device three deposition parameters for both µc-SiC:H(n) layers are found to be important. The filament temperature for both layers should be optimized to achieve a high passivation quality and high conductivity of the layers. The thicknesses of the layers need to be optimized to reduce the contact resistivity while maintaining a high passivation quality. The third parameter, which might also influence the conductivity of the µc-SiC:H(n) layers, is the doping gas flow rate F_{N2}. It should be noted that other deposition parameters e.g. substrate temperature, MMS flow rate, might also influence the performance of the double layer stack but are not tested in this work.

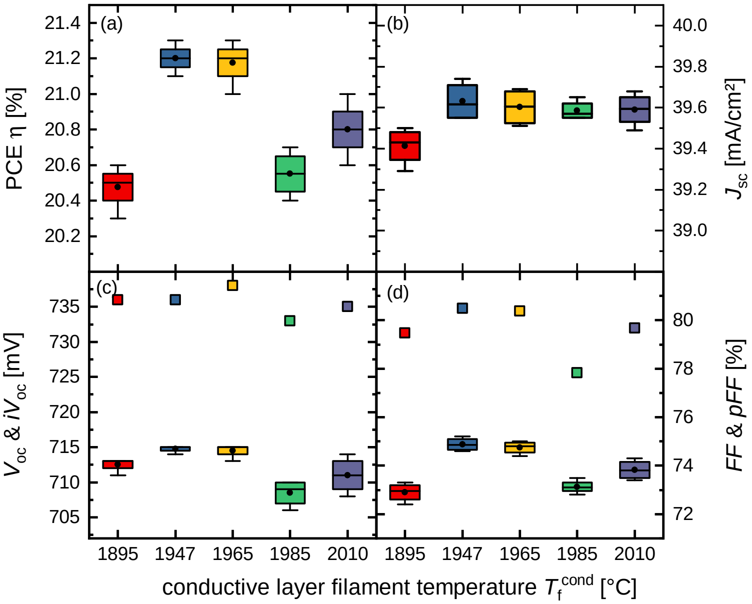

Figure 6.6.: *Solar cell series using a double layer stack of µc-SiC:H(n) with a variation of the conductive layer filament temperature. (a) The power conversion efficiency (η), (b) short circuit current density (J_{sc}), (c) open circuit voltage (V_{oc}) & implied open circuit voltage (iV_{oc}), and (d) fill factor (FF) & pseudo fill factor (pFF) as a function of T_f^{cond}. The colored box in the box plots depicts the values in the 25% – 75% range. The horizontal line within the box shows the median value and the circle shows the mean value.*

6.3.2. Double layer stack optimization

To be able to investigate the influences of the selected deposition parameters of both the passivation and the conductive layer on the properties of solar cells, a design of experiment (DoE) is used. To reduce the number of parameters the flow rate of nitrogen gas (F_{N2}) is not changed within the deposition of passivation and conductive layer. The F_{N2} is only changed between samples. Therefore, five factors, each on a high and a low level, have been investigated:

- thickness of the µc-SiC:H(n) passivation layer ($d_{\mathrm{SiC}}^{\mathrm{pass}}$),
- filament temperature of the passivation layer ($T_{\mathrm{f}}^{\mathrm{pass}}$),

- thickness of the µc-SiC:H(n) conductive layer ($d_{\mathrm{SiC}}^{\mathrm{cond}}$),
- filament temperature of the conductive layer ($T_{\mathrm{f}}^{\mathrm{cond}}$),
- flow rate of nitrogen gas (F_{N2}).

Checking all parameter combinations would result in $2^5 = 32$ experiments, which is also known as a «full factorial design». The advantage of this plan is that all dependencies of all tested parameters are revealed. The disadvantage is the high number of experiments which are needed. The number of experiments can be reduced by using a «fractional factorial design» to $2^{5-1} = 16$ experiments. The disadvantage of the fractional factorial plan is that not all parameter combination are tested, thus, no complete variation of one parameter can be evaluated. Therefore, the «effects» of each deposition parameter on each solar cell parameter can be investigated. Three center points have been added to the DoE where all levels are 0.5 of the high level values to judge if an effect has a significant influence on the result. The full experimental matrix can be found in the Appendix A.3. The effect (E) of the i-th parameter can be calculated by subtracting the mean result when the parameter is «low» ($\bar{y}_{\mathrm{low}}$) from the mean solar cell result when the parameter is «high» ($\bar{y}_{\mathrm{high}}$)

$$E_{\mathrm{i}} = \bar{y}_{\mathrm{high}} - \bar{y}_{\mathrm{low}}. \tag{6.1}$$

Since in the last experiment it was shown that the FF is the critical parameter for the efficiency of TPC solar cells the focus was set to reach high FF and low R_{s} while maintaining a high iV_{oc}. The resulting effects on the device parameters of the solar cell are plotted in Figure 6.7. The effects on the fill factor show that FF can be mainly increased by reducing the layer thickness and increasing the filament temperature of the passivation layer (see Figure 6.7 (a)). A lower thickness of the conductive layer and an increased doping gas flow also improve the fill factor slightly. The improvement in fill factor can be mainly attributed to a decrease in series resistance, which can be seen in Figure 6.7 (b). It should be noted that positive effects increase the series resistance. However, the series resistance of a solar cell should rather be decreased. Therefore, positive effects on R_{s} should rather be set to the low level and vice versa. In conclusion, a low thickness and a high filament temperature of the passivation layer are decreasing the series resistance. This leads to the conclusion that the series resistance mainly depends on the parameters of the passivation layer. Since an increased filament temperature T_f^{pass} from 1775 °C to 1875 °C increases the electrical conductivity of the µc-SiC:H(n) from approximately 10^{-8} S/cm to 10^{-2} S/cm (see Figure 5.1), the contact resistivity of the TPC can be reduced. Additionally, reducing the thickness of the passivation layer also

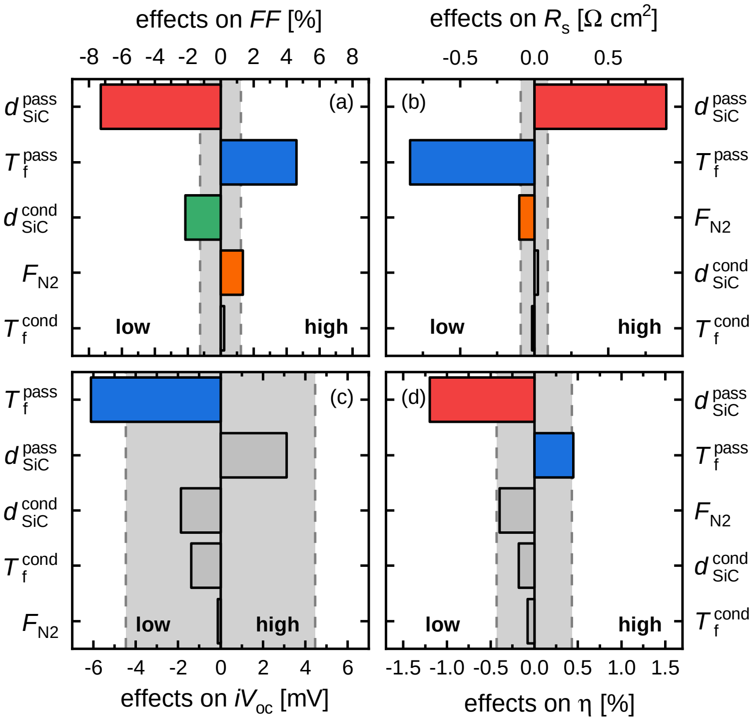

Figure 6.7.: *Effects of the five deposition parameters calculated by Equation 6.1 on the (a) fill factor (FF), (b) series resistance (R_s), (c) implied open circuit voltage (iV_{oc}), and (d) power conversion efficiency (η) of the solar cells. The color of the bar represents the parameter. The effects are plotted from the largest absolute effect to the lowest absolute effect from top to bottom. The dashed lines mark the significance value, which is calculated from the results obtained at the center point of the DoE. The absolute effects need to exceed this value in order to be significant. A negative effect means that in other to increase the result the parameters should be set to the low value. For a positive effect the parameter should be set to the high value to increase the result. This figure was originally published in [9] and was adapted (CC BY 4.0).*

contributes to a decreased contact resistivity of the front side, which then results in a decreased series resistance. These findings are also stressed by the results of the $T_\mathrm{f}^\mathrm{cond}$ series shown in Figure 6.6 where it is found that the filament temperature of the conductive layer has no significant influence on the series resistance and fill factor due to the dominating effect of the passivation layer.

Regarding the iV_oc, increasing the filament temperature of the passivation layer by 100 °C can also result in a degradation of the passivation as shown before. To investigate the effects on the passivation without the influence of the ITO sputtering the iV_oc rather than the V_oc is evaluated in Figure 6.7 (c). Due to scattering of the iV_oc results of the center points the significance value is large compared to the effects. Only the influence of $T_\mathrm{f}^\mathrm{pass}$ is found to surpass the significance threshold. As expected, using the lower rather than the higher filament temperature results in an improved iV_oc. As discussed in Section 5.3 the µc-SiC:H(n) layers deposited at elevated T_f contain less hydrogen and more atomic hydrogen is produced during HWCVD, which can impair the SiO_2/c-Si interface. Additionally, the substrate temperature also increases for increasing T_f due to a higher thermal radiation, which might lead to a diffusion or desorption of hydrogen at the interface. Also, a decrease of the layer thickness of the passivation layer might lead to a deterioration since the barrier against the radicals is thinner.

The effects on the solar cell efficiency are plotted in Figure 6.7 (d). It can be seen that only the thickness and the filament temperature of the passivation layer show a significant influence on the solar cell efficiency. To improve the efficiency the d_SiC should be decreased while the $T_\mathrm{f}^\mathrm{pass}$ should be increased. This is the same trend as observed for the FF and R_s results, which leads to the conclusion that efficiency in this experiment is mostly influence by the fill factor rather than by the passivation quality. Since the thickness of the passivation layer has such a large impact on the device performance, the influence on the series resistance and fill factor was additionally investigated as shown in Figure 6.8. It can be seen that the mean series resistance can be decreased from $R_\mathrm{s} = 2.6\,\Omega\,\mathrm{cm}^2$ to $0.6\,\Omega\,\mathrm{cm}^2$ by reducing $d_\mathrm{SiC}^\mathrm{pass}$ from 13 nm to 3 nm. In the same interval the fill factor increased from $FF = 63\%$ to 76.5%. It can therefore be concluded that a low thickness of the passivation layer is necessary to provide high fill factors. Nevertheless, the passivation layer cannot

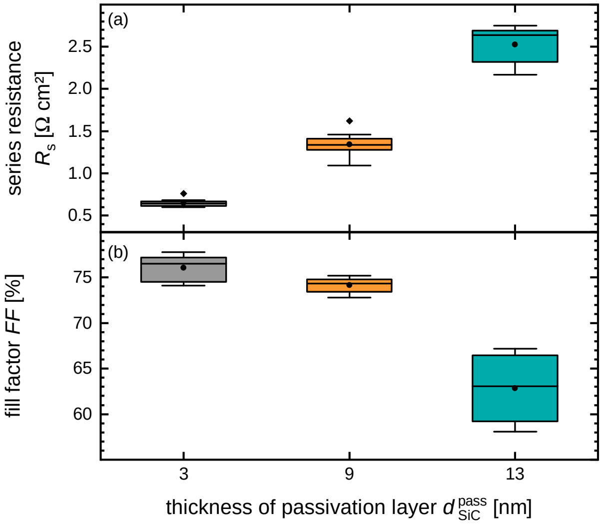

Figure 6.8.: *Solar cell series using a double layer stack of µc-SiC:H(n) with variation of the passivation layer thickness. (a) The series resistance (R_s) and (b) the fill factor (FF) as a function of the $d_{\mathrm{SiC}}^{\mathrm{pass}}$. The colored box in the box plots depicts the values in the 25% – 75% range. The horizontal line within the box shows the median value and the circle shows the mean value. This figure was originally published in [9] and was adapted (CC BY 4.0).*

be completely removed, since this drastically decreases the passivation quality as it was found for single layer TPC in Figure 5.7 (a). Additionally, it is also found for $d_{\mathrm{SiC}}^{\mathrm{pass}} = 3$ nm that a high iV_{oc} of 734 mV can only be achieved for the lower $T_{\mathrm{f}}^{\mathrm{cond}} = 1950$ °C while for $T_{\mathrm{f}}^{\mathrm{cond}} = 2060$ °C the iV_{oc} drops to 714 mV (not shown). This leads to the conclusion that the passivation layer is too thin to ensure high passivation quality of the device.

The results of the DoE for the J_{sc} (not shown) suggest that $d_{\mathrm{SiC}}^{\mathrm{pass}}$ should be increased and $T_{\mathrm{f}}^{\mathrm{pass}}$ should be decreased in order to increase the short circuit current density. However, increasing the J_{sc} is not the focus in this chapter, thus the results are not discussed in detail here. Finally the best solar cell of the DoE experiments is achieved with $d_{\mathrm{SiC}}^{\mathrm{pass}} = 3$ nm and $T_{\mathrm{f}}^{\mathrm{pass}} = 1775$ °C («low») and shows an $\eta = 22\%$, $iV_{\mathrm{oc}} = 727$ mV, $V_{\mathrm{oc}} = 711$ mV, $FF = 77.8\%$, and a $J_{\mathrm{sc}} = 39.75$ mA/cm^2. Interestingly, this sample shows the lowest drop from iV_{oc} to V_{oc} of all samples with 16 mV, which leads to the conclusion that the TCO deposition has the lowest impact on the passivation quality. The mean drop from iV_{oc} to V_{oc} within this experiment is 32 mV.

It can be concluded that in this work tuning the passivation layer properties has the stronger influence on the solar cell performance compared to the conductive layer properties or the doping gas flow. To increase the fill factor of the solar cell it is necessary to reduce the thickness of the passivation layer. Still, the solar cells suffer from a deterioration of the passivation quality after sputtering of the ITO. Therefore, alternative deposition methods and TCO materials are investigated in the following Section.

6.4. TCO development for TPC

Within this work very high passivation qualities of $iV_{\mathrm{oc}} = 740$ mV and $J_0 = 2$ fA/cm^2 were achieved with the TPC. This high passivation quality should enable very high V_{oc} of the final solar cell. However, the highest V_{oc} so far was found to be 714 mV (see Figure 6.6). In the optimization experiment for the double layer stack, the mean drop from iV_{oc} to V_{oc} was 32 mV. For the SHJ reference cells using an a-Si:H(i)/a-Si:H(n) front contact the mean drop from iV_{oc} to V_{oc} was 12 mV. The origin of this deterioration was identified to be the sputter deposition of the ITO. This drop was therefore not only found from iV_{oc} to V_{oc} but also from iV_{oc} before to iV_{oc} after ITO sputtering. This drop can be visualized by lifetime corrected photo-luminescence (PL) imaging as it is shown in Figure 6.9. The color code displays the effective minority carrier lifetime in microseconds. The ITO is sputtered through a shadow mask, which results in four 2×2 cm^2 areas and several test structures around these solar cells. The areas of the wafer, which are covered by the mask, are not exposed to the deposition and are only heated by the substrate heater during the physical vapor deposition (PVD). It can be seen that the lifetime is strongly decreased in the areas where the ITO is deposited and the lifetime is not effected in the masked areas. This leads to the conclusion that the heating of the substrate is not causing the degradation of the passivation quality. This finding is

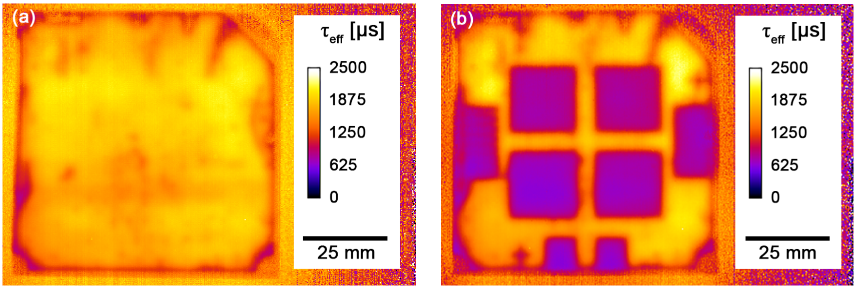

Figure 6.9.: *Lifetime corrected photo-luminescence (PL) image of a solar cell precursor before (a) and after (b) ITO deposition through a mask. The images are corrected with effective minority carrier lifetime (τ_{eff}) lifetime measured by photo-conductance (PC). The color code shows τ_{eff} in microseconds. The lifetime is degraded in the unmasked areas, which were exposed during deposition.*

stressed by annealing experiments of symmetrically passivated µc-SiC:H(n) samples (not shown). It was found that the iV_{oc} is drops by 1% for temperatures >320 °C thus sputtering at 200 °C should not affect the passivation. Therefore, the degradation is most likely caused by the sputter deposition. Degradation due to sputtering is also found for contacts prepared by SiO_2/poly-Si [57, 58] or a-Si:H [181, 182]. The possible origins of the TPC degradation are discussed in the following Section.

6.4.1. Mechanisms of sputter degradation

Degradation due to sputtering can mainly be caused in two different ways. A first degradation mechanism can occur due to a strong particle bombardment during sputtering, which may have enough energy to damage the c-Si/SiO_2 interface [183]. The bombardment can be due to high energy secondary ions sputtered from the target or due to argon (Ar) ions, which are neutralized at the target and reflected back onto the sample [184]. The energy of the particles hitting the substrate can be controlled by the sputter pressure. By increasing the sputter pressure, the mean free path of the sputtered ions is shorter, which results in more inelastic scattering. Due to inelastic scattering the ions lose kinetic energy on their way to the substrate. The mean free path can be decreased by increasing the sputter pressure. If the energy of the secondary ions is high enough to impair the c-Si interface, an important measure is the flux density of the particles. This flux density can be controlled by the sputter power. By decreasing the sputter power the primary ions hitting the target have less energy. Additionally, the primary Ar ions have less energy when they are neutralized and reflected from the target towards the sample. Therefore, the flux density of the sputtered ions is reduced since less secondary ions are knocked out of the target [185]. Changing the sputter pressure and power can influence the ion bombardment damage, thus can directly affects the V_{oc} of the solar cells.

A second mechanism which can degrade the passivation is ultraviolet radiation (UV) from the plasma during sputtering [186]. Due to the high transparency of the TPC this effect might be even more detrimental than for poly-Si or a-Si:H layers, which have a higher optical absorption. It was found by Profijt et al. that an emission of the oxygen plasma at 130.5 nm or 9.5 eV significantly decreases the passivation quality of a Al_2O_3 passivated c-Si wafer [187]. This vacuum ultraviolet radiation (VUV) has enough energy to break Si–H bonds (3.1 eV) and Si–O bonds (8.3 eV) at the interface of c-Si/SiO_2 or introduce defects e.g. in the µc-SiC:H(n) because it has a lower bandgap than the photon energy [170, 188]. Since the TPC is selective for electrons, only majority carriers should have the ability to transfer into the contact and the minority carriers should be repelled. The small amount of minority carriers which reach the contact layers will recombine. Therefore, increasing the defects in the contact layers by VUV will not significantly increase the recombination rate. Nevertheless, breaking bonds at the c-Si/SiO_2 interface will lead to an increased recombination rate, since it will increase the density of dangling bonds in the area before the charge carriers are separated.

Since the plasma used for ITO deposition of the solar cells in this work also contains oxygen precursors, the influence of the VUV photons on the TPC passivation is investigated. Therefore, symmetrically passivated samples are covered with three filters, which have different transmittance in the UV wavelength range. The transmission data of the filters are summarized in Table 6.3. The first filter (F1) has 50% transmittance at 4.1 eV, while the second filter (F2) has 50% transmittance at 7.5 eV. The third and fourth filter (F3, F4) have a typical transmittance of >50% at 10.2 eV. These filters are used to check which part of the UV light is the

Table 6.3.: *The transmittance (T_λ) data for the used UV filters for T_λ = 50% and 0% with the corresponding photon energies (E_Ph) and wavelength (λ) as found in the material data sheets. For MgF_2 the guaranteed transmittance at 121 nm is >40% and the typical transmittance is ≥55%.*

Filter	thickness d mm	$T_\lambda = 50\%$ E_Ph eV	 λ nm	$T_\lambda = 0\%$ E_Ph eV	 λ nm
F1. Corning EAGLE XG	0.4	4.1	300	4.8	260
F2. Heraeus Herasil	1	7.5	165	8.3	150
F3. MgF_2	5^a	>10.2	<121	n.a.	n.a.
F4. MgF_2	1^b	>10.2	<121	n.a.	n.a.

[a] guaranteed transmission >40% at 121 nm, typical transmission >50%
[b] guaranteed transmission >40% at 121 nm, typical transmission >55%

main cause of degradation. Additionally, they protect the surface against any ion bombardment. The filters cover the samples only partly so that parts of the sample are directly exposed to the plasma. For the first experiment a pure oxygen plasma similar to the one used in Profijt et al. was ignited and the sample was exposed for 15 min [187]. The lifetime corrected PL images before (a) and after plasma exposure (b) are plotted in Figure 6.10. Before the plasma exposure of the sample the effective minority carrier lifetime (τ_eff) was 3.6 ms, measured by PC. After the plasma exposure τ_eff is almost unchanged for the parts covered by filter F1 and F2. In the uncovered part the lifetime drops to τ_eff < 700 µs while in the covered area of filter F3, τ_eff drops to ~900 µs. This result confirms that UV radiation from an oxygen plasma can degrade the passivation of a sample passivated by SiO_2/µc-SiC:H(n). It can also be seen that wavelength of $\lambda < 150$ nm causes this damage, since no significant degradation is detected for the areas covered by filter F1 and F2. The reason why the area covered by filter F3 shows a slightly higher τ_eff compared to the uncovered area is likely due to the non-zero absorption of the filter in the wavelength range <150 nm. Therefore, the uncovered area is exposed to a higher flux density and degrades stronger. This effect was also found by Profijt et al. [187].

However, for sputtering of ITO an argon plasma with only a low concentration of oxygen (1.5 – 5%) is used. It needs to be investigated if this small amount of

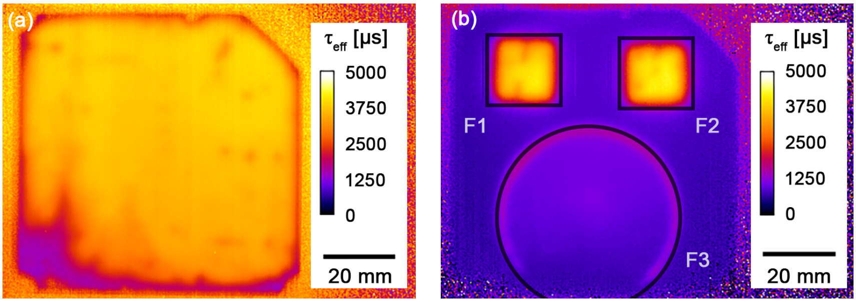

Figure 6.10.: *Lifetime corrected PL image of a symmetrically passivated sample before (a) and after (b) oxygen plasma exposure. Parts of the sample were covered during exposure by three selected UV filters. The images are corrected with τ_{eff} results measured by PC. The color code shows the τ_{eff} in microseconds. This figure was originally published in [9] and was adapted (CC BY 4.0).*

oxygen also leads to a significant VUV emission, which degrades the passivation. Therefore, this experiment is repeated during an ITO deposition. Since the deposition is performed in an upright position, the filters were taped onto the sample. In comparison to the first experiment a smaller and thinner MgF_2 filter (F4) is used, since the filter is ITO coated and can be used only once.

The results of this experiment are displayed in Figure 6.11. The initial τ_{eff} of the sample after passivation was 1.3 ms, measured by PC. After ITO deposition the lifetime in the areas covered by the filters does not show any degradation of τ_{eff}. In the uncovered areas, which were directly exposed to the deposition, τ_{eff} drops below 600 µs. It can therefore be concluded that for high VUV intensities e.g. by a pure oxygen plasma the passivation of the TPC is degraded. However, during the deposition of ITO no degradation due to UV modes can be detected. A possible reason is that the intensity of the VUV mode in the plasma used for sputtering is too low e.g. due to the low oxygen concentration. Nevertheless, the MgF_2 filter reduces the intensity of the VUV light due to its non-zero absorption. The filter typically transmits 55% at 121 nm. Therefore, it cannot be excluded that the VUV intensity is artificially decreased by the filter and is too low to cause degradation while in the uncovered areas the intensity is strong enough to cause this degradation.

Deterioration due to UV exposure and ion bombardment can be prevented

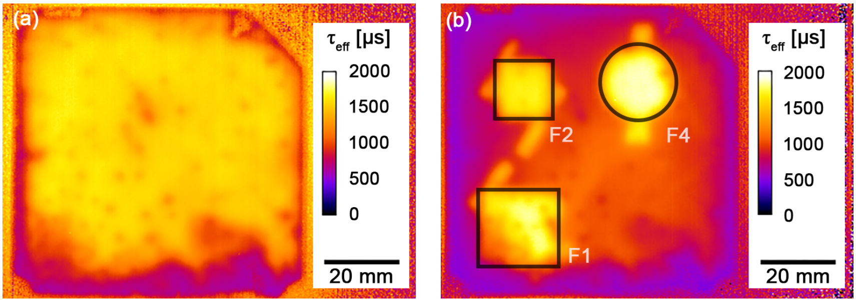

Figure 6.11.: *Lifetime corrected PL image of a solar cell precursor before (a) and after (b) ITO deposition. Parts of the wafer were covered with filters to avoid ion bombardment and to filter the UV light. The images are corrected with the effective minority carrier lifetime (τ_{eff}) results measured by PC. The color code shows τ_{eff} in microseconds. This figure was originally published in [9] and was adapted (CC BY 4.0).*

when using thermal ALD for the processing of the TCO. ALD of e.g. aluminum-doped zinc oxide (AZO) neither involves accelerated particles nor a plasma emitting UV radiation, therefore, the SiO_2/c-Si interface should not be damaged during deposition [189]. To investigate the influence of the ALD deposition on the passivation quality solar cells are fabricated. Therefore, the AZO is deposited through the same kind of shadow mask as used in Figure 6.9 (b). Due to the use of gas precursors for ALD the gas also diffuses underneath the mask. Therefore, the ALD deposition does not reproduce the structure of the mask with high accuracy. The result of the deposition are displayed in Figure 6.12 (a). To see the impact of the deposition on the effective minority carrier lifetime, PL images are taken before and after the deposition and are plotted in Figure 6.13. The initial effective minority carrier lifetime of the sample was $\tau_{\text{eff}} = 2.4$ ms, measured by PC. In comparison to the strong deterioration which was found for sputtered TCO (see Figure 6.9) the ALD deposition does not show any significant degradation in the deposited areas. In Figure 6.13 (b) a slight impact of the sputtered ITO on the rear contact is visible, which is evident due to the slightly lower τ_{eff} within the $2{\times}2$ cm^2 squares. This degradation can be assigned to the ITO on the a-Si:H(i)/a-Si:H(p) rear contact, since the ALD AZO did not show these perfect squared shapes (see Figure 6.13 b). In contrast to sputtering, ALD deposition does not decrease the passivation of the TPC.

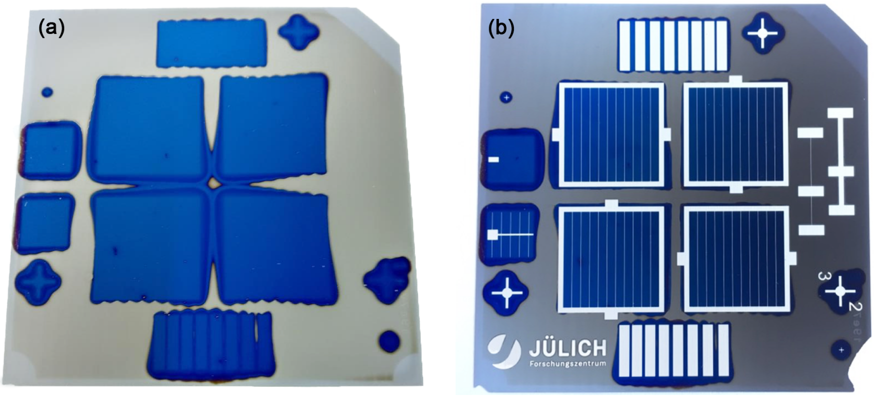

Figure 6.12.: *(a) Wafer after ALD deposition of AZO. (b) Finished solar cell with etched AZO in 1% HCl and and screen printed metallization.*

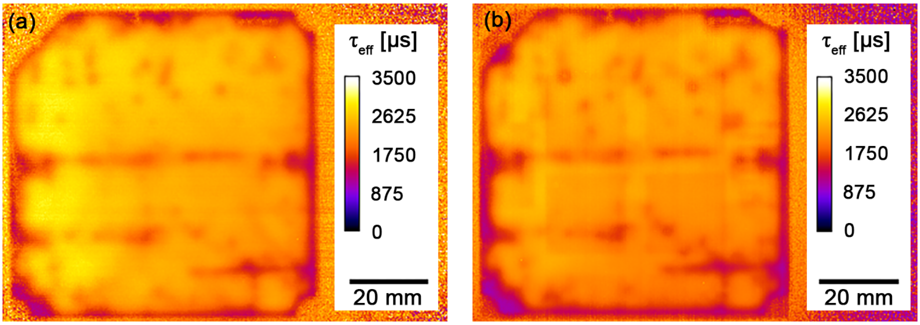

Figure 6.13.: *Lifetime corrected PL image of a solar cell before (a) and after (b) AZO deposition by ALD (a). In (b) the rear contact ITO is also already sputterd. The images are corrected with the effective minority carrier lifetime (τ_{eff}) measured by PC. The color code displays τ_{eff} microseconds. In (b) four squares of slightly reduced lifetime can be seen. These result from the ITO on the rear contact. Due to the use of ALD on the front contact, the mask is not perfectly transferred onto the sample. The effect can be seen in Figure 6.12 (a).*

6.4.2. TCO screening for TPC

To reduce the degradation of the passivation several TCO materials and deposition methods are screened. The goal of this part is to find the best working combination of TCO and TPC. A detailed analysis of all used materials and deposition methods is beyond the scope of this work. The best combination has a high lateral conductive and transparent TCO and negligible degradation of the passivation of the TPC. Additionally, TCO free cells are investigate to study if an additional TCO layer is necessary for a good lateral current flow into the contact fingers. The following TCO and deposition techniques are investigated:

- aluminum-doped zinc oxide (AZO) by atomic layer deposition (ALD),
- tungsten-doped indium oxide (IWO) by reactive plasma deposition (RPD),
- titanium-doped indium oxide (ITiO) by sputtering,
- indium tin oxide (ITO) by sputtering in different systems.

The results for the selected materials and deposition methods are shown in Figure 6.14. Details regarding the depositions can be found in the Appendix A.4. The lowest efficiency of $\eta = 20\%$ is measured for the TCO free solar cells (not shown). The TCO free solar cell suffers from three basic problems: a low J_{sc}, a low V_{oc}, and a low FF. The origin of this low J_{sc} of 37.8 mA/cm^2 is the absence of an ARC. For solar cells with TCO, the TCO also works as an ARC. However, for the TCO free device no additional ARC is added, which results in a high reflection and a low J_{sc}. Furthermore, the precursor cell initially shows a low iV_{oc} of 719 mV, which is approximately 20 mV lower than for the other precursors. This low iV_{oc} then results in a low mean V_{oc} of 708 mV, which means a drop from iV_{oc} to V_{oc} of 11 mV. This drop is comparably low in contrast to the usual drop after sputtering of 32 mV. However, the pFF of the TCO free cells is with >83% the highest pFF throughout this thesis. The reason for that might be that in contrast to the devices with TCO no sputter damage is increasing the recombination. The reason why the iV_{oc} is low and the pFF is high is not understood yet. Nevertheless, the mean FF of 74.5% is low, which is a consequence of a high $R_{\mathrm{s}} > 2\ \Omega\,\mathrm{cm}^2$. The reason for the high series resistance is most likely the high contact resistivity between the Ag and the µc-SiC:H(n). The lateral conductivity, which is otherwise accounted for by the

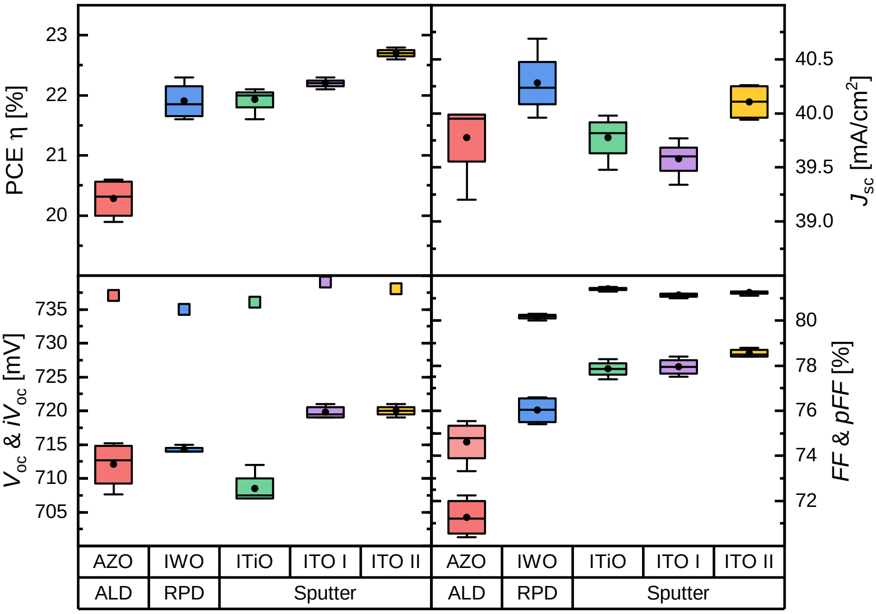

Figure 6.14.: *Device results for solar cells with selected TCOs and deposition methods. With (a) power conversion efficiency, (b) J_{sc}, (c) iV_{oc} (squares) & V_{oc}, and (d) FF & pFF. The AZO, IWO, and ITO were prepared by partner institutes. The colored box in the box plots depicts the values in the 25% - 75% range. The horizontal line within the box shows the median value and the circle shows the mean value.*

ITO, is now supported by the high conductive wafer material, which has a resistivity of 1 Ω cm. Therefore, the lateral conductivity should have no significant effect on the series resistance. It can be concluded that the full potential of this TCO free contact is not yet exploited. By using a precursor with a higher passivation quality as well as a suitable ARC and metallization scheme higher efficiency can be expected. Further investigation on TCO free SHJ solar cells can be found in a preprint version elsewhere [190].

The second lowest efficiency is achieved for the TCO deposited by ALD with $\eta = 20.3\%$. In contrast to sputtering and RPD the pattern of the mask used to define the four 2×2 cm² areas for the solar cells is not transferred perfectly onto the sample, as it can be seen in Figure 6.12 (a). An ALD process uses alternating precursor gases, which react with each other to form the desired layer. These precursor gases flow through the small gap between mask and substrate and create an AZO layer also in between and around these cells. To regain the desired contact area, the excess AZO is etched back using 1% HCl before metallization.

The reason for the low efficiency of the device fabricated with ALD AZO is the low mean V_{oc} of 712 mV and the low mean pFF of 74.6%, which results in a mean FF of 71.3%. The reason for the low pFF can either be a high recombination or a low shunt resistance. However, the IV curve does not show a strong influence of the R_{sh} and no passivation degradation is observed in PL (see Figure 6.13 b). Since the AZO is deposited by ALD, no ion bombardment or UV exposure can reduce the passivation quality of the device as it is the case for sputter depositions. Furthermore, the initial passivation of the precursor was high as it can be seen from the iV_{oc} of 737 mV. The reason for the low V_{oc} and pFF is not understood yet.

Another deposition method, which is known to reduce the ion bombardment compared to sputtering, is RPD [177,191,192]. For RPD deposition particle energies are usually lower than 40 eV [193] while for sputtering particle energies of 100 eV have been measured, originating for back-scattered Ar ions [194]. The binding energy between atoms is typically several eV, thus, particle energies higher than 5 eV can break these bonds [195]. Smets et al. suggest different processes happening due to ion bombardment in a silicon network at different ion energies [196]. At ~7 eV the ions can be incorporated in the silicon network as interstitials, for >18 eV the surface atoms and >40 eV bulk atoms can be displaced [196]. For ion energies >50 eV sputtering of the surface atom can happen [196]. However, Illiberi et al. found that for a-Si:H passivated c-Si the passivation quality is independent of the energy of impinging ions [183]. They found that the influencing factor during ion bombardment is the ion flux density.

For the solar cells with IWO deposited by RPD no improvement in V_{oc} is found in comparison to the samples with sputtered TCO. The reason for the deterioration of the passivation is not fully understood yet. A systematical study of the RPD deposition parameters is necessary to reveal the origin of the deterioration. The mean V_{oc} is 714 mV, which is 21 mV lower than the iV_{oc}. Due to a low pFF and a mean R_{s} of 0.9 $\Omega\,\text{cm}^2$ the mean FF is 76%. Nevertheless, the mean J_{sc} with

40.3 mA/cm^2 is the highest in this series. This high J_{sc} implicates that the IWO is the most transparent film in this series. Meng et al. found that the IWO in their experiment shows the highest refractive index, the lowest extinction coefficient and the lowest free electron concentration compared to ITO and ITiO films [193]. This superior optical parameters can explain the high transparency of IWO. The solar cells with IWO had a mean efficiency of $\eta = 21.9\%$ in this experiment.

Finally, sputtering is used for the deposition of ITiO and ITO films. For the deposition of the ITO films two different deposition systems and deposition conditions are used. Despite the differences in deposition an equal mean V_{oc} of 720 mV and a iV_{oc} to V_{oc} drop of 19 mV is measured, while sputtering of ITiO results in a V_{oc} of 709 mV and a drop of 27 mV. Due to the highest mean FF of 78.6% and J_{sc} of 40.1 mA/cm^2 of the cells fabricated with ITO II, these cells show the highest mean efficiency of $\eta = 22.7\%$ in this experiment . It can be concluded that neither TCO free nor nominally less harmful deposition methods e.g. ALD and RPD result in a superior V_{oc}. However, the mechanisms leading to a reduced V_{oc} might depend on the used deposition methods. The best efficiency was achieved by ITO sputtering.

6.4.3. Influence of ITO deposition conditions on solar cell parameters

To further investigate the influences of the sputter parameters on the performance of the solar cells the deposition power (P_{dep}) and deposition pressure (p_{dep}) are changed in the following experiment. As discussed before, a higher sputter pressure results in a lower energy of the sputtered ions reaching the sample surface. A lower sputter power results in a lower flux density of the secondary ions. Furthermore, decreasing the sputter pressure and power also decreases the intensity of the high energy UV at 130 nm as found by Profijt et al. [187].

To be able to compare the results of the changed deposition power and pressure, reference solar cell is investigated. As a reference cell the best cell from the DoE experiment is chosen. The deposition of the reference ITO is performed at $p_{\text{dep}} = 6$ µbar and $P_{\text{dep}} = 5$ kW. In this experiment three sputter powers $P_{\text{dep}} = 0.5$ kW, 3.35 kW, and 6.2 kW as well as three sputter pressures $p_{\text{dep}} = 10$ µbar, 15 µbar, and 20 µbar are investigated. The influence of the sputter pressure and power on the solar cell parameters can be seen in Figure 6.15. The results are obtained following the conventional annealing after screen printing of 40 min at 190 °C in an oven. No further curing steps are applied at this time. Details about the deposition parameters can be found in the Appendix A.4.

The results show that two deposition conditions (10 µbar, 0.5 kW and 15 µbar, 3.35 kW) of the ITO reach significantly higher V_{oc} values compared to the reference cell (gray dashed line). The highest V_{oc} in this experiment was measured for 5 µbar, 3.35 kW with 719 mV. However the mean results of the V_{oc} are only improved slightly compared to the reference cell. The lowest V_{oc} values are found for the deposition conditions of 20 µbar, 0.5 kW which are expected to have the lowest degradation by ion bombardment and UV damage. However, the sheet resistance of the ITO deposit at 20 µbar, 0.5 kW is very high (>4000 Ω/sq) resulting in a high R_{s}, which then results in the low mean FF of 74.2%. This low FF is the reason for the lower mean efficiency of $\eta = 20.8\%$.

For all samples deposited at 6.2 kW the V_{oc} is almost equal to the reference, which is deposited at 5 kW. This leads to the conclusion that high deposition powers do not lead to high V_{oc}. The reason for that might be the high ion flux density, which deteriorates the passivation or the high energy of the Ar ions reflected from the target. Regarding the J_{sc} the mean values for all ITO layers are equal besides the ITO deposited at 10 µbar, 6.2 kW. Here, the J_{sc} is significantly reduced. It was found that the ITO deposited at 10 µbar, 6.2 kW has the lowest sheet resistance of 136 Ω/sq. This low sheet resistance might be a reason for an increase of free carriers in the ITO, which then leads to an increased free carrier absorption and a decreased J_{sc}. The solar cells with ITO deposited at 10 µbar, 0.5 kW and 15 µbar, 3.35 kW seem to have a good balance between moderate ion flux densities, moderate ion energies, and moderate sheet resistances. However, the complete mechanism resulting in less sputter damage and improved V_{oc} is not fully understood yet.

To reduce the degradation damage which could not be prevented by sputtering, the samples are cured on a hot plate. For contacts prepared by SiO_2/poly-Si and a-Si:H contacts the sputter damage is found to be reversible by curing at 300 °C – 400 °C [57, 58] and 190 °C – 300 °C [181, 182], respectively. The rear contact of the solar cells consists of temperature sensitive a-Si:H(i)/a-Si:H(p) layers. For curing temperatures higher than 250 °C hydrogen starts to effuse from the a-Si:H, which reduces the passivation quality and thereby the V_{oc} [197,198]. Therefore, the curing of the cells is performed in two steps at 220 °C for $10+10$ min. For this experiment the best four solar cells from the reference batch ($p_{\mathrm{dep}} = 6$ µbar, $P_{\mathrm{dep}} = 5$ kW) as well as from the 10 µbar, 0.5 kW and 15 µbar, 3.35 kW have been investigated.

The results of the JV-measurements for selected curing times are displayed in Figure 6.16. It can be seen that the V_{oc} of the reference solar cells does not improve upon curing. Especially, the V_{oc} is not improving for the reference cells unlike for the cells with optimized ITO sputter conditions. For the cells with ITO sputtered at 10 µbar, 0.5 kW the mean V_{oc} increases from 712 mV to 718 mV. The V_{oc} for the cells with ITO deposited at 15 µbar, 3.35 kW increases from 717 mV to 721 mV. Simultaneously, also the J_{sc} increases by 0.5 mA/cm^2 and the FF improves up to 0.5%$_{\mathrm{abs}}$ due to the curing of the cells with improved sputtering conditions. These improvements due to curing lead to an improved mean power conversion efficiency from 21.7% to 22.5% for the cell with ITO deposited with 10 µbar, 0.5 kW and from 22.4% to 22.9% for the cell with ITO deposited with 15 µbar, 3.35 kW. The best solar cell in this experiment had an efficiency of $\eta = 23\%$ ($J_{\mathrm{sc}} = 40.5$ mA/cm^2, $V_{\mathrm{oc}} = 722$ mV, $FF = 78.6\%$, and $R_{\mathrm{s}} = 0.59\ \Omega\,\mathrm{cm}^2$).

The regular JV measurement of the four cells on one wafer (see Figure 6.12 b) was performed in a way that all four rear contacts of the solar cells were contacted even though only one cell was under test. However, it can be shown that by contacting only the tested cell, higher V_{oc} and FF values are measured. For our best solar cell a FF increase of $\sim$2.2%$_{\mathrm{abs}}$ and a V_{oc} increase of 4 mV is evident. The J_{sc} is unaffected by the isolation of the back contacts.

The IV-measurements of the four best solar cells on one wafer are independently certified by CalTeC at the Institute for Solar Energy Research in Hamelin (ISFH) and can be seen in the Appendix Figure A.1. To isolate the rear contacts on a conductive chuck an adhesion foil is used for certification. The best solar cell is then certified with $\eta = 23.79\%$, $J_{\mathrm{sc}} = 40.3$ mA/cm^2, $V_{\mathrm{oc}} = 725$ mV, $FF = 81.3\%$. Measuring with isolated rear contacts is a valid method, since industrial full-size solar cells also contain only one rear side contact. Furthermore, when comparing solar cells processed in the same batches on industrial size wafers and 2×2 cm^2 solar cells on a 78×78 cm^2 wafer, the small solar cells always shows a significantly lower V_{oc} and FF when measured without rear contact isolation. The reduced V_{oc} and FF when all rear contacts are contacted seem to be a measurement artifact.

Curing of the samples can improve the efficiency of solar cells in various ways. One way is the reorganization of hydrogen [199]. Due to an increased substrate temperature the hydrogen at the $\mathrm{SiO_2}$/c-Si interface can be redistributed. Additionally, hydrogen from the µc-SiC:H(n) layer may diffuse to the interface. This hydrogen can then re-passivate open dangling bonds, which e.g. result from damage due to sputtering. This diffusion to the interface might be supported by the ITO, since ITO is a diffusion barrier for hydrogen and thus prevents the out-diffusion of hydrogen [200]. The ability to prevent out-diffusion of hydrogen might dependent on the structure of the ITO and its deposition parameters. This might explain why the reference ITO does not show an improvement in V_{oc} due to curing. Further studies, beyond the scope of this work, are currently ongoing.

Curing of the solar cell might also reduce the contact resistivity. Curing can lead to a higher conductivity of the metal electrodes and of the ITO layer. For the best solar cell, the sheet resistance of the ITO decreased by ∼70 Ω/sq to 202 Ω/sq due to curing. For the best solar cell the series resistance decreased by 0.1 $\Omega\,\mathrm{cm}^2$. However, the contact resistivity of Ag/ITO is usually in the $\mu\Omega\,\mathrm{cm}^2$ range [201]. Therefore, it is more likely that the contact resistivity is reduced at the ITO/TPC or the TPC/c-Si interfaces since they have a larger impact on the contact resistivity.

It can be summarized that sputtering of ITO can cause a deterioration of the passivation. It was found that UV radiation from a pure oxygen plasma has the ability to reduce the passivation of the TPC drastically. However, during the real sputter experiment with only a small oxygen concentration in the plasma no degradation due to UV radiation was found. Therefore, the most likely reason for sputter degradation is the effect of ion bombardment. This idea was stressed by the finding that depositing TCO with an ion bombardment free method like ALD results in no degradation of the passivation as shown by PL measurement.

Fabricating solar cells with TCO deposited by ALD did not show an improvement in V_{oc}. It was also found that deposition by RPD, which should also reduce ion bombardment, V_{oc} did not improve compared to the sputtered TCOs on solar cells. Furthermore, it was found that by decreasing the power and increasing the pressure during sputter deposition the V_{oc} was increased compared to the reference deposition conditions. The V_{oc} was then further increased by curing on a hot plate at 220 °C for 20 min, which cures the residual damage. This improvement due to annealing was only found for the optimized ITO deposition conditions and not for the reference deposition.

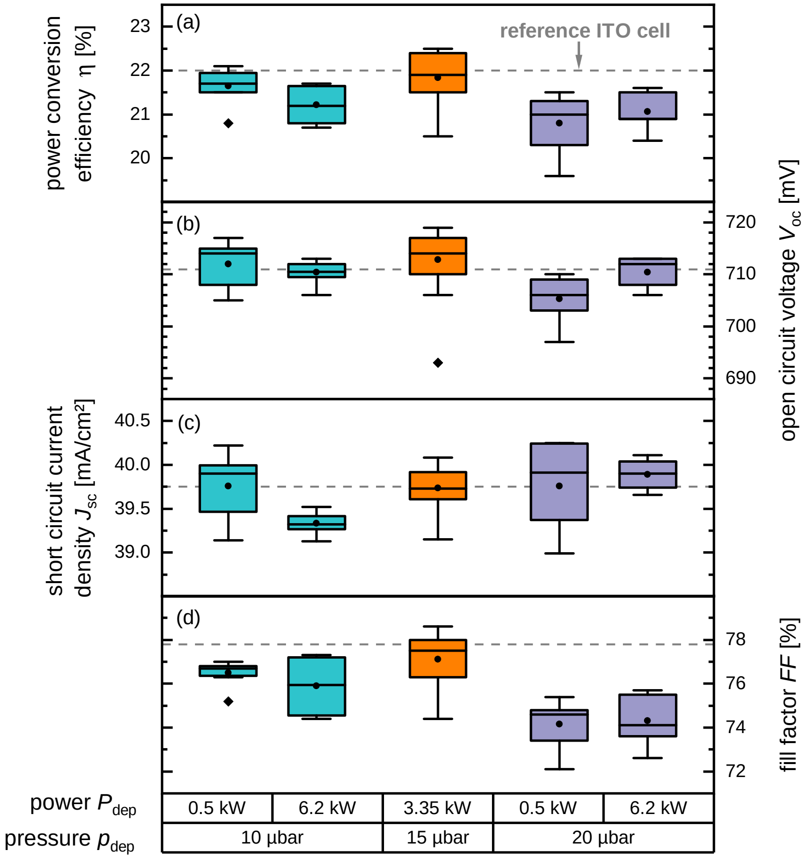

Figure 6.15.: *Sputter parameter experiment on solar cells to reduce sputter damage. (a) power conversion efficiency η, (b) open circuit voltage V_{oc}, (c) short circuit current density J_{sc}, and (d) fill factor FF as a function of the deposition the sputter pressure p_{dep} and the sputter power P_{dep} after initial annealing at 190 °C. The gray dashed line marks the results of the best cell from the double layer stack development experiment using the reference ITO deposited with 6 µbar and 5 kW. The colored box in the box plots depicts the values in the 25% – 75% range. The horizontal line within the box shows the median value and the circle shows the mean value. Diamonds represent outlier values. This figure was originally published in [9] and was adapted (CC BY 4.0).*

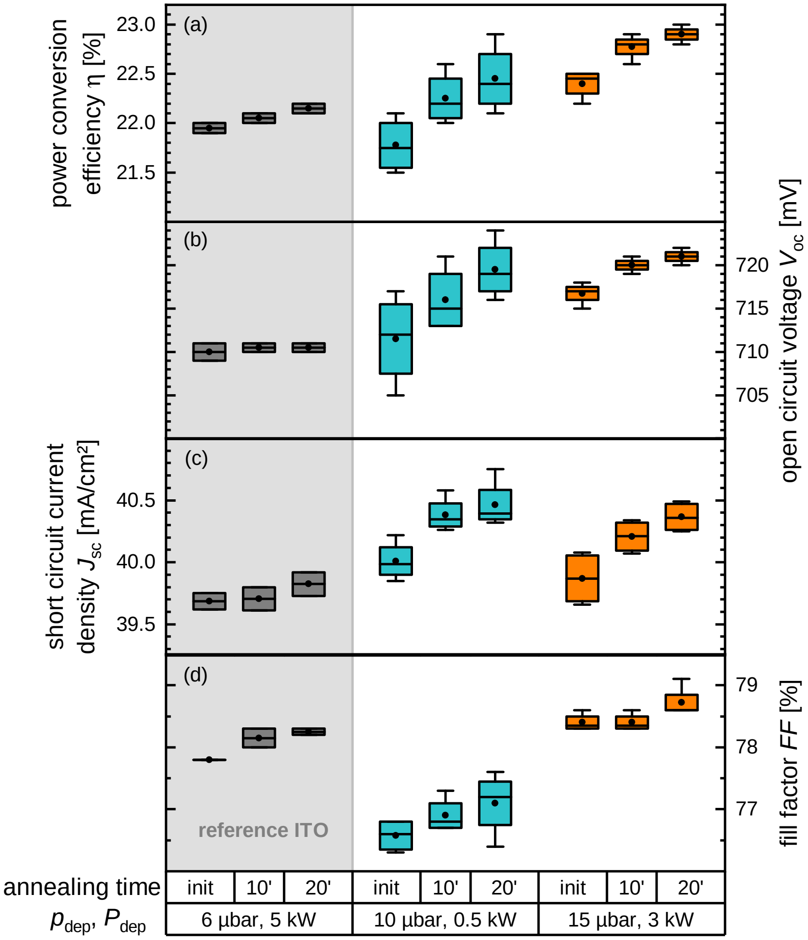

Figure 6.16.: *Curing series of solar cells on hot plate to reduce sputter damage. (a) power conversion efficiency (η), (b) open circuit voltage (V_{oc}), (c) short circuit current density (J_{sc}), and (d) fill factor (FF) as a function of the curing time after 40 min initial annealing at 190 °C in oven (init), and curing for 10 min, and 20 min at 220 °C on a hot plate. The colored box in the box plots depicts the values in the 25% – 75% range. The horizontal line within the box shows the median value and the circle shows the mean value. This figure was originally published in [9] and was adapted (CC BY 4.0).*

6.5. Optical improvement

Using µc-SiC:H(n) as a front contact has the natural advantage of the wide optical bandgap of the material (2.3 – 2.9 eV) [144], which makes it more transparent than state of the art passivating contacts e.g. a-Si:H (1.7 eV) [202] or poly-Si (1.1 eV) [53]. An additional advantage of the µc-SiC:H(n) as a front contact for silicon solar cells compared to a-Si:H and poly-Si contacts is the well matching refractive index grating. While silicon has a refractive index in the wavelength range of 300 nm – 900 nm between 3.6 – 6.9 [203] the refractive index for µc-SiC:H(n) is 2.6 – 3 [180], for a-Si:H it is 3.1 – 4.9 [204], and for poly-Si it is similar to c-Si [205]. Thus, using µc-SiC:H(n) instead of a-Si:H or poly-Si layer on the sun facing side of the solar cell the reflection of the front contact should be reduced. Pomaska et al. found that the reflection of the c-Si/SiO$_2$/µc-SiC:H(n) contact can be further reduced by adding an MgF$_2$ layer on top of the µc-SiC:H(n) [180]. MgF$_2$ has an refractive index of 1.4 over the entire measured wavelength range and no additional absorption. This result was obtained for interdigitated back contact (IBC) solar cells without a TCO layer in between. For two side contacted solar cells as fabricated in this work a TCO layer is necessary to achieve a high power conversion efficiency. To investigate if a MgF$_2$ ARC can decrease the reflection of the front side for TPC with ITO, optical simulations using the software OPAL2 [206] are done.

The results of the optical simulation is shown in Figure 6.17 (a). It can be seen that by adding a 125 nm thick MgF$_2$ layer the reflection of the front contact can be significantly reduced. Due to the result of the OPAL2 simulation an 125 nm thick MgF$_2$ layer is added by electron beam evaporation on top of the best solar cell from the TCO study in Section 6.4. This cell was previously independently certified to have a J_{sc} of 40.3 mA/cm^2. By adding the ARC the J_{sc} was increased to 40.9 mA/cm^2, which was also independently certified by ISFH CalTeC (see Figure A.2 b). The results of the reflectance and EQE measurements can be found in Figure 6.17 (a) and (b), respectively. It should be noted that the reflectance is measured on the aperture area of the solar cell, thus, includes reflectance of the active area and the metal fingers while the simulation is performed only on the active area. Due to the reflectance of the metal fingers the measured data has an offset to higher reflectances.

It can be seen that the results of the simulation of the reflectance can be confirmed by the measurements. The reflectance peak at 380 nm can be decreased from 14% to 8% due to the ARC (see Figure 6.17 a). The reflectance is decreased in the short wavelength range between 350 nm – 600 nm and in the long wavelength range >850 nm. This decrease in reflectance increases the EQE in both short and long wavelength range as it can be seen in Figure 6.17 (b). Due to the reduction of reflectance the J_{sc} is increased by 0.6 mA/cm^2. However, it is found that due to the e-beam evaporation of the MgF_2 the passivation quality, thus, the V_{oc} is decreased. This deterioration of the passivation can be cured on a 230 °C hot plate for 20 min. This solar cell is again independently certified and results in $\eta = 23.99\%$, $J_{\text{sc}} = 40.9$ mA/cm^2, $V_{\text{oc}} = 725.5$ mV, $FF = 80.9\%$. The graphs of the certifications can be found in the Appendix Figure A.2.

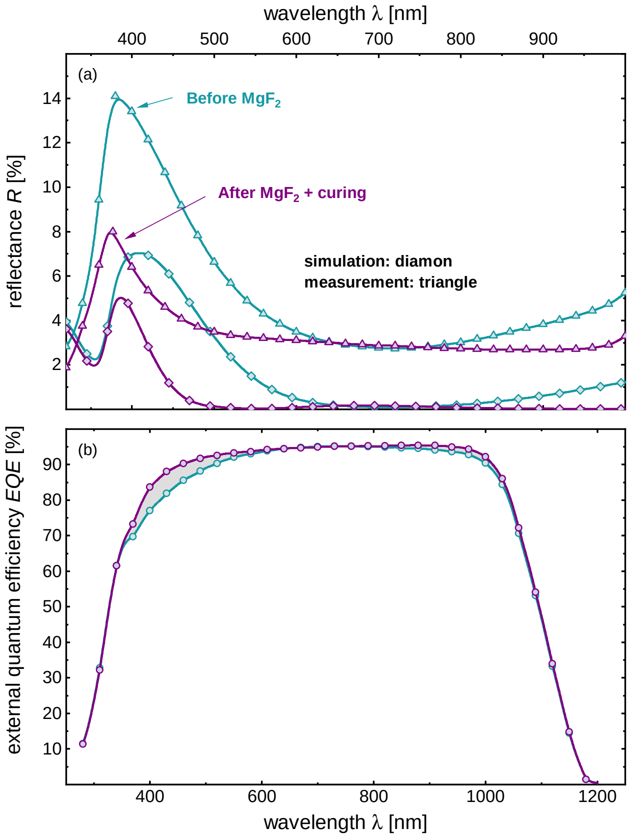

Figure 6.17.: *Optical and electro-optical effects of an MgF_2 ARC on TPC solar cells. (a) Simulated (diamonds) and measured (triangles) reflectance for the front side contact of c-Si/SiO_2/µc-SiC:H(n)/ITO with and without MgF_2 as a function of the wavelength. (b) External quantum efficiency (EQE) with and without MgF_2 ARC as a function of the wavelength. MgF_2 reduces the reflection in the long and in the short wavelength range, which improves the EQE in these regions and results in a higher J_{sc}. Data in this figure was originally published in [9] (CC BY 4.0) and adapted.*

7. Conclusion & Outlook

The goal of this thesis was to develop a transparent passivating contact (TPC) for the front side of c-Si solar cells. This front contact must fulfill three basic requirements. It needs to be (i) transparent, (ii) passivating and (iii) conductive. Wide bandgap marterials, which minimize parasitic absorption of the incident sunlight, are necessary to achieve a high transparency of the contact. As studied before by Pomaska in his PhD thesis, a suitable material with high bandgap is n-type hydrogenated microcrystalline silicon carbide (µc-SiC:H(n)) [10], which was chosen for this work. However, as also found by Pomaska, the sole µc-SiC:H(n) layer is not providing a sufficient surface passivation. Thus, a SiO_2 layer is needed in between the c-Si and the µc-SiC:H(n) as a buffer [10].

In the Chapter «**Wet-chemically grown SiO_2 Tunnel Oxides**» the SiO_2 layer was optimized to achieve a high passivation quality and a low contact resistivity. Therefore, SiO_2 layers are grown using selected wet-chemical oxidation techniques. It was found that a minimum oxide thickness of 1 nm is required to achieve high passivation qualities. However, for oxide thicknesses larger than 1 nm the contact resistivity is increasing exponentially. Oxidation in SC-2 solution was found to create an oxide with a thickness of 0.5 nm, which is not stable enough to achieve a high passivation quality and a low contact resistivity. Oxidation in HNO_3 resulted in an oxide thickness of 1.3 nm, which allowed to achieve a sufficient passivation quality with a comparably high contact resistivity. The best trade-off between passivation and contact resistivity was found for the 1 nm thick SiO_2 produced with piranha oxide. Furthermore, it was found that the filament temperature of the hot wire during HWCVD deposition of the µc-SiC:H(n) also has a strong impact on the passivation quality. The highest passivation quality was achieved at a filament temperature of 1800 °C, resulting in the highest iV_{oc} of 728 mV for SiO_2

prepared in piranha solution. The contact resistivity is decreasing with increasing filament temperature for a given oxide thickness. The lowest contact resistivity was measured with $\rho_c = 18\ \mathrm{m\Omega\,cm^2}$ at $T_f = 1970$ °C.

In the Chapter «**Material and contact properties of µc-SiC:H(n)**» the material properties of µc-SiC:H(n) and the contact properties of the SiO_2/ µc-SiC:H(n) stack were investigated. The electrical conductivity of the µc-SiC:H(n) was increased by 12 orders of magnitude by increasing the filament temperature during HWCVD from 1630 °C to 2100 °C. This increase can partly be explained by the increase in nitrogen doping concentration, which was found to have a doping efficiency of one for filament temperatures higher than 1850 °C. Additionally, it was found that the crystallite size of the µc-SiC:H(n) is increasing with increased filament temperature, which can lead to an increased free carrier concentration.

Increasing the filament temperature from 1660 °C to 1900 °C also increased the optical bandgap of the µc-SiC:H(n). Additionally, it was found that due to the increase of free carriers with increased filament temperature, the sub-bandgap absorption also increases. A balance between high optical bandgap and low sub-bandgap absorption was found for µc-SiC:H(n) deposited at 1800 °C. Here, the parasitic absorption of a 20 nm thick µc-SiC:H(n) film was calculated to result in a loss in short circuit current density of $0.31\ \mathrm{mA/cm^2}$.

As already found in the SiO_2 development, the passivation quality of the TPC strongly depends on the filament temperature during HWCVD. For filament temperatures higher than 1850 °C the passivation quality starts to degenerate. It was found that by increasing the filament temperature the hydrogen concentration in the material is decreased. This decrease in hydrogen concentration might be correlated to the larger crystallite size for increased filament temperature since hydrogen predominantly located at the grain boundaries. A lower hydrogen concentration in the layer can lead to less diffusion of hydrogen to the c-Si/SiO_2 interface, where it passivates dangling bonds. However, high filament temperatures are necessary to achieve low contact resistivities of the TPC to enable a sufficient flow of the generated current in the solar cell. Both, a high passivation quality and a low contact resistivity were achieved by using a double layer stack of µc-SiC:H(n). The first layer, which is in contact with the SiO_2, provides a hydrogen reservoir to passivate

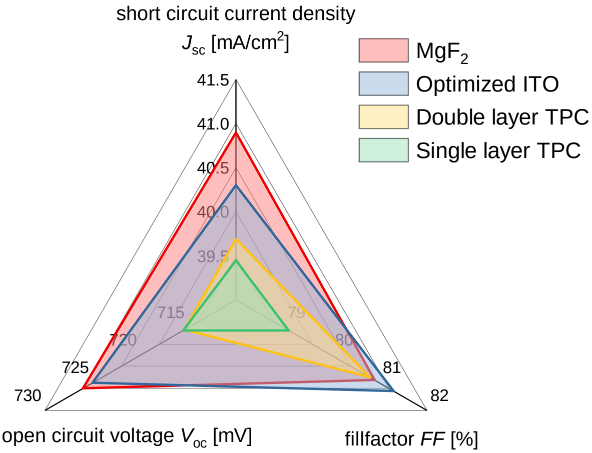

Figure 7.1.: *Development of the solar cell parameters J_{sc}, V_{oc}, and FF during for single layer (η = 22.3%), double layer stack (η = 22.9%), ITO optimization (η = 23.8%), and MgF$_2$ ARC (η = 24%). This figure was originally published in [9] and was adapted (CC BY 4.0).*

dangling bonds and is deposited at lower filament temperatures. The second layer is deposited at elevated temperatures resulting in a high electrical conductivity of the µc-SiC:H(n), which enables low contact resistivities. With the double layer stack it was possible to achieve an exceptionally high passivation quality with iV_{oc} of 740 mV and $J_0 = 2$ fA/cm^2 as well as a contact resistivity of 38 mΩ cm^2.

The aim of the Chapter «**Solar cell development with TPC front side**» was to optimize the TPC in order to achieve high power conversion efficiencies of the solar cells. In a first step selected oxidation solutions for forming the SiO$_2$ were investigated on device level. It was shown that oxidation in SC-2 can neither provide a sufficiently high V_{oc} nor a sufficiently low R_s. Thus, it is not suitable for achieving high solar cell efficiencies. For SiO$_2$ prepared by HNO$_3$ and piranha solution the achievable series resistances were comparable. However, the efficiency is higher for solar cells prepared using piranha solution due to a higher V_{oc}. The subsequent experiments were all performed using SiO$_2$ prepared in piranha solution.

In a second step the filament temperature during HWCVD of the µc-SiC:H(n) was varied. It was found that the V_{oc} is decreased with decreasing T_f in the same way as the iV_{oc} is decreasing. Furthermore, it was found that the fill factor is not improving with increased T_{f} even though the electrical conductivity of the material is strongly increasing. Using the double layer stack of µc-SiC:H(n), a high FF was achieved while a high V_{oc} could be maintained. It was found that the R_{s} and the FF are mainly dominated by the thickness of the first layer. Reducing the thickness of the first µc-SiC:H(n) layer significantly increased the FF. A quantitative version of the «magic triangle» is used to visualize the optimization process throughout this Chapter. The improvement from single layer (green) to double layer µc-SiC:H(n) (yellow) in the FF can be seen in Figure 7.1. However, using a double layer stack of µc-SiC:H(n) did not improve the V_{oc} of the solar cells even though the iV_{oc} was maintained.

The reason for the drop from iV_{oc} to V_{oc} was found to be the degradation due to sputtering of the TCO. Further experiments revealed that UV damage originating from the sputtering plasma is likely not the reason for the degradation of TPC passivation. Thus, the ion bombardment of the sample during sputtering has a significant influence on the degradation. The sputter damage was reduced by increasing the sputter pressure and decreasing the sputter power, which results in a lower particle energy and a lower particle flux to the substrate, respectively. The gap between iV_{oc} and V_{oc} was decreased by optimizing the deposition parameters. Furthermore, it was possible to anneal remaining sputter damage, which was not the case for ITO deposited at lower power and higher pressure. Due to these improvements the V_{oc} was increased by 10 mV as compared to the best solar cell from the double layer stack experiments (see Figure 7.1, blue).

Finally, $\mathrm{MgF_2}$ was deposited on the front side on top of the µc-SiC:H(n) to reduce the reflection of the TPC. This additional ARC improved the J_{sc} by 0.6 mA/cm^2 as compared to the best solar cell with optimized ITO. As a result the best solar cell in this work was independently certified by CalTeC ISFH with η = 23.99%, J_{sc} = 40.9 mA/cm^2, V_{oc} = 725.5 mV, FF = 80.9% (see Figure 7.1, red). These results stress the high potential for the $\mathrm{SiO_2}$/µc-SiC:H(n) contact as a front contact platform for silicon solar cells. The process flow is very lean and solely based on low temperature fabrication due only three basic processing steps: 1. $\mathrm{SiO_2}$ oxidation, 2. µc-SiC:H(n) deposition, and 3. TCO sputtering.

Outlook On the basis of this work several experiments might be of interest to further optimize the contact properties as well as increasing the maturity for possible industrial applications. Using wet-chemical oxidation with ozone might improve the SiO_2 properties and reduce the environmental impact of chemical waste. Moldovan et al. could show a high stoichiometry and an improved iV_{oc} for SiO_2/poly-Si contacts [81] using ozone oxidation. A reduction to two processing steps might be achievable by oxidizing the Si surface with HWCVD [107], which would make it possible to combine oxidation and µc-SiC:H(n) formation.

Investigations of the role of hydrogen are necessary to further understand the passivation mechanism of the SiO_2/µc-SiC:H(n) stack. By using deuterium instead of hydrogen as a dilution precursor during HWCVD, ToF-SIMS measurements could reveal if the deuterium is diffusing to the c-Si/SiO_2 interface. It should be investigated if the hydrogen concentration at the c-Si/SiO_2 interface depends on the filament temperature of the HWCVD, thus, confirming that a lower hydrogen reservoir in the µc-SiC:H(n) contributes to a lower passivation of silicon dangling bonds. Furthermore, effusion measurements of hydrogen or deuterium could reveal at which temperature hydrogen/ deuterium effusion is happening and if it can be capped e.g. by µc-SiC:H(n), TCO layers or MgF_2. The sample temperature can be kept constant by decreasing the substrate heater temperature at increased T_f, to reveal if hydrogen effusion is happening due to an increased substrate temperature by stronger wire radiation.

Further fine tuning of deposition conditions (e.g. MMS flow rate, deposition pressure, wire-substrate distance) for the µc-SiC:H(n) double layer stack will improve the FF of the device as long as it is not limited by the rear side contact. The V_{oc} of the device might be further increased by using deposition methods for the TCO, which are less harmful to the passivation of the TPC, for example ALD or RPD with improved deposition conditions. The J_{sc} of the device can be increased by substituting the ITO using a more transparent TCO, which have a high electron mobility. Possible options can be IWO [193, 207–209] as shown in Figure 6.14 (b) or hydrogen-doped indium oxide (IOH) due to its high electron mobility [210, 211]. IOH might be advantageous because it can be either sputtered or deposited by ALD [212]. Further improvements can be expected when using a TCO-free front contact with a customized metallization scheme and a suitable ARC. The results in this work showed a very high pFF (see Figure 6.14 d) for TCO-free cells, which were mainly limited by the low iV_{oc} of the precursor samples.

Due to its superior optical properties, its high passivation quality, its low contact resistivity and its lean process flow, the SiO_2/µc-SiC:H(n) contact can be utilized as a platform for different solar cell concepts. Possible contact concepts beyond the presented SHJ rear contact might be a p-type poly-Si as a rear emitter [59, 60, 213] or using the TPC as a front emitter on p-type crystalline silicon. A very innovative concept for bifacial solar cells would be the used of an n-type silicon carbide on the front side and a p-type silicon carbide on the rear side of the solar cell. Silicon carbide can be p-type doped using e.g. aluminum as an acceptor and also shows high transparency as well as high electrical conductivity [128, 149, 214, 215]. In combination with a TCO free front side this device would not only be highly transparent on front and rear contact but could also be mostly deposited by HWCVD. This device is sketched in Figure 7.2.

The next steps to achieve a more industrial relevant process will be the demonstration of a TPC solar cell on full size 6 inch wafer. Furthermore, the deposition time of the µc-SiC:H(n) by HWCVD needs to be decreased while maintaining a high quality of the material to enable an industry relevant process. Selected wire materials for the hot wires could be investigated to see their lifetime and the dependency of the µc-SiC:H(n) quality on the material. Cleaning an preconditioning routines of the deposition chamber need to be established for a close to industrial production.

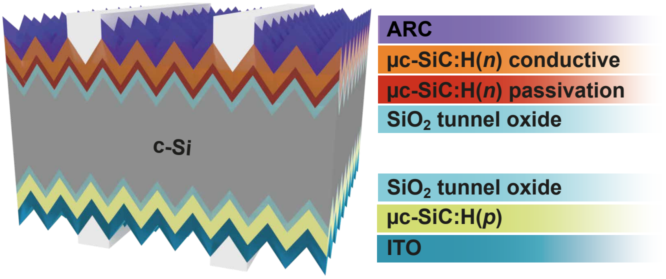

Figure 7.2.: *Bifacial solar cell concept using an n-type TPC as a front contact and a p-type TPC as a rear contact to maximize the solar cell current.*

A. Experimental Details

In this Chapter a detailed overview of the deposition parameters for the solar cell experiments is given. In the beginning all wafers are cleaned and oxidized as described in Section 3.1. The µc-SiC:H(n) layers are deposited by HWCVD. As a rear contact of the solar cells a stack of a-Si:H(i)/a-Si:H(p) is deposited by PECVD. Following the deposition of the rear side ITO is sputtered on the front (n) and on the rear (p) if not stated otherwise. Finally the metal contacts are either evaporated or screen printed on the solar cells.

A.1. Solar Cells using selected SiO_2

The used dst wafers have a base resistivity of $1 - 5\ \Omega\,\mathrm{cm}^2$. The front side fingers are evaporated with 2 µm while the rear side contact is evaporated on full area with a thickness of 700 nm.

Table A.1.: *Deposition details for solar cell series with varied SiO_2 oxidation method. Parameters are given for HWCVD of µc-SiC:H(n), PECVD of a-Si:H(i)/a-Si:H(p), and PVD of ITO. Differences of ITO deposition on front (n) and rear (p) side are separated by a slash.*

HWCVD			PECVD (i/p)			PVD (n/p)		
System		p-HW	System		Maria	System		Lissy
T_H	°C	250	T_H	°C	200	T_H	°C	250
p_{dep}	mbar	0.75	$d_{a\text{-}Si}$	nm	6/9	p_{dep}	µbar	3
$d_{f\text{-}s}$	mm	57	P_{dep}	W	50/90	P_{dep}	kW	5
H_2 flow	sccm	94	H_2 flow	sccm	650/500	Ar flow	sccm	90/197
MMS flow	sccm	6	SiH_4 flow	sccm	145/50	O_2 flow	sccm	5/3
N_2 flow	sccm	30	TMB flow	sccm	0/100			

A.2. Single layer TPC solar cells

The used dst wafers have a base resistivity of 1 $\Omega\,cm^2$. The tunnel SiO_2 is produced in 60 °C piranha solution for 10 min. The metal contacts are realized by screen printing of fingers and a busbar on the font side and by full area metallization of the rear side. Afterwards, the solar cells are annealed at 190 °C for 70 min in ambient air.

Table A.2.: *Deposition details for the solar cell series using a single layer µc-SiC:H(n). Parameters are given for HWCVD of µc-SiC:H(n), PECVD of a-Si:H(i)/a-Si:H(p), and PVD of ITO. Differences of ITO deposition on front (n) and rear (p) side are separated by a slash.*

HWCVD			PECVD (i/p)			PVD (n/p)		
System		p-HW	System		Maria	System		Lissy
T_H	°C	250	T_H	°C	200	T_H	°C	250
p_{dep}	mbar	0.75	$d_{a\text{-}Si}$	nm	6/7.5	p_{dep}	µbar	6/3
$d_{f\text{-}s}$	mm	57	P_{dep}	W	50/90	P_{Gen}	kW	5
H_2 flow	sccm	94	H_2 flow	sccm	650/500	Ar flow	sccm	197/90
MMS flow	sccm	6	SiH_4 flow	sccm	145/50	O_2 flow	sccm	3/5
N_2 flow	sccm	30	TMB flow	sccm	0/100			

A.3. Double layer stack µc-SiC:H(*n*)

Conductive layer variation For the following experiments a double layer stack of µc-SiC:H(n) is used. It consists of a thin µc-SiC:H(n) layer in contact with the SiO_2 which is called the passivation layer followed by a thicker layer which is called the conductive layer (see Figure 6.5). In this experiment filament temperature and the thickness of the passivation layer are fixed at $T_{\mathrm{f}}^{\mathrm{pass}} = 1750$ °C and $d_{\mathrm{SiC}}^{\mathrm{pass}} = 9$ nm. The filament temperature of the conductive layer is varied between $T_{\mathrm{f}}^{\mathrm{cond}} = 1895$ °C – 2010 °C. The other HWCVD deposition parameters, PECVD of the a-Si:H(i/p), and PVD of the ITO are the same as for the single layer stack solar cells and can be found in Table A.2. The used dst wafers have a base resistivity of 1 $\Omega\,\mathrm{cm}^2$. The tunnel SiO_2 is produced in 60 °C piranha solution for 10 min.

Double layer stack optimization To optimize the double layer µc-SiC:H(n) stack a high number of experiments is necessary to evaluate all deposition parameters of both layer. To reduce the number of experiments five deposition parameters are selected and investigated using DoE with a fractional factorial plan. The five selected deposition parameters are tested on a high and a low level as shown in Table A.3. The deposition parameters regarding the other HWCVD deposition parameters (N_2 flow excluded), PECVD of the a-Si:H(i/p), and PVD of the ITO are the same as for the single layer stack solar cells and can be found in Table A.2. Using a DoE with a fractional factorial plan leads to a reduced number of experiments since not all parameter combinations are tested $2^{5-1} = 16$. The first four parameters are tested with all parameter combinations as a full factorial experimental plan. However, the levels of the fifth parameter (either high or low i.e. 1 or -1) are calculated by multiplying the levels of the first four parameters. Since the fifth parameter is now confounded with the first four parameters only the effects of the parameters can be calculated as shown in Equation 6.1. To calculate the significance of the effect three center points with levels 0.5 of the high level are added to the experiment resulting in a total of 19 experiments. The experimental matrix is shown in Table A.4. Further details about the DoE and available experimental plans can be found in [216–220]. For the design and the evaluation of the results the Software Chemoface is used [221].

Table A.3.: *Deposition parameters and their set values for the «high» and «low» levels during HWCVD deposition of the passivation and conductive layer.*

parameter	unit	high (1)	low (-1)
$T_\mathrm{f}^\mathrm{pass}$	°C	1775	1875
$d_\mathrm{SiC}^\mathrm{pass}$	nm	3	12
$T_\mathrm{f}^\mathrm{cond}$	°C	1950	2060
$d_\mathrm{SiC}^\mathrm{cond}$	nm	11	27
F_N2	sccm	30	100

Table A.4.: *Fractional factorial design for DoE experiments to evaluate effects of the thickness of the µc-SiC:H(n) passivation layer (d_{SiC}^{pass}), filament temperature of the passivation layer (T_f^{pass}), thickness of the µc-SiC:H(n) conductive layer (d_{SiC}^{cond}), filament temperature of the conductive layer (T_f^{cond}), and flow rate of nitrogen gas (F_{N2}).*

Experiment	$d_\mathrm{SiC}^\mathrm{pass}$ nm	$T_\mathrm{f}^\mathrm{pass}$ °C	$d_\mathrm{SiC}^\mathrm{cond}$ nm	$T_\mathrm{f}^\mathrm{cond}$ °C	F_N2 sccm
1	3	1775	11	1950	100
2	3	1775	11	2060	30
3	3	1775	27	1950	30
4	3	1775	27	2060	100
5	3	1875	11	1950	30
6	3	1875	11	2060	100
7	3	1875	27	1950	100
8	3	1875	27	2060	30
9	13	1775	11	1950	30
10	13	1775	11	2060	100
11	13	1775	27	1950	100
12	13	1775	27	2060	30
13	13	1875	11	1950	100
14	13	1875	11	2060	30
15	13	1875	27	1950	30
16	13	1875	27	2060	100
17	8	1825	16	2010	65
18	8	1825	16	2010	65
19	8	1825	16	2010	65

A.4. TCO development for TPC

TCO screening For the TCO screening experiments several TCOs (AZO, IWO, and ITO I) have been prepared by cooperation partner thus the deposition information are undisclosed. The ITO deposition conditions for the rear side are not changed and can be found in Table A.2. The TCO free solar cells has a very high reflection due to the missing anti-reflection effect of the TCO, thus, a 120 nm thick MgF_2 ARC was thermally evaporated. The used dst wafers have a base resistivity of 1 Ω cm^2. The tunnel SiO_2 is produced in 60 °C piranha solution for 10 min.

Table A.5.: *Deposition details for HWCVD of µc-SiC:H(n), PECVD of a-Si:H(i)/a-Si:H(p), and PVD of ITO. Differences of ITO deposition on front (n) and rear (p) side are separated by a slash.*

HWCVD			PECVD (i/p)		
System		p-HW	System		Maria
T_H	°C	250	T_H	°C	200
p_{dep}	mbar	0.75	$d_{a\text{-}Si}$	nm	7/7.4
$d_{f\text{-}s}$	mm	57	P_{dep}	W	50/90
H_2 flow	sccm	94	H_2 flow	sccm	650/500
MMS flow	sccm	6	SiH_4 flow	sccm	145/50
N_2 flow	sccm	30	TMB flow	sccm	0/100
T_f^{pass}	°C	1775			
T_f^{cond}	°C	1950			

Table A.6.: *Deposition details for the ITiO and ITO TCOs which have been prepared by in-house sputtering.*

ITiO			ITO II		
System		CT-2	System		Lissy
T_H	°C	100	T_H	°C	250
p_{dep}	µbar	3	p_{dep}	µbar	15
P_{Gen}	W	100	P_{Gen}	kW	3.35
Ar flow	sccm	15	Ar flow	sccm	197
1%Ar/O_2 flow	sccm	15	O_2 flow	sccm	3

Optimization of ITO sputter parameters To improve the sputter deposition process a design of experiment using a full factorial plan is used. In this DoE the sputter pressure and the sputter power was systematically varied. The used dst wafers have a base resistivity of 1 $\Omega\,\mathrm{cm}^2$. The tunnel $\mathrm{SiO_2}$ is produced in 60 °C piranha solution for 10 min.

Table A.7.: *Deposition details for HWCVD of µc-SiC:H(n), PECVD of a-Si:H(i)/a-Si:H(p), and PVD of ITO. Differences of ITO deposition on front (n) and rear (p) side are separated by a slash.*

HWCVD			PECVD (i/p)			PVD (n/p)		
System		p-HW	System		Maria	System		Lissy
T_H	°C	250	T_H	°C	200	T_H	°C	250
p_dep	mbar	0.75	$d_\text{a-Si}$	nm	7/7.4	p_dep	µbar	6/3
$d_\text{f-s}$	mm	57	P_dep	W	50/90	P_Gen	kW	5
$\mathrm{H_2}$ flow	sccm	94	$\mathrm{H_2}$ flow	sccm	650/500	Ar flow	sccm	197/90
MMS flow	sccm	6	$\mathrm{SiH_4}$ flow	sccm	145/50	$\mathrm{O_2}$ flow	sccm	3/5
$\mathrm{N_2}$ flow	sccm	30	TMB flow	sccm	0/100			
$T_\mathrm{f}^\mathrm{pass}$	°C	1775						
$T_\mathrm{f}^\mathrm{cond}$	°C	1950						

A.5. Results of the certification

Before MgF_2 anti-reflection coating

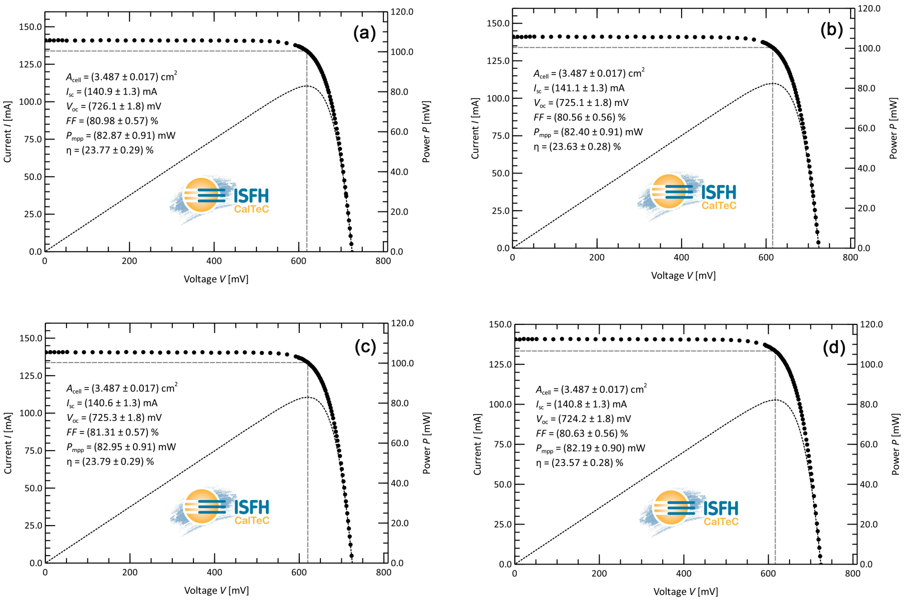

Figure A.1.: *Independently certified JV measurements by CalTeC of ISFH of the four best solar cells on one wafer from the ITO optimization experiment as described in Section 6.4. The certification was done on the solar cells without MgF_2 ARC. The measurments were performed in a way that only the rear contact of the solar cell under test was contacted. This was achieved by using an isolation foil on the rear side during measurements. This figure was originally published in [9] and was adapted (CC BY 4.0).*

After MgF_2 anti-reflection coating

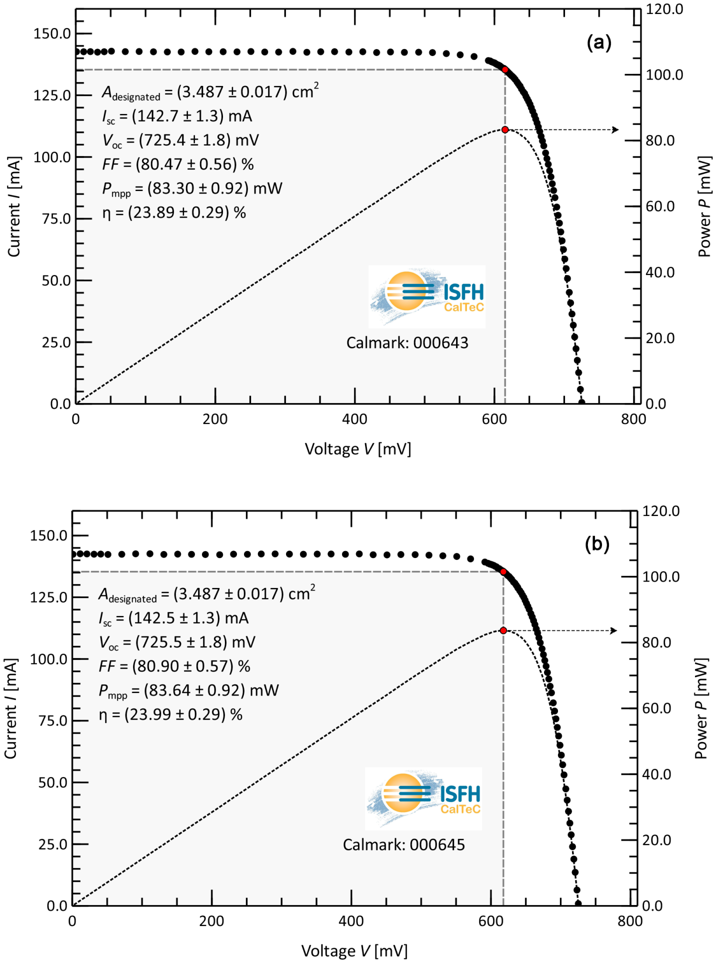

Figure A.2.: *Independently certified JV measurements by CalTeC of ISFH of the two best solar cells from b and c in Figure A.1). The certification was done after a deposition of 125 nm* MgF_2 *as anARC as described in Section 6.5. Subsequently the solar cells have been cured on a hot plate for 20 min at 230°C. The measurments were performed in a way that only the rear contact of the solar cell under test was contacted. This was achieved by using an isolation foil on the rear side during measurements. This figure was originally published in [9] and was adapted (CC BY 4.0).*

B. Abbreviations and Symbols

Variables and physical constants

α	optical absorption coefficient
$\alpha_{\mathbf{1eV}}$	sub-bandgap absorption at the photon energy of 1.0 eV
ϵ_0	vacuum permittivity
$\epsilon_{\mathbf{r}}$	relative permittivity
η	power conversion efficiency
$\eta_{\mathbf{e}}$	electrochemical potential of electrons
$\eta_{\mathbf{h}}$	electrochemical potential of holes
$\eta_{\mathbf{max}}$	maximum power conversion efficiency
λ	wavelength
μ	charge carrier mobility
ν	wavenumber
$\xi_{\mathbf{e}}$	chemical potential of electrons
$\xi_{\mathbf{h}}$	chemical potential of holes
$\rho_{\mathbf{c}}$	contact resistivity
$\rho_{\mathbf{M}}$	resistivity of the majority carriers
$\rho_{\mathbf{m}}$	resistivity of the minority carriers
$\rho_{\mathbf{SiO2}}$	atomic density of the SiO_2
σ	electrical conductivity
$\sigma_{\mathbf{e}}$	electrical conductivity of electrons
$\sigma_{\mathbf{h}}$	electrical conductivity of holes
$\sigma_{\mathbf{trap,e}}$	capture cross section for electrons of a trap state
$\tau_{\mathbf{Auger}}$	Auger lifetime
$\tau_{\mathbf{eff}}$	effective minority carrier lifetime
$\tau_{\mathbf{rad}}$	radiative carrier lifetime
Φ	height of the potential barrier of SiO_2
C	capacitance
$c_{\mathbf{N}}$	nitrogen concentration
$d_{\mathbf{SiC}}$	film thickness of µc-SiC:H(n)
$d_{\mathbf{SiC}}^{\mathbf{cond}}$	thickness of the µc-SiC:H(n) conductive layer

$d_{\mathbf{SiC}}^{\mathbf{pass}}$	thickness of the µc-SiC:H(n) passivation layer
$d_{\mathbf{SiO2}}$	thickness of silicon oxide layer
$d_{\mathbf{a\text{-}Si}}$	thickness of amorphous silicon layer
$d_{\mathbf{f\text{-}s}}$	distance between filament and substrate
$D_{\mathbf{e}}$	electron diffusion coefficient
$D_{\mathbf{it}}$	defect density at the c-Si interface
E	effect of a parameter in a DoE
E_{04}	optical bandgap
$E_{\mathbf{c}}$	conduction band edge
$E_{\mathbf{F}}$	Fermi level
$E_{\mathbf{Fe}}$	energy of the quasi Fermi level of electrons
$E_{\mathbf{Fh}}$	energy of the quasi Fermi level of holes
$E_{\mathbf{g}}$	bandgap energy
$E_{\mathbf{Ph}}$	photon energy
EQE	external quantum efficiency
$E_{\mathbf{v}}$	valence band edge
FF	fill factor
FF_0	fill factor without the influence of the series resistance
$FF_{\mathbf{J01}}$	upper fill factor limit which includes only J_{01} recombination
$\boldsymbol{\Delta} FF_{\mathbf{J02}}$	fill factor loss due to J_{02} recombination
$\boldsymbol{\Delta} FF_{\mathbf{Rs}}$	fill factor loss due to R_{s} recombination
$\boldsymbol{\Delta} FF_{\mathbf{Rsh}}$	fill factor loss due to R_{sh} recombination
$F_{\mathbf{MMS}}$	flow rate of monomethylsilane gas
$F_{\mathbf{N2}}$	flow rate of nitrogen gas
G	generation rate
$\hbar$	reduced Planck constant
$iV_{\mathbf{oc}}$	implied open circuit voltage
$I_{\mathbf{H}}$	intensity of the hydrogen signal in ToF-SIMS measurements
$I_{\mathbf{O}}$	intensity of the oxygen signal in ToF-SIMS measurements
$I_{\mathbf{PL}}$	intensity of the PL signal
IQE	internal quantum efficiency
$I_{\mathbf{Si\text{-}C}}$	intensity of the Si–C stretch mode in FTIR spectroscopy
$I_{\mathbf{Si\text{-}H}}$	intensity of the Si–H mode in FTIR spectroscopy
$J_{\mathbf{0}}$	saturation current density
$J_{\mathbf{01}}$	saturation current density of the first diode
$J_{\mathbf{02}}$	saturation current density of the second diode
$J_{\mathbf{0,M}}$	majority saturation current density
$J_{\mathbf{0,m}}$	minority saturation current density
$J_{\mathbf{c}}$	recombination parameter
$J_{\mathbf{diff}}$	diffusion current

$J_{\mathbf{drift}}$	drift current
$J_{\mathbf{ex}}$	external current
$J_{\mathbf{m}}$	minority carrier current density
$J_{\mathbf{ph}}$	photo-current density
$J_{\mathbf{SiC}}^{\mathbf{abs}}$	parasitic absorption current density loss
$J_{\mathbf{sc}}$	short circuit current density
$\mathbf{k_B}$	Boltzmann constant
$L_{\mathbf{SiC}}$	average µc-SiC:H(n) grain size measured by XRD
$m_{\mathbf{t}}$	tunneling mass
n	charge carrier density
$n_{\mathbf{e}}^{0}$	equilibrium electron concentration
$n_{\mathbf{e}}$	electron concentration
$n_{\mathbf{h}}$	hole concentration
$n_{\mathbf{i}}$	intrinsic charge carrier concentration
$n_{\mathbf{trap,h}}$	density of trap states filled with a hole
$\Delta n_{\mathbf{e}}$	excess electron concentration
$N_{\mathbf{A}}$	acceptor doping concentration
$N^{\mathbf{act}}$	active doping concentration
$N_{\mathbf{c}}$	effective density of states in the conduction band
$N_{\mathbf{D}}$	donor doping concentration
$N_{\mathbf{D}}^{\mathbf{act}}$	active donor doping concentration
$N_{\mathbf{v}}$	effective density of states in the valence band
$p_{\mathbf{dep}}$	deposition pressure
pFF	pseudo fill factor
$P_{\mathbf{dep}}$	deposition power
$P_{\mathbf{Gen}}$	generator power of PECVD
$P_{\mathbf{max}}$	maximum power of the solar cell
$P_{\mathbf{sun}}$	power of the incoming sunlight
$\mathbf{q}$	elementary charge
$Q_{\mathbf{fix}}$	fixed charge density
R	reflectance
$R_{\mathbf{Aug}}$	Auger recombination rate
$R_{\mathbf{ms}}$	root mean squared roughness
$R_{\mathbf{rad}}$	radiative recombination rate
$R_{\mathbf{s}}$	series resistance
$R_{\mathbf{sh}}$	shunt resistance
$R_{\mathbf{SRH}}$	Shockley-Read-Hall recombination rate
$R_{\mathbf{surf}}$	surface recombination rate
S	selectivity
$S_{\mathbf{10}}$	logarithm of selectivity

$S_{\mathbf{e}}$	surface recombination velocity of electrons
$t_{\mathbf{int}}$	integration time of the PL image
$t_{\mathbf{ox}}$	oxidation time
T	temperature
T_λ	transmittance
$T(E)$	quantum mechanical tunnel probability
$T_{\mathbf{f}}$	filament temperature
$T_{\mathbf{f}}^{\mathbf{cond}}$	filament temperature of the conductive layer
$T_{\mathbf{f}}^{\mathbf{pass}}$	filament temperature of the passivation layer
$T_{\mathbf{H}}$	substrate heater temperature
U	recombination rate
$v_{\mathbf{e}}$	velocity of the electrons
V	voltage
$V_{\mathbf{oc}}$	open circuit voltage
$V_{\mathbf{th}}$	thermal voltage
W	thickness of the wafer

Material and elements

Ag	silver
Al	aluminium
$\mathbf{Al_2O_3}$	aluminum oxide
Ar	argon
AZO	aluminum-doped zinc oxide
$\mathbf{DI\text{-}H_2O}$	deionised water
H	hydrogen
$\mathbf{H_2}$	molecular hydrogen
HCl	hydrochloric acid
HF	hydrofluoric acid
$\mathbf{HNO_3}$	nitric acid
$\mathbf{H_2O}$	water
$\mathbf{H_2O_2}$	hydrogenperoxide
$\mathbf{H_2SO_4}$	sulfuric acid
IOH	hydrogen-doped indium oxide
ITO	indium tin oxide
ITiO	titanium-doped indium oxide
IWO	tungsten-doped indium oxide
(*i*)	intrinsic
KOH	potassium hydroxide
$\mathbf{MgF_2}$	magnesium fluoride

MMS	monomethylsilane H_3Si-CH_3
($\boldsymbol{n}$)	n-type doped
$\mathbf{N}_2$	molecular nitrogen
$\mathbf{NH}_3$	ammonia
$\mathbf{NH}_4\mathbf{OH}$	ammonium hydroxide
O	oxygen
$\mathbf{O}_2$	molecular oxygen
piranha	mixture from sulfuric acid with hydrogenperoxide H_2SO_4:H_2O_2
P	phosphorous
$\mathbf{PH}_3$	phosphine
($\boldsymbol{p}$)	p-type doped
Si	silicon
$^{30}\mathbf{Si}$	isotope of silicon with 30 nucleons
a-Si:H	hydrogenated amorphous silicon
a-Si:H($\boldsymbol{i}$)	intrinsic hydrogenated amorphous silicon
a-Si:H($\boldsymbol{n}$)	n-type doped hydrogenated amorphous silicon
a-Si:H($\boldsymbol{p}$)	p-type doped doped hydrogenated amorphous silicon
c-Si	crystalline silicon
poly-Si	polycrystalline silicon
µc-SiC:H($\boldsymbol{n}$)	n-type hydrogenated microcrystalline silicon carbide
$\mathbf{SiH}_4$	silane
$\mathbf{SiN}_\mathbf{x}$	sub-stoichiometric silicon nitride
$\mathbf{SiO}_2$	silicon dioxide
TMB	trimethylboran (C_3H_9B)

Abbreviations

ALD	atomic layer deposition
AM	air-mass
ARC	anti-reflection coating
c-AFM	conductive atomic force microscopy
Cat-CVD	catalytic chemical vapor deposition
CC BY 4.0	Creative Commons Attribution 4.0 International License http://creativecommons.org/licenses/by/4.0
Cz	Czochralski
DoE	design of experiment
dsp	double side polished
dst	double side textured
$\mathbf{e}_c^-$	electron in the conduction band
eCV	electrochemical capacitance-voltage profiling

FTIR	Fourier transform infrared spectroscopy
fz	float zone
$\mathbf{h}_\mathrm{v}^{+}$	hole in the valence band
HWCVD	hot wire chemical vapor deposition
IBC	interdigitated back contact
ISFH	Institute for Solar Energy Research in Hamelin
JV	current density-voltage
MFC	mass flow controler
MOS	metal-oxide semiconductor
PC	photo-conductance
PDS	photothermal deflection spectroscopy
QSS	quasi-steady state mode
PECVD	plasma enhanced chemical vapor deposition
PEEM	photoemission electron microscopy
PERC	passivated emitter and rear cell
PES	photoemission spectroscopy
PL	photo-luminescence
PVD	physical vapor deposition
QDR	Quick Dump Rinse
QFL	quasi-Fermi level
RCA	cleaning process developed at the Radio Corporation of America
RPD	reactive plasma deposition
RT	room temperature
SC-1	Standard Clean 1
SC-2	Standard Clean 2
SE	spectral ellipsometry
SHJ	silicon heterojunction
ToF-SIMS	time-of-flight secondary ion mass spectroscopy
SRH	Shockley-Read-Hall
TCO	transparent conducting oxide
TEM	transmission electron microscopy
TLM	transfer length method
TPC	transparent passivating contact
T & R	transmission and reflection
UV	ultraviolet radiation
VUV	vacuum ultraviolet radiation
XPS	X-ray photoelectron spectroscopy
XRD	X-ray diffraction

C. List of Publications

Publications related to this work

1. M. Köhler, M. Pomaska, F. Lentz, F. Finger, U. Rau, and K. Ding, *Wet-Chemical Preparation of Silicon Tunnel Oxides for Transparent Passivated Contacts in Crystalline Silicon Solar Cells*, ACS Applied Materials & Interfaces **10**, 17, 14259 – 14263 (2018), 10.1021/acsami.8b02002
2. M. Köhler, A. Zamchiy, M. Pomaska, A. Lambertz, F. Lentz, W. Duan, V. Smirnov, F. Finger, U. Rau, and K. Ding, *Development of a Transparent Passivated Contact as a Front Side Contact for Silicon Heterojunction Solar Cells*, IEEE 7th World Conference on Photovoltaic Energy Conversion (WCPEC) (A Joint Conference of 45th IEEE PVSC, 28th PVSEC & 34th EU PVSEC), Waikoloa, Hawaii, 3468 – 3472 (2018), 10.1109/PVSC.2018.8548008
3. M. Köhler, A. Zamchiy, M. Pomaska, A. Lambertz, F. Lentz, W. Duan, V. Smirnov, F. Finger, U. Rau, and K. Ding, *Optimization of Transparent Passivating Contact for Crystalline Silicon Solar Cells*, IEEE Journal of Photovoltaics **10**, 1, 1960 – 1964 (2020), 10.1109/JPHOTOV.2019.2947131
4. M. Pomaska, M. Köhler, P. Moya, A. Zamchiy, A. Singh, D. Kim, O. Isabella, V. Smirnov, M. Zeman, S. Li, K. Qiu, A. Eberst, V. Smirnov, F. Finger, U. Rau, and K. Ding, *Transparent silicon carbide/tunnel SiO_2 passivation for c-Si solar cell front side: Enabling $J_{sc} > 42$ mA/cm^2 and iV_{oc} of 742 mV*, Progress in Photovoltaics: Research and Applications **28**, 4, 321 – 327 (2020), 10.1002/pip.3244

5. M. Köhler, M. Pomaska, P. Procel, R. Santbergen, A. Zamchiy, B. Macco, A. Lambertz, W. Duan, P. Cao, B. Klingebiel, S. Li, A. Eberst, M. Luysberg, K. Qiu, O. Isabella, F. Finger, T. Kirchartz, U. Rau, and K. Ding, *A silicon carbide based highly transparent passivating contact for crystalline silicon solar cells approaching efficiencies of 24%*, Nature Energy **6**, 529 – 537 (2021), 10.1038/s41560-021-00806-9

Other publications

1. Y. Liu, M. Pomaska, K. Ding, W. Duan, D. Kim, M. Köhler, U. Breuer, and K. Ding *Phosphorous Catalytic-Doping of Silicon Alloys for the Use in Silicon Heterojunction Solar Cells*, Advanced Engineering Materials **22**, 6, 1900613 (2020), 10.1002/adem.201900613
2. S. Li, M. Pomaska, A. Lambertz, W. Duan, K. Bittkau, D. Qiu, Z. Yao, M. Luysberg, P. Steuter, M. Köhler, K.Qiu, R. Hong, H. Shen, F. Finger, T. Kirchartz, U. Rau, K. Ding, *Transparent-Conductive-Oxide-Free Front Contacts for High Efficiency Silicon Heterojunction Solar Cells* , Joule, (2021), 10.1016/j.joule.2021.04.004 accepted manuscript; also available at Research Square Preprint, Version 1, (2020), 10.21203/rs.3.rs-97106/v1
3. F. Li, W. Duan, M. Pomaska, M. Köhler, S. Zhou, W. Niu, K. Ding, Y. Pu, U. Aeberhard, and Uwe Rau, *Quantum transport across amorphous-crystalline interfaces in Tunnel-Oxide Passivated Contact solar cells: direct vs. defect-assisted tunneling*, Chinese Physics Letters, **38**, 3, 036301 (2021), 10.1088/0256-307X/38/3/036301

D. Curriculum Vitae

Personal details

Name	Malte Köhler
Date of birth	August 30th, 1990
Place of birth	Hildesheim, Germany
Citizenship	German

Education

1997 – 2001	Grundschule Ochtersum, Hildesheim
2001 – 2003	Orientierungsstufe Stadtmitte, Hildesheim
2003 – 2010	Goethegymnasium, Hildesheim
2010 – 2013	Bachelor of Engineering in Photovoltaics at Hochschule Anhalt, Köthen Bachelor thesis at Fraunhofer Center for Silicon Photovoltaics
2013 – 2016	Master of Science in Engineering Physics at the University of Oldenburg Main subjects: renewable energies and laser & optics Master thesis at University of Oldenburg, Energy and Semiconductor Research
2016 – 2020	PhD thesis at the Forschungszentrum Jülich GmbH, IEK 5 – Photovoltaics

References

[1] World Population Prospects 2019, Report, United Nations, Department of Economic and Social Affairs, Population Division, 2019.

[2] B. Dudley, BP Statistical Review of World Energy 2019, Report, BP p.l.c., London, 2019.

[3] United Nations: Paris Agreement, Report, United Nations, New York, 2016.

[4] IRENA, Future of solar photovoltaic - Deployment, investment, technology, grid integration and socio-economic aspects, Report, International Renewable Energy Agency, Abu Dhabi, 2019.

[5] V. Shah, J. Booream-Phelps, and S. Min, 2014 Outlook: Let the Second Gold Rush Begin, Report, Deutsche Bank Markets Research, 2014.

[6] S. Philipps and W. Warmuth, Fraunhofer ISE: Photovoltaics Report, updated: 14 November 2019, Report, Fraunhofer ISE, Freiburg im Breisgau, 2019.

[7] R. Swanson and R. Sinton, High-Efficiency Silicon Solar Cells, in *Advances in Solar Energy: An Annual Review of Research and Development*, edited by K. W. Böer, chapter 4, pages 427–484, Springer, New York, 1 edition, 1990.

[8] S. W. Glunz and F. Feldmann, Solar Energy Materials and Solar Cells **185**, 260 (2018), doi:10.1016/j.solmat.2018.04.029.

[9] M. Köhler et al., Nature Energy **6**, 529 (2021), doi:10.1038/s41560-021-00806-9.

[10] M. Pomaska, *Microcrystalline Silicon Carbide for Silicon Heterojunction Solar Cells*, Phd thesis, RWTH Aachen University, 2017.

[11] R. P. Huebener, Electric Conductor or Insulator? – Energy Bands, in *Conductors, Semiconductors, Superconductors: An Introduction to Solid State*

[12] P. P. Altermatt, A. Schenk, F. Geelhaar, and G. Heiser, Journal of Applied Physics **93**, 1598 (2003), doi:10.1063/1.1529297.

[13] S. Hunklinger, *Festkörperphysik*, De Gruyter, München, 4 edition, 2014.

[14] P. Würfel, *Physik der Solarzellen*, volume 2, Springer Spektrum, 2000.

[15] P. Auger, C.R.A.S. **177**, 169 (1923).

[16] W. Shockley and W. T. Read, Physical Review **87**, 835 (1952), doi:10.1103/PhysRev.87.835.

[17] R. N. Hall, Physical Review **87**, 387 (1952), doi:10.1103/PhysRev.87.387.

[18] B. Das, I. Aguilera, U. Rau, and T. Kirchartz, Physical Review Materials **4**, 024602 (2020), doi:10.1103/PhysRevMaterials.4.024602.

[19] T. Tiedje, E. Yablonovitch, G. G. D. Cody, and B. G. B. Brooks, IEEE Transactions on Electron Devices **31**, 711 (1984), doi:10.1109/T-ED.1984.21594.

[20] J. Szlufcik, S. Sivoththaman, J. Nlis, R. Mertens, and R. Van Overstraeten, Proceedings of the IEEE **85**, 711 (1997), doi:10.1109/5.588971.

[21] M. A. Green, Physica E: Low-dimensional Systems and Nanostructures **14**, 11 (2002), doi:10.1016/S1386-9477(02)00354-5.

[22] P. Würfel, Physica E: Low-dimensional Systems and Nanostructures **14**, 18 (2002), doi:10.1016/S1386-9477(02)00355-7.

[23] U. Würfel, A. Cuevas, and P. Wurfel, IEEE Journal of Photovoltaics **5**, 461 (2015), doi:10.1109/JPHOTOV.2014.2363550.

[24] I. Morá-Seró, J. Bisquert, I. Mora-Seró, and J. Bisquert, Solar Energy Materials and Solar Cells **85**, 51 (2005), doi:10.1016/j.solmat.2004.04.008.

[25] W. Tress, K. Leo, and M. Riede, Physical Review B **85**, 155201 (2012), doi:10.1103/PhysRevB.85.155201.

[26] E. T. Roe, K. E. Egelhofer, and M. C. Lonergan, ACS Applied Energy Materials **1**, 1037 (2018), doi:10.1021/acsaem.7b00179.

[27] R. Brendel and R. Peibst, IEEE Journal of Photovoltaics **6**, 1413 (2016), doi:10.1109/JPHOTOV.2016.2598267.

[28] U. Rau and T. Kirchartz, Advanced Materials Interfaces **6**, 1900252 (2019),

doi:10.1002/admi.201900252.

[29] M. A. Green, Solid-State Electronics **24**, 788 (1981), doi:10.1016/0038-1101(81)90062-9.

[30] B. Lim, T. Brendemuhl, T. Dullweber, and R. Brendel, IEEE Journal of Photovoltaics **6**, 447 (2016), doi:10.1109/JPHOTOV.2016.2520211.

[31] R. Brendel et al., Progress in Photovoltaics: Research and Applications **24**, 1475 (2016), doi:10.1002/pip.2696.

[32] M. Müller et al., Loss analysis of 22% efficient industrial PERC solar cells, in *Energy Procedia*, volume 124, pages 131–137, Elsevier, 2017, doi:10.1016/j.egypro.2017.09.322.

[33] P. Saint-Cast et al., Physica Status Solidi (A) Applications and Materials Science **214**, 1600708 (2017), doi:10.1002/pssa.201600708.

[34] A. W. Stephens, A. G. Aberle, and M. A. Green, Journal of Applied Physics **76**, 363 (1994), doi:10.1063/1.357082.

[35] M. J. Kerr and A. Cuevas, Semiconductor Science and Technology **17**, 35 (2002), doi:10.1088/0268-1242/17/1/306.

[36] A. G. Aberle, Solar Energy Materials and Solar Cells **65**, 239 (2001), doi:10.1016/S0927-0248(00)00099-4.

[37] S. Y. Herasimenka, W. J. Dauksher, and S. G. Bowden, Applied Physics Letters **103**, 053511 (2013), doi:10.1063/1.4817723.

[38] J. Schmidt, R. Peibst, and R. Brendel, Solar Energy Materials and Solar Cells **187**, 39 (2018), doi:10.1016/j.solmat.2018.06.047.

[39] L. Black et al., Solar Energy Materials and Solar Cells **188**, 182 (2018), doi:10.1016/j.solmat.2018.07.003.

[40] A. W. Blakers, A. Wang, A. M. Milne, J. Zhao, and M. A. Green, Applied Physics Letters **55**, 1363 (1989), doi:10.1063/1.101596.

[41] M. A. Green, Solar Energy Materials and Solar Cells **143**, 190 (2015).

[42] B. Min et al., IEEE Journal of Photovoltaics **7**, 1541 (2017), doi:10.1109/JPHOTOV.2017.2749007.

[43] M. Taguchi et al., Progress in Photovoltaics: Research and Applications **8**, 503

(2000), doi:10.1002/1099-159X(200009/10)8:5<503::AID-PIP347>3.0.CO;2-G.

[44] F. Einsele, P. J. Rostan, M. B. Schubert, and U. Rau, Journal of Applied Physics **102**, 094507 (2007), doi:10.1063/1.2803749.

[45] Hanergy, Twitter: Hanergy's SHJ technology sets a new world record for 6-inch silicon batteries with 25.11% conversion efficiency., 2019. `https://twitter.com/HanergyGlobal/status/1195261597461229569`, Accessed: 04/03/2020

[46] M. Hutchins, PV-magazin: Hanergy hits 25.11% efficiency with HJT cell, 2019. `https://www.pv-magazine.com/2019/11/20/hanergy-sets-new-heterojunction-module-efficiency-record/`, Accessed: 04/03/2020

[47] D. Adachi, J. L. Hernández, and K. Yamamoto, Applied Physics Letters **107**, 233506 (2015), doi:10.1063/1.4937224.

[48] F. Li et al., Chinese Physics Letters **38**, 036301 (2021), doi:10.1088/0256-307X/38/3/036301.

[49] U. Römer et al., Solar Energy Materials and Solar Cells **131**, 85 (2014), doi:10.1016/j.solmat.2014.06.003.

[50] Y. Chen et al., Progress in Photovoltaics: Research and Applications **27**, 827 (2019), doi:10.1002/pip.3180.

[51] A. Richter et al., Solar Energy Materials and Solar Cells **173**, 96 (2017), doi:10.1016/j.solmat.2017.05.042.

[52] M. A. Green et al., Progress in Photovoltaics: Research and Applications **28**, 3 (2020), doi:10.1002/pip.3228.

[53] M. Rienäcker et al., IEEE Journal of Photovoltaics **7**, 11 (2017), doi:10.1109/JPHOTOV.2016.2614123.

[54] S. Reiter et al., Parasitic Absorption in Polycrystalline Si-layers for Carrier-selective Front Junctions, in *Energy Procedia*, volume 92, pages 199–204, Chambéry, France, 2016, Elsevier Ltd, doi:10.1016/j.egypro.2016.07.057.

[55] F. Feldmann, C. Reichel, R. Müller, and M. Hermle, Solar Energy Materials and Solar Cells **159**, 265 (2017), doi:10.1016/j.solmat.2016.09.015.

[56] F. Feldmann et al., High and Low Work Function Materials for Passivated Contacts, in *Energy Procedia*, volume 77, pages 263–270, 2015, doi:10.1016/j.egypro.2015.07.037.

[57] A. B. Morales-Vilches et al., ZnO:Al/a-SiOx front contact for polycrystalline-silicon-on-oxide (POLO) solar cells, in *8th International Conference on Crystalline Silicon Photovoltaics March 19-21*, page 040016, Lausanne, Switzerland, 2018, doi:10.1063/1.5049279.

[58] L. Tutsch et al., Solar Energy Materials and Solar Cells **200**, 109960 (2019), doi:10.1016/j.solmat.2019.109960.

[59] Y. Larionova et al., Screen Printed Double-Side Contacted POLO-Cells with Ultra-Thin Poly-Si Layers and Different Transparent Conductive Oxides, in *36th European Photovoltaic Solar Energy Conference and Exhibition*, pages 172–175, Marseille, 2019, WIP, doi:10.4229/EUPVSEC20192019-2BO.2.6.

[60] M. Lozac'h, S. Nunomura, and K. Matsubara, Solar Energy Materials and Solar Cells **207**, 110357 (2020), doi:10.1016/j.solmat.2019.110357.

[61] J. Dabrowski and H.-J. Müssig, *Silicon Surfaces and Formation of Interfaces - Basic Science in the Industrial World*, World Scientific, Singapore, 2000.

[62] C. R. Helms and B. E. Deal, editors, *The Physics and Chemistry of SiO2 and the Si-SiO2 Interface*, Springer US, Boston, MA, 1988.

[63] S. Takami, Y. Egashira, and H. Komiyama, Japanese Journal of Applied Physics **36**, 2288 (1997), doi:10.1143/JJAP.36.2288.

[64] H. Z. Massoud, J. D. Plummer, and E. A. Irene, Journal of The Electrochemical Society **132**, 2693 (1985), doi:10.1149/1.2113649.

[65] W. Kern and D. A. Puotinen, RCA Review **31** (1970).

[66] C. K. Fink, K. Nakamura, S. Ichimura, and S. J. Jenkins, Journal of Physics: Condensed Matter **21**, 183001 (2009), doi:10.1088/0953-8984/21/18/183001.

[67] A. Moldovan et al., Energy Procedia **55**, 834 (2014), doi:10.1016/j.egypro.2014.08.067.

[68] G. Micard et al., Advances in the understanding of phosphorus silicte glass (PSG) formation for accurate process simulation of phosphorus diffu-

sion, in *27th European Photovoltaic Solar Energy Conference and Exhibition*, pages 1355–1359, Frankfurt Germany, 2012, doi:10.4229/27thEUPVSEC2012-2BV.5.8.

[69] H. Li et al., Frontiers in Energy **11**, 42 (2017), doi:10.1007/s11708-016-0433-7.

[70] P. Ostoja, S. Guerri, P. Negrini, and S. Solmi, Solar Cells **11**, 1 (1984), doi:10.1016/0379-6787(84)90114-5.

[71] A. W. Blakers and M. A. Green, Applied Physics Letters **48**, 215 (1986), doi:10.1063/1.96799.

[72] R. Hezel and R. Schörner, Journal of Applied Physics **52**, 3076 (1981), doi:10.1063/1.329058.

[73] C. Leguijt et al., Solar Energy Materials and Solar Cells **40**, 297 (1996), doi:10.1016/0927-0248(95)00155-7.

[74] B. Hoex et al., Applied Physics Letters **91**, 112107 (2007), doi:10.1063/1.2784168.

[75] B. Hoex, J. Schmidt, P. Pohl, M. C. M. van de Sanden, and W. M. M. Kessels, Journal of Applied Physics **104**, 044903 (2008), doi:10.1063/1.2963707.

[76] F. Werner and J. Schmidt, Applied Physics Letters **104**, 091604 (2014), doi:10.1063/1.4867652.

[77] F. Feldmann, M. Bivour, C. Reichel, M. Hermle, and S. W. Glunz, Solar Energy Materials and Solar Cells **120**, 270 (2014), doi:10.1016/j.solmat.2013.09.017.

[78] T. M. Buck and F. S. McKim, Journal of The Electrochemical Society **105**, 709 (1958), doi:10.1149/1.2428707.

[79] H. Angermann, W. Henrion, M. Rebien, and A. Röseler, Solar Energy Materials and Solar Cells **83**, 331 (2004), doi:10.1016/j.solmat.2004.01.031.

[80] F. J. Himpsel, F. R. McFeely, A. Taleb-Ibrahimi, J. A. Yarmoff, and G. Hollinger, Physical Review B **38**, 6084 (1988), doi:10.1103/PhysRevB.38.6084.

[81] A. Moldovan et al., Tunnel oxide passivated carrier-selective contacts based on ultra-thin SiO2 layers grown by photo-oxidation or wet-

chemical oxidation in ozonized water, in *2015 IEEE 42nd Photovoltaic Specialist Conference (PVSC)*, volume 142, pages 1–6, IEEE, 2015, doi:10.1109/PVSC.2015.7356144.

[82] S. Patzig-Klein, *Untersuchungen zum Reaktionsverhalten kristalliner Siliziumoberflächen in HF-basierten Ätzlösungen*, PhD thesis, TU Bergakademie Freiberg, 2009.

[83] E. Abel and H. Schmid, Zeitschrift für Physikalische Chemie **136U**, 279 (1928), doi:10.1515/zpch-1928-13631.

[84] A. A. Langford, M. L. Fleet, B. P. Nelson, W. A. Lanford, and N. Maley, Physical Review B **45**, 13367 (1992), doi:10.1103/PhysRevB.45.13367.

[85] A. C. Boccara, W. Jackson, N. M. Amer, and D. Fournier, Optics Letters **5**, 377 (1980), doi:10.1364/ol.5.000377.

[86] E. Peiner, Journal of The Electrochemical Society **142**, 576 (1995), doi:10.1149/1.2044101.

[87] R. Sinton, A. Cuevas, and M. Stuckings, Quasi-steady-state photoconductance, a new method for solar cell material and device characterization, in *Conference Record of the Twenty Fifth IEEE Photovoltaic Specialists Conference*, pages 457–460, IEEE, 1996, doi:10.1109/PVSC.1996.564042.

[88] R. A. Sinton and A. Cuevas, Applied Physics Letters **69**, 2510 (1996), doi:10.1063/1.117723.

[89] H. Nagel, C. Berge, and A. G. Aberle, Journal of Applied Physics **86**, 6218 (1999), doi:10.1063/1.371633.

[90] A. Cuevas and R. A. Sinton, Progress in Photovoltaics: Research and Applications **5**, 79 (1997), doi:10.1002/(SICI)1099-159X(199703/04)5:2<79::AID-PIP155>3.0.CO;2-J.

[91] A. Kimmerle, P. Rothhardt, A. Wolf, and R. A. Sinton, Increased reliability for J0-analysis by QSSPC, in *Energy Procedia*, volume 55, pages 101–106, Elsevier, 2014, doi:10.1016/j.egypro.2014.08.087.

[92] T. Fuyuki, H. Kondo, T. Yamazaki, Y. Takahashi, and Y. Uraoka, Applied Physics Letters **86**, 262108 (2005), doi:10.1063/1.1978979.

[93] T. Trupke, R. A. Bardos, M. C. Schubert, and W. Warta, Applied Physics Letters **89**, 044107 (2006), doi:10.1063/1.2234747.

[94] K. Ramspeck, S. Reissenweber, J. Schmidt, K. Bothe, and R. Brendel, Applied Physics Letters **93**, 102104 (2008), doi:10.1063/1.2972122.

[95] K. Ramspeck, K. Bothe, J. Schmidt, and R. Brendel, Journal of Applied Physics **106**, 114506 (2009), doi:10.1063/1.3261733.

[96] S. Herlufsen, J. Schmidt, D. Hinken, K. Bothe, and R. Brendel, Camera-Based Photoluminescence Lifetime Imaging of Crystalline Silicon Wafers, in *24th European Photovoltaic Solar Energy Conference*, pages 913–917, Hamburg, 2009, WIP-Munich, doi:10.4229/24thEUPVSEC2009-2AO.1.3.

[97] S. Herlufsen et al., Physica Status Solidi - Rapid Research Letters **5**, 25 (2011), doi:10.1002/pssr.201004426.

[98] S. Herlufsen, K. Bothe, J. Schmidt, R. Brendel, and S. Siegmund, Solar Energy Materials and Solar Cells **106**, 42 (2012), doi:10.1016/j.solmat.2012.06.002.

[99] U. Rau, IEEE Journal of Photovoltaics **2**, 169 (2012), doi:10.1109/JPHOTOV.2011.2179018.

[100] S. Eidelloth and R. Brendel, IEEE Electron Device Letters **35**, 9 (2014), doi:10.1109/LED.2013.2290602.

[101] B. Turan, *Laser processing for the integrated series connection of thin-film silicon solar cells*, PhD thesis, RWTH Aachen University, 2016.

[102] M. A. Green, *Solar Cells - Operating Principles, Technology and System Applications*, The University of New South Wales, Kensington, 1 edition, 1992.

[103] M. Wolf and H. Rauschenbach, Advanced Energy Conversion **3**, 455 (1963), doi:10.1016/0365-1789(63)90063-8.

[104] M. Köhler et al., ACS Applied Materials & Interfaces **10**, 14259 (2018), doi:10.1021/acsami.8b02002.

[105] W. Kulisch, T. Lippmann, and R. Kassing, Thin Solid Films **174**, 57 (1989), doi:10.1016/0040-6090(89)90869-9.

[106] S. C. Deshmukh and E. S. Aydil, Applied Physics Letters **65**, 3185 (1994),

doi:10.1063/1.112475.

[107] Y. Katamune, T. Negi, S. Tahara, K. Fukushima, and A. Izumi, Japanese Journal of Applied Physics **57**, 120301 (2018), doi:10.7567/JJAP.57.120301.

[108] J. Shewchun, R. Singh, and M. A. Green, Journal of Applied Physics **48**, 765 (1977), doi:10.1063/1.323667.

[109] International Technology Roadmap for Photovoltaic (ITRPV) - Results 2018 including maturity report 2019, Report, 2019.

[110] K. Ding et al., physica status solidi (RRL) - Rapid Research Letters **10**, 233 (2016), doi:10.1002/pssr.201510376.

[111] W. Kern, Journal of The Electrochemical Society **137**, 1887 (1990), doi:10.1149/1.2086825.

[112] H. Angermann, W. Herion, and A. Röseler, Wet-chemical conditioning of silicon: Electronic properties correlated with the surface morphology, in *Silicon-Based Material and Devices*, edited by H. S. Nalwa, chapter 7, pages 267–298, Elsevier, San Diego, 2001.

[113] A. Cuevas et al., Skin care for healthy silicon solar cells, in *2015 IEEE 42nd Photovoltaic Specialist Conference (PVSC)*, number 1, pages 1–6, IEEE, 2015, doi:10.1109/PVSC.2015.7356379.

[114] A. Cuevas et al., Solar Energy Materials and Solar Cells **184**, 38 (2018), doi:10.1016/j.solmat.2018.04.026.

[115] A. Moldovan, *Ozonbasierte Reinigungs- und Konditionierungsverfahren für die Herstellung hocheffizienter Silizium Solarzellen*, Phd thesis, Albert-Ludwigs-Universität Freiburg im Breisgau, 2015.

[116] Y. Yamashita, A. Asano, Y. Nishioka, and H. Kobayashi, Physical Review B **59**, 15872 (1999), doi:10.1103/PhysRevB.59.15872.

[117] H. Angermann, W. Henrion, A. Röseler, and M. Rebien, Materials Science and Engineering B: Solid-State Materials for Advanced Technology **73**, 178 (2000), doi:10.1016/S0921-5107(99)00457-2.

[118] H. Angermann, Characterization of wet-chemically treated silicon interfaces by surface photovoltage measurements, in *Analytical and Bioanalytical Chem-*

istry, volume 374, pages 676–680, 2002, doi:10.1007/s00216-002-1450-4.

[119] H. Angermann, J. Rappich, and C. Klimm, Central European Journal of Physics **7**, 363 (2009), doi:10.2478/s11534-009-0055-3.

[120] W. Nolting, Einfache Modellsysteme, in *Grundkurs Theoretische Physik 5/1*, Springer-Lehrbuch, chapter 4, Springer Berlin Heidelberg, Berlin, Heidelberg, 7 edition, 2002.

[121] R. Peibst et al., Solar Energy Materials and Solar Cells **158**, 60 (2016), doi:10.1016/j.solmat.2016.05.045.

[122] K. Lancaster, S. Großer, F. Feldmann, V. Naumann, and C. Hagendorf, Energy Procedia **92**, 116 (2016), doi:10.1016/j.egypro.2016.07.040.

[123] D. Tetzlaff et al., Energy Procedia **124**, 435 (2017), doi:10.1016/j.egypro.2017.09.270.

[124] A. S. Kale et al., Applied Physics Letters **114**, 083902 (2019), doi:10.1063/1.5081832.

[125] M. Morita, T. Ohmi, E. Hasegawa, M. Kawakami, and M. Ohwada, Journal of Applied Physics **68**, 1272 (1990), doi:10.1063/1.347181.

[126] Y. Sugita, S. Watanabe, and N. Awaji, Japanese Journal of Applied Physics **35**, 5437 (1996), doi:10.1143/JJAP.35.5437.

[127] T. Sato, T. Sugiura, M. Ohtsubo, S. Matsuno, and M. Konagai, Japanese Journal of Applied Physics **46**, 6796 (2007), doi:10.1143/JJAP.46.6796.

[128] T. Chen et al., Thin Solid Films **519**, 4511 (2011), doi:10.1016/j.tsf.2011.01.336.

[129] M. Pomaska et al., Japanese Journal of Applied Physics **56**, 022302 (2017), doi:10.7567/JJAP.56.022302.

[130] Asuha, T. Yuasa, O. Maida, and H. Kobayashi, Applied Physics Letters **80**, 4175 (2002), doi:10.1063/1.1482147.

[131] Y. Fukaya et al., Applied Surface Science **256**, 5610 (2010), doi:10.1016/j.apsusc.2010.03.032.

[132] S. Bordihn et al., Energy Procedia **8**, 654 (2011), doi:10.1016/j.egypro.2011.06.197.

[133] S. Bordihn, *Surface Passivation by Al2O3-based Film Stacks for Si Solar Cells*, Phd thesis, Eindhoven University of Technology, 2014.

[134] N. Folchert et al., Solar Energy Materials and Solar Cells **185**, 425 (2018), doi:10.1016/j.solmat.2018.05.046.

[135] D. Tetzlaff et al., Evolution of oxide disruptions: The (W)hole story about poly-Si/c-Si passivating contacts, in *2016 IEEE 43rd Photovoltaic Specialists Conference (PVSC)*, volume 2016-Novem, pages 0221–0224, IEEE, 2016, doi:10.1109/PVSC.2016.7749582.

[136] T. F. Wietler et al., Applied Physics Letters **110**, 253902 (2017), doi:10.1063/1.4986924.

[137] Z. Zhang et al., Solar Energy Materials and Solar Cells **187**, 113 (2018), doi:10.1016/J.SOLMAT.2018.07.025.

[138] J. C. Bravman, G. L. Patton, and J. D. Plummer, Journal of Applied Physics **57**, 2779 (1985), doi:10.1063/1.335421.

[139] F. Feldmann et al., Advanced passivated contacts and their applications to high-efficiency cells, Presentation. *Workshop on Crystalline Silicon Solar Cells and Modules, Keystone, CO*, 2015.

[140] D. Yan, A. Cuevas, J. Bullock, Y. Wan, and C. Samundsett, Solar Energy Materials and Solar Cells **142**, 75 (2015), doi:10.1016/j.solmat.2015.06.001.

[141] J. Gan and R. Swanson, Polysilicon emitters for silicon concentrator solar cells, in *IEEE Conference on Photovoltaic Specialists*, volume 1, pages 245–250, IEEE, 1990, doi:10.1109/PVSC.1990.111625.

[142] U. Römer, *Polycrystalline silicon/monocrystalline silicon junctions and their application as passivated contacts for Si solar cells*, Phd thesis, Gottfried Wilhelm Leibniz Universität Hannover, 2016.

[143] U. Römer et al., IEEE Journal of Photovoltaics **5**, 507 (2015), doi:10.1109/JPHOTOV.2014.2382975.

[144] M. Köhler et al., Development of a Transparent Passivated Contact as a Front Side Contact for Silicon Heterojunction Solar Cells, in *2018 IEEE 7th World Conference on Photovoltaic Energy Conversion (WCPEC) (A Joint*

Conference of 45th IEEE PVSC, 28th PVSEC & 34th EU PVSEC), pages 3468–3472, Waikoloa, Hawaii, 2018, IEEE, doi:10.1109/PVSC.2018.8548008.

[145] H. Umemoto et al., Journal of Applied Physics **91**, 1650 (2002), doi:10.1063/1.1428800.

[146] A. Dasgupta et al., Thin Solid Films **516**, 622 (2008), doi:10.1016/j.tsf.2007.06.077.

[147] T. Chen et al., Thin Solid Films **517**, 3513 (2009), doi:10.1016/j.tsf.2009.01.029.

[148] S. Miyajima, K. Haga, A. Yamada, and M. Konagai, Japanese Journal of Applied Physics **45**, L432 (2006), doi:10.1143/JJAP.45.L432.

[149] S. Miyajima, A. Yamada, and M. Konagai, Japanese Journal of Applied Physics **46**, 1415 (2007), doi:10.1143/JJAP.46.1415.

[150] Y. Hoshide, A. Tabata, A. Kitagawa, and A. Kondo, Thin Solid Films **517**, 3524 (2009), doi:10.1016/j.tsf.2009.01.045.

[151] N. Yoshida et al., Preparations of P- and N-doped hydrogenated microcrystalline cubic silicon carbide films by VHF plasma enhanced chemical vapor deposition method for Si thin film solar cells, in *Physica Status Solidi (C) Current Topics in Solid State Physics*, volume 7, pages 790–792, John Wiley & Sons, Ltd, 2010, doi:10.1002/pssc.200982732.

[152] M. Köhler et al., IEEE Journal of Photovoltaics **10**, 46 (2020), doi:10.1109/JPHOTOV.2019.2947131.

[153] L. Hong-Sheng et al., Chinese Physics Letters **26**, 067101 (2009), doi:10.1088/0256-307X/26/6/067101.

[154] Z. A. Weinberg, G. W. Rubloff, and E. Bassous, Physical Review B **19**, 3107 (1979), doi:10.1103/PhysRevB.19.3107.

[155] S. Klein, R. Carius, F. Finger, and L. Houben, Thin Solid Films **501**, 169 (2006), doi:10.1016/j.tsf.2005.07.180.

[156] Y. Huang, A. Dasgupta, A. Gordijn, F. Finger, and R. Carius, Applied Physics Letters **90**, 203502 (2007), doi:10.1063/1.2739335.

[157] S. Klein, A. Dasgupta, F. Finger, R. Carius, and T. Bronger, Thin Solid Films

516, 630 (2008), doi:10.1016/j.tsf.2007.06.056.

[158] M. Pomaska et al., Journal of Applied Physics **119**, 175303 (2016), doi:10.1063/1.4948479.

[159] G. Schulze and M. Henzler, Surface Science **124**, 336 (1983), doi:10.1016/0039-6028(83)90795-1.

[160] W. Beyer, Physica B: Condensed Matter **170**, 105 (1991), doi:10.1016/0921-4526(91)90111-Q.

[161] G. Dingemans, W. Beyer, M. C. M. van de Sanden, and W. M. M. Kessels, Applied Physics Letters **97**, 152106 (2010), doi:10.1063/1.3497014.

[162] D. E. Carlson and C. W. Magee, Applied Physics Letters **33**, 81 (1978), doi:10.1063/1.90153.

[163] W. Beyer, Hydrogen incorporation in amorphous silicon and processes of its release, in *Tetrahedrally-Bonded Amorphous Semiconductors*, pages 129–146, Springer US, Boston, MA, 1985.

[164] W. Beyer and F. Einsele, Hydrogen Effusion Experiments, in *Advanced Characterization Techniques for Thin Film Solar Cells*, edited by D. Abou-Ras, T. Kirchartz, and U. Rau, volume 1-2, pages 569–595, Wiley-VCH Verlag GmbH & Co. KGaA, Weinheim, Germany, 2016.

[165] C. Banerjee et al., Japanese Journal of Applied Physics **46**, 1 (2007), doi:10.1143/JJAP.46.1.

[166] S. Miyajima, J. Irikawa, A. Yamada, and M. Konagai, Applied Physics Letters **97**, 023504 (2010), doi:10.1063/1.3460917.

[167] J. Irikawa, S. Miyajima, T. Watahiki, and M. Konagai, Applied Physics Express **4**, 092301 (2011), doi:10.1143/APEX.4.092301.

[168] T. Chen, Y. Huang, D. Yang, R. Carius, and F. Finger, Thin Solid Films **519**, 4523 (2011), doi:10.1016/j.tsf.2011.01.299.

[169] H. Matsumura et al., Journal of Applied Physics **116**, 114502 (2014), doi:10.1063/1.4895635.

[170] Y.-R. Luo, *Comprehensive Handbook of Chemical Bond Energies*, CRC Press, 1 edition, 2007.

[171] Y. Huang et al., Journal of Non-Crystalline Solids **354**, 2430 (2008), doi:10.1016/j.jnoncrysol.2007.09.067.

[172] F. Finger et al., Thin Solid Films **517**, 3507 (2009), doi:10.1016/j.tsf.2009.01.115.

[173] G. Kökbudak et al., On the determination of the contact resistivity for passivating contacts using 3D simulations, in *33rd European Photovoltaic Solar Energy Conference and Exhibition, EU PVSEC 2017 : Proceedings of the international conference held in Amsterdam*, pages 242–246, Amsterdam, 2017, doi:10.4229/EUPVSEC20172017-2AO.4.3.

[174] H.-J. Ueng, D. Janes, and K. Webb, IEEE Transactions on Electron Devices **48**, 758 (2001), doi:10.1109/16.915721.

[175] M. van Rijnbach et al., IEEE Transactions on Electron Devices **67**, 1757 (2020), doi:10.1109/TED.2020.2974194.

[176] D. Zhang, A. Tavakoliyaraki, Y. Wu, R. van Swaaij, and M. Zeman, Influence of ITO deposition and post annealing on HIT solar cell structures, in *Energy Procedia*, volume 8, pages 207–213, Freiburg, Germany, 2011, doi:10.1016/j.egypro.2011.06.125.

[177] M. Tamakoshi and N. Matsuki, Japanese Journal of Applied Physics **54**, 08KD09 (2015), doi:10.7567/JJAP.54.08KD09.

[178] A. Khanna et al., IEEE Journal of Photovoltaics **3**, 1170 (2013), doi:10.1109/JPHOTOV.2013.2270348.

[179] C.-T. T. Sah, R. N. Noyce, and W. Shockley, Proceedings of the IRE **45**, 1228 (1957), doi:10.1109/JRPROC.1957.278528.

[180] M. Pomaska et al., Progress in Photovoltaics: Research and Applications **28**, 321 (2020), doi:10.1002/pip.3244.

[181] B. Demaurex, S. De Wolf, A. Descoeudres, Z. Charles Holman, and C. Ballif, Applied Physics Letters **101**, 171604 (2012), doi:10.1063/1.4764529.

[182] D. Skorka, N. Brinkmann, A. Gorgulla, G. Hahn, and B. Terheiden, Changes in Passivation Quality of PECVD-Deposited Hydrogenated Amorphous Silicon Layers used in Solar Cells due to Sputter Deposition of TCOs, in *Proceed-*

ings of the 28th European Photovoltaic Solar Energy Conference and Exhibition (EU PVSEC 2013), pages 1162–1165, Paris, France, 2013, WIP-Munich, doi:https://dx.doi.org/10.4229/28thEUPVSEC2013-2BV.1.39.

[183] A. Illiberi, P. Kudlacek, A. H. M. Smets, M. Creatore, and M. C. M. van de Sanden, Applied Physics Letters **98**, 242115 (2011), doi:10.1063/1.3601485.

[184] L. Zhao, Z. Zhou, H. Peng, and R. Cui, Applied Surface Science **252**, 385 (2005), doi:10.1016/j.apsusc.2005.01.033.

[185] J. R. Woodworth, M. E. Riley, P. A. Miller, G. A. Hebner, and T. W. Hamilton, Journal of Applied Physics **81**, 5950 (1997), doi:10.1063/1.364383.

[186] F. Lebreton, S. N. Abolmasov, F. Silva, and P. Roca i Cabarrocas, Applied Physics Letters **108**, 051603 (2016), doi:10.1063/1.4941298.

[187] H. B. Profijt, P. Kudlacek, M. C. M. van de Sanden, and W. M. M. Kessels, Journal of The Electrochemical Society **158**, G88 (2011), doi:10.1149/1.3552663.

[188] C. Cismaru, J. L. Shohet, J. L. Lauer, R. W. Hansen, and S. Ostapenko, Applied Physics Letters **77**, 3914 (2000), doi:10.1063/1.1331081.

[189] Y. Wu et al., Chemistry of Materials **25**, 4619 (2013), doi:10.1021/cm402974j.

[190] S. Li et al., Research Square Preprint **Version 1** (2020), doi:10.21203/rs.3.rs-97106/v1.

[191] H. Kitami, M. Miyashita, T. Sakemi, Y. Aoki, and T. Kato, Japanese Journal of Applied Physics **54**, 01AB05 (2015), doi:10.7567/JJAP.54.01AB05.

[192] J. Shi, L. Shen, F. Meng, and Z. Liu, Materials Letters **182**, 32 (2016), doi:10.1016/j.matlet.2016.06.084.

[193] F. Meng et al., Japanese Journal of Applied Physics **56**, 04CS09 (2017), doi:10.7567/JJAP.56.04CS09.

[194] Y. Takagi, Y. Sakashita, H. Toyoda, and H. Sugai, Vacuum **80**, 581 (2006), doi:10.1016/j.vacuum.2005.10.001.

[195] H. R. Kaufman and J. M. E. Harper, Journal of Vacuum Science & Technology A: Vacuum, Surfaces, and Films **22**, 221 (2004), doi:10.1116/1.1633565.

[196] A. H. M. Smets, W. M. M. Kessels, and M. C. M. van de Sanden, Journal of

Applied Physics **102**, 073523 (2007), doi:10.1063/1.2786873.

[197] S. De Wolf and M. Kondo, Applied Physics Letters **91**, 112109 (2007), doi:10.1063/1.2783972.

[198] S. De Wolf and M. Kondo, Journal of Applied Physics **105**, 103707 (2009), doi:10.1063/1.3129578.

[199] M. L. Reed and J. D. Plummer, Journal of Applied Physics **63**, 5776 (1988), doi:10.1063/1.340317.

[200] W. Duan, J. Bian, J. Yu, J. Shi, and Z. Liu, IEEE Transactions on Electron Devices **62**, 1113 (2015), doi:10.1109/TED.2015.2402175.

[201] J. Geissbühler et al., IEEE Journal of Photovoltaics **4**, 1055 (2014), doi:10.1109/JPHOTOV.2014.2321663.

[202] W. G. J. H. M. van Sark, L. Korte, and F. Roca, editors, *Physics and Technology of Amorphous-Crystalline Heterostructure Silicon Solar Cells*, Engineering Materials, Springer, Berlin, Heidelberg, 2012.

[203] P. Procel, G. Yang, O. Isabella, and M. Zeman, Solar Energy Materials and Solar Cells **186**, 66 (2018), doi:10.1016/j.solmat.2018.06.021.

[204] P. Procel, G. Yang, O. Isabella, and M. Zeman, IEEE Journal of Photovoltaics **9**, 374 (2019), doi:10.1109/JPHOTOV.2019.2892527.

[205] G. Lubberts, B. C. Burkey, F. Moser, and E. A. Trabka, Journal of Applied Physics **52**, 6870 (1981), doi:10.1063/1.328681.

[206] K. R. McIntosh and S. C. Baker-Finch, OPAL 2: Rapid optical simulation of silicon solar cells, in *2012 38th IEEE Photovoltaic Specialists Conference*, pages 000265–000271, Austin, 2012, IEEE, doi:10.1109/PVSC.2012.6317616.

[207] Z. Hu et al., Solar Energy Materials and Solar Cells **95**, 2173 (2011), doi:10.1016/j.solmat.2011.03.020.

[208] Z. Lu et al., Journal of Physics D: Applied Physics **46**, 075103 (2013), doi:10.1088/0022-3727/46/7/075103.

[209] F. Meng et al., Solar Energy Materials and Solar Cells **122**, 70 (2014), doi:10.1016/j.solmat.2013.11.030.

[210] T. Koida, H. Fujiwara, and M. Kondo, Japanese Journal of Applied Physics

46, L685 (2007), doi:10.1143/JJAP.46.L685.

[211] T. Koida et al., Journal of Applied Physics **107**, 033514 (2010), doi:10.1063/1.3284960.

[212] B. Macco, H. C. M. Knoops, and W. M. M. Kessels, ACS Applied Materials & Interfaces **7**, 16723 (2015), doi:10.1021/acsami.5b04420.

[213] J.-I. Polzin, F. Feldmann, B. Steinhauser, M. Hermle, and S. Glunz, Realization of TOPCon using industrial scale PECVD equipment, in *AIP Conference Proceedings*, volume 1999, page 040018, Lausanne, Switzerland, 2018, American Institute of Physics Inc., doi:10.1063/1.5049281.

[214] L. Xiao, O. Astakhov, T. Chen, M. Stutzmann, and F. Finger, Thin Solid Films **519**, 4519 (2011), doi:10.1016/j.tsf.2011.01.320.

[215] T. Chen, F. Köhler, A. Heidt, R. Carius, and F. Finger, Japanese Journal of Applied Physics **53**, 05FM04 (2014), doi:10.7567/JJAP.53.05FM04.

[216] Chapter 21 An introduction to experimental design, in *Handbook of Chemometrics and Qualimetrics: Part A*, edited by J. S.-V. D.L. Massart, B.G.M. Vandeginste, L.M.C. Buydens, S. De Jong, P.J. Lewi, pages 643–658, 1998.

[217] Chapter 22 Two-level factorial designs, in *Handbook of Chemometrics and Qualimetrics: Part A*, edited by D. L. Massart et al., volume 20 of *Data Handling in Science and Technology*, pages 659–682, Elsevier, 1998.

[218] Chapter 23 Fractional factorial designs, in *Handbook of Chemometrics and Qualimetrics: Part A*, edited by D. L. Massart et al., volume 20 of *Data Handling in Science and Technology*, pages 683–699, Elsevier, 1998.

[219] K. Siebertz, D. van Bebber, and T. Hochkirchen, *Statistische Versuchsplanung*, Springer, Berlin, Heidelberg, 2010.

[220] J. Antony, *Design of Experiments for Engineers and Scientists*, Elsevier, 2 edition, 2014.

[221] C. A. Nunes, M. P. Freitas, A. C. M. Pinheiro, and S. C. Bastos, Journal of the Brazilian Chemical Society **23**, 2003 (2012), doi:10.1590/S0103-50532012005000073.

Acknowledgments

I would like to express my deepest gratitude to all those who made this work possible. It was a wonderful journey, which wouldn't have been the same without some special people. I would like to thank:

Prof. Dr. Uwe Rau for the supervision and examination of this thesis, for conclusive discussions and long nights of writing short papers.

Dr. Manuel Pomaska for the best supervision I only could have wished for and always finding the perfect balance between professional and personal guidance. You became not only a rolemodel but also a very good friend.

Dr. Kaining Ding for being an excellent supervisor and always encouraging critical thinking.

Prof. Dr. Thomas Kirchartz for always having an open door and the patience to explain things again when I did not get it the first three times and for beeing an excellent mentor.

Dr. Friedhelm Finger and *Prof. Dr. Reinhard Carius* for shaping every manuscript until it was close to perfect.

Dr. Wolfhard Beyer for many fruitful and enlightening discussions about hydrogen.

Prof. Dr. Paul Strading for beeing my external mentor and providing an outside view on my thesis.

Johannes Wolff, *Andreas Schmalen*, and *Sven Schiffer* for providing world class technical equipment and support for the hot-wire systems.

Dr. Andreas Lambertz and the baseline team for providing excellent solar cells. Without your relentless improvements of the baseline my results wouldn't have been possible.

Dr. Alexandr Zamchiy for helping me with a lot of experiments and measurements as well as a lot of hot-wire knowledge.

The whole *IEK-5* and especially our group, who contributed so many details, enabled this whole thesis.

The TCO task force to tackle the degradation problem with *Dr. Bart Macco*, *Hildegard Siekmann*, *Leonard Tutsch*, *Dr. Matthieu Boccard*, and *Dr. Byungsul Min.*

The HNF team including *Irina Kempf*, *Janine Worbs*, *Georg Mathey*, *Matthias Geitner* and *Alain Doumit* for supporting me in the cleanroom and always having a good time.

The team of UK around *Christina Hallen* and *Thomas Bierschenk* for the organization and all the tour guides from young to old, who made the tour guiding so much fun not only for me but hopefully also for the visitors. It opened a whole new world for me to see what all the other 5999 people were working on around me.

I would also like to thank all the people contributing to the *Rurtalbahn Think-Tank* for all the discussions, ideas and innovations which were discussed, embraced and discarded here. A special thanks here to the *Inner Circle* for years of friendship, inspiration and consolation sweating or freezing in trains, at train stations or in bars.

My physics teacher in school *Wolf-Rüdeger Schanz* who ignited my passion for photovoltaics.

My friends, flatmates, and sports teams who kept me balanced especially in stressful times.

My whole family for supporting me and having my back in every situation.

And especially my beloved fiancée *Pia* for being the best companion I could have wished for in every situation. Thank you for creating tons of beautiful experiences and memories along our way.

Thanks to each and every one of you, who helped me achieve this thesis. It would not have been possible without you. Thanks!

Band / Volume 525
ETV Online Tagung 2020
Industrielle Groß- und Hochtemperaturwärmepumpen im Energiesystem
D. Stolten, G. Markowz (Hrsg.) (2020), ca. 71 pp
ISBN: 978-3-95806-519-2

Band / Volume 526
Atmospheric Trace Gas Measurements Using Chemical Ionisation Time-of-Flight Mass Spectrometry
Y. Li (2020), xi, 110 pp
ISBN: 978-3-95806-520-8

Band / Volume 527
Uranium accumulation in agricultural soils as derived from long-term phosphorus fertilizer applications
Y. Sun (2020), XII, 136 pp
ISBN: 978-3-95806-521-5

Band / Volume 528
Entwicklung von Schutzschichten für nicht-oxidische Faserverbundwerkstoffe
M. Wolf (2021), VI, 150, 2 pp
ISBN: 978-3-95806-524-6

Band / Volume 529
Mechanical reliability and oxygen permeation of $\mathrm{Ce_{0.8}Gd_{0.2}O_{2-\delta}}$-$\mathrm{FeCo_2O_4}$ dual phase membranes
F. Zeng (2021), IV, VI, 222 pp
ISBN: 978-3-95806-527-7

Band / Volume 530
Capacitance-Based Methods to Study Charge Transport and Recombination in Organic Solar Cells
I. Zonno (2021), vi, 153 pp
ISBN: 978-3-95806-528-4

Band / Volume 531
Einflüsse von Klimavariabilität und -wandel auf Ausbau und Erzeugung im Europäischen Stromsystem
F. P. Gotzens (2021), XXIII, 231 pp
ISBN: 978-3-95806-530-7

Band / Volume 532
Weltweite Infrastruktur zur Wasserstoffbereitstellung auf Basis erneuerbarer Energien
P.-M. Heuser (2021), VII, 231 pp
ISBN: 978-3-95806-531-4

Band / Volume 533
Mechanische Eigenschaften von katalysatorbeschichteten Membranen für die Polymer-Elektrolyt-Membran Elektrolyse
E. Borgardt (2021), viii, 181 pp
ISBN: 978-3-95806-533-8

Band / Volume 534
Techno-economic Assessment of Hybrid Post-combustion Carbon Capture Systems in Coal-fired Power Plants and Steel Plants
Y. Wang (2021), IV, xx, 230 pp
ISBN: 978-3-95806-545-1

Band / Volume 535
Wissenschaftliche Begleitstudie der Wasserstoff Roadmap Nordrhein-Westfalen
S. Cerniauskas, P. Markewitz, J. Linßen, F. Kullmann, T. Groß,
P. Lopion, P-M. Heuser, T. Grube, M. Robinius und D. Stolten
(2021), IV, 89 pp
ISBN: 978-3-95806-547-5

Band / Volume 536
High-Resolution Photocurrent Mapping of Thin-Film Silicon Solar Cells Using Scanning Near-Field Optical Microscopy
Z. Cao (2021), xiii, 148 pp
ISBN: 978-3-95806-548-2

Band / Volume 537
Kompressionseigenschaften der Gasdiffusionslage einer Hochtemperatur-Polymerelektrolyt-Brennstoffzelle
E. Hoppe (2021), viii, 153 pp
ISBN: 978-3-95806-549-9

Band / Volume 538
Transparent Passivating Contact for Crystalline Silicon Solar Cells
M. Köhler (2021), 186 pp
ISBN: 978-3-95806-550-5

Weitere ***Schriften des Verlags im Forschungszentrum Jülich*** unter
http://wwwzb1.fz-juelich.de/verlagextern1/index.asp

Energie & Umwelt / Energy & Environment
Band / Volume 538
ISBN 978-3-95806-550-5

Mitglied der Helmholtz-Gemeinschaft

JÜLICH
Forschungszentrum